Spring 1-1-2017

An Investigation into Wind Turbine Acoustic Noise Variability

Steven Redford Buck
University of Colorado at Boulder, redfordb3@gmail.com

Recommended Citation
Buck, Steven Redford, "An Investigation into Wind Turbine Acoustic Noise Variability" (2017). *Aerospace Engineering Sciences Graduate Theses & Dissertations*. 161.
https://scholar.colorado.edu/asen_gradetds/161

An Investigation into Wind Turbine Acoustic Noise Variability

by

Steven Buck

B.S., University of Florida, 2011

M.S., University of Colorado Boulder, 2014

A thesis submitted to the
Faculty of the Graduate School of the
University of Colorado in partial fulfillment
of the requirements for the degree of
Doctor of Philosophy
Department of Aerospace Engineering
2017

This thesis entitled:
An Investigation into Wind Turbine
Acoustic Noise Variability
written by Steven Buck
has been approved for the Department of Aerospace Engineering

Prof. Scott Palo

Dr. Stefan Oerlemans

Dr. Pat Moriarty

Date

The final copy of this thesis has been examined by the signatories, and we find that both the content and the form meet acceptable presentation standards of scholarly work in the above mentioned discipline.

Buck, Steven (Ph.D., Remote Sensing)

An Investigation into Wind Turbine
Acoustic Noise Variability

Thesis directed by Prof. Scott Palo

Wind turbine acoustic noise has been the subject of significant research in recent decades due to rapid growth in the wind energy industry. Available space with a reliable wind resource and that does not reside near populated areas is becoming extremely scarce, particularly in Europe. This decline in available space then results in a heightened need for wind turbine designs to be optimized for both acoustic emission and power-performance. Due to highly variable operating conditions, wind turbine acoustic noise emission may deviate from design levels, causing irritation to local residents and requiring reduced power production of the contributing turbines. The objective of this dissertation is to investigate two parameters that contribute to this variability—atmospheric turbulence in the inflow field, and aerodynamic flow separation—such that they may be more fully understood and properly accounted for in design. Results are achieved through an extensive experimental campaign on a full-scale turbine equipped with a thorough sensor network. Several novel flow characterization methods are developed, including a method of in-situ turbulence measurement using blade-mounted accelerometers. Turbulent inflow noise is shown to dominate the low frequency portion of the emitted spectrum for normal turbine operation and increases levels by as much as 6 dB for the conditions observed at the research facility. Experimental observations are typically within 2-3 dB of a commonly implemented noise prediction model. Finally, a study into the effects of high angle of attack operation shows that aerodynamic flow separation—detected using static pressure sensors along one blade of the turbine—can increase overall noise levels by more than 10 dB, thus dominating turbulent inflow noise at low frequencies. The studies of both turbulent inflow noise and flow separation noise represent the most thorough experimental observations and analysis of the respective noise mechanisms on a full-scale wind turbine.

Dedication

To my parents, for everything they have taught me and will inevitably continue to teach me.

Acknowledgements

The work of this dissertation would not have been possible without the open-mindedness and flexibility of numerous people within Siemens Wind Power. The context in which this dissertation was completed was not an established framework. Rather, several of the engineers and managers within the company were willing to explore somewhat uncharted territory—to not only dig deeply into scientific questions within the field, but to make the results public, thereby broadening the greater knowledge-base of the wind energy industry. Without this flexibility, this dissertation would have amounted to little more than a title page and would not likely have satisfied the approving committee. This fact has not gone unappreciated, and I will remain grateful as I continue to use the knowledge I have gained in the process.

In particular, I would like to thank those that have contributed to this research: my technical advisors, Professor Scott Palo and Dr. Stefan Oerlemans for their countless conversations and feedback; Dr. Pat Moriarty of the National Wind Technology Center (NWTC) for his advisement through this entire process; the many engineers at Siemens Wind Power (SWP) for providing a wealth of knowledge on all aspects of wind energy; Mike Asheim and Manjinder Singh for designing and building the acoustic data acquisition system; John Obrecht for his interest in the work and for building the point-source noise model; those at the NWTC for designing an incredible atmospheric measurement system; Brian Killourhy and Matt Brzezinski for their invaluable and frequent assistance with the field work; Jason Roadman, Jeroen van Dam, and Andy Scholbrock of the NWTC for their assistance in managing site-related logistics and for keeping neighboring turbines quiet; and all the members of my dissertation committee for their time and advice.

Contents

Chapter

Figures

Figure

Chapter 1

Introduction

1.1 Problem Statement

Wind turbine acoustic noise generation presents a significant hindrance to the widespread acceptance of wind power. The noise negatively impacts public opinion due to perceived annoyance, places limitations on the locations where turbines can be constructed due to local nose regulations, and can require power-curtailed operation in the case where noise emissions must be reduced. For this reason, wind turbine acoustics has been the subject of significant research in recent decades. A considerable portion of this work has been focused on modeling and prediction of wind turbine noise [35, 33, 49, 31, 59, 65]. These models allow for informed wind turbine design with proper consideration for acoustic optimization [63]. Robust acoustic optimization in turn leads to improved financial viability of wind farms and competitiveness with other forms of energy such as coal and natural gas. As wind is a renewable, non-polluting form of energy production, these advantages are seen as a benefit to the well-being of the global community. The acoustic emission of a wind turbine represents a complex physical system, however, and significant unanswered scientific questions persist.

Acoustic noise generated by modern industrial scale wind turbines is typically dominated by aerodynamic noise, since mechanical noise is more readily reduced by careful design [78]. For Mach numbers relevant to wind turbines, aeroacoustic noise is in general produced by unsteady flow interacting with a solid surface—in this case the wind turbine blades. Oerlemans et al. [65, 64] showed that aerodynamic noise at frequencies above a few hundred Hz from wind turbines is dominated by turbulent boundary layer trailing edge noise (TE noise). This is the noise generated by turbulence in the boundary layer of an airfoil interacting with the discontinuity of the trailing edge. Since the aerodynamic boundary layers for modern, large wind turbines are generally turbulent because of their operating Reynolds numbers, boundary layer turbulence and TE noise are present regardless of inflow conditions. Oerlemans et al. [64] has shown that wind turbine noise—particularly the mid to high frequency levels and overall A-weighted levels—can be predicted to within a few decibels (dB) using only a trailing edge noise model. A-weighted levels reflect the perception of human hearing by de-emphasizing very low and very high frequencies, so the prediction of A-weighted levels is quite important; this concept is returned to throughout this dissertation. Such a model offers an accurate baseline prediction for when inflow conditions can be approximated as steady and uniform. This condition of steady, uniform flow raises an important question: When can flow conditions be approximated as steady and uniform, and when must secondary effects be considered? Such secondary effects are the subject of this dissertation, as they can result in appreciable deviation from design noise levels.

Acoustic noise from wind turbines is often assessed by wind turbine manufacturers and noise regulators alike based on IEC Standard 61400-11 [23]. This standard offers a framework for determining the sound power generated by a wind turbine as a function of wind speed. It includes provisions for microphone selection, microphone calibration, microphone positioning, minimum signal to noise ratio, wind speed measurement methods, and convergence criteria for results. However, even when measurements are taken in accordance with this standard, significant variability in recorded levels between cases has been observed. Intuitively, this variability may be broken into three groups of root causes: variability in acoustic noise emission, variability in acoustic noise propagation, and variability in acoustic noise measurement. With regard to regulation, consideration must also be made for variation in human perception of noise, e.g. with age or location. This study will be focused primarily on acoustic noise emission variability. Some consideration will also be given to propagation effects, simply because this impacts what neighbors may observe in comparison to more localized measurements. Variability due to measurement conditions—e.g. microphone placement, microphone board angle, microphone calibration—will only be considered in the context of acquiring sufficiently controlled data. To be clear, this is not intended as an investigation into the sufficiency of IEC Standard 61400-11; the standard is only discussed for illustration purposes. The motivation of the proposed research is to develop a more thorough understanding of wind turbine acoustics such that proper consideration can be made for the parameters shown to contribute to acoustic noise variability.

1.2 Scientific Motivations

At the outset of the research campaign for this dissertation, a host of variability parameters were identified for potential inclusion in the investigation. These parameters were identified based on a fundamental understanding of the wind turbine noise generation mechanisms and an assessment of typical regulations and noise measurement methods. The parameters included in the investigation can then be ranked based on several merit criteria. Namely:

(1) **How much can the parameter potentially affect noise levels?** Scientific conclusions can be considered to be significantly more practical if the parameter being investigated has a large effect on wind turbine noise; several decibels (dB) could be considered a large effect.

(2) **How much is currently known about the mechanism?** The less understood and well-defined the parameter's effects are, the more value its investigation can be considered to have for the academic and industrial communities.

(3) **How readily can the parameter be investigated?** As a practical consideration for the success of the campaign, the parameter must be able to be investigated in a well-controlled manner, either by experimentation or simulation.

(4) **How likely or frequently will the effect arise in practice?** The value of this study depends on how commonly the selected variability parameters may actually affect the acoustic output of a deployed turbine.

These selection criteria give insight into the scientific motivations of this dissertation; a balance is sought between intellectual merit and industrial utility.

The first variability parameter selected for investigation is atmospheric turbulence in the inflow to a wind turbine. Atmospheric turbulence—and specifically surface layer turbulence—is driven by the ground terrain roughness and atmospheric stability [44, 66]. The magnitude and spectral characteristics of atmospheric turbulence naturally vary between wind sites and in time depending on these characteristics. Inflow turbulence radiates sound when it interacts with the leading edge of an airfoil [4, 70, 53] or with a wind turbine blade [35, 33, 49, 59]. As such, turbulence conditions in the inflow to a wind turbine define a variability parameter that will contribute to differences in acoustic noise generated site-to-site, day-to-night, seasonally, etc., even by identical turbines. Furthermore, as is discussed thoroughly within this dissertation, the amount of research published about wind turbine turbulent inflow noise has been quite limited. Several models have been proposed for wind turbine turbulent inflow noise [35, 49, 58], but experimental evidence to support their accuracy is lacking. The reasons for this lack of experimental validation appear be the difficulty of experimental control when investigating turbulence noise in the field, insufficient methods for characterizing inflow turbulence in prior experiments, and a recent focus upon trailing edge noise [63], a separate noise mechanism shown to dominate the mid- to high-frequency range of wind turbine noise [65, 64]. As turbulent inflow noise is predicted to dominate the low-frequency portion of the turbine noise spectrum [49, 57], its effect is expected to have the most impact at large distances from a turbine where atmospheric attenuation of higher frequencies reduces their effect. Thus, inflow turbulence satisfies the selection criteria listed above in that it has not been well characterized in the literature and that its impact on industrial turbines' acoustic emission is expected to be significant due to natural variation in turbulence conditions.

The second variability parameter to be investigated is the effect of aerodynamic flow separation on wind turbine noise. Aeroacoustic studies of flow separation show it to have drastic effects on noise output [75, 54], with between 10 and 30 dB increases depending on the flow conditions and the severity of flow separation. For this reason, modern industrial scale turbines are typically designed to avoid flow separation under normal operating conditions [20]. However, variation in operational conditions such as high wind shear, yaw error (the difference between the inflow direction and turbine yaw direction), turbine-wake interactions, and wind gusts can lead to off-design angle of attack operation and, in turn, flow separation. Further, flow separation on wind turbine blades can be periodic with the blade passing frequency, which is referred to as “dynamic stalling” and is cited as a potential cause of thump-noise [61, 50]. Thump-noise is an intense amplitude modulation of wind turbine noise and intuitively makes the noise more irritating to nearby residents than the nominal acoustic levels, which are typically approximately constant and broadband at relatively large distances from a turbine [61]—the noise of a dripping faucet versus a steady rain is analogous. Research into wind turbine flow separation noise and airfoil flow separation noise is relatively limited. Maruta [52] attributes the limited amount of research to the complexity of the flow structure in the separated flow region and the common aerodynamic design philosophy of avoiding separated flow conditions. Further, with application to wind turbines, the inflow conditions cannot be controlled, so flow separation can only be studied under the happenstance that these conditions arise during a measurement campaign or by deliberately inducing high angles of attack. The latter is the approach of this dissertation, which will serve to characterize the acoustic effects of flow separation specifically for wind turbines. The results pertain directly to the flow regimes relevant to modern, industrial scale wind turbines and can therefore most readily be used to affect design decisions and potentially improve modeling capabilities.

1.3 Research Questions

The research questions answered by this dissertation, along with the scientific approach taken for each, are as follows.

(1) **How does turbulence in the inflow field of a wind turbine affect its acoustic noise generation?**

Approach: An extensive data acquisition campaign was conducted on a full-scale 2.3

MW Siemens turbine, resulting in over 50 hours of acoustic data at power generating wind speeds. Thorough acoustic and atmospheric instrumentation was used. This approach allows for the atmospheric conditions to naturally vary during measurement, and facilitates a simple correlation study as a first, coarse investigation into the question: Does increased turbulence lead to increased noise? The study considers on two potential turbulence noise generation mechanisms. Namely, noise radiation from pressure fluctuations on the surface of the blades due directly to small scale turbulent fluctuations in the atmosphere, and angle of attack variations due to larger scale turbulent fluctuations, resulting in modified trailing edge and separation noise characteristics. A novel method of characterizing the inflow turbulence using accelerometers in each of the three blades is also developed to mitigate the effects of turbulence spatial de-correlation and flow non-stationarity.

(2) **How does observed turbulent inflow noise compare to the theoretical expectations?**

Approach: As discussed above, several models of wind turbine turbulent inflow noise have been developed in the past, though they lack significant experimental validation. Several wind turbine noise codes [31, 57] are largely based on the prediction model developed by Lowson [49], so this model forms the foundation of the predictions made in this dissertation. Comparisons are made on the basis of absolute noise levels, spectral shape, noise directivity about the turbine, scaling of noise with turbulence levels, and scaling of noise with blade tip speed. The effect of blade thickness on noise is also considered by the inclusion of a modified model developed by Guidati [36] and Moriarty [58].

(3) **What is the aeroacoustic effect of separated flow on a wind turbine blade?**

A test was designed and conducted in which separated flow is deliberately induced on the blades of the test turbine by reducing the rotor RPM below its design level, thus increasing the operating angle of attack. By then pitching the blades of the turbine, the flow reattaches, allowing for a comparison of acoustic characteristics for separated and attached flow at the same rotor RPM. Separated flow is detected using static pressure ports on the surface of one of the turbine blades. This allows for effective filtering by aerodynamic state, i.e. by separated versus attached flow. Comparisons are made based on absolute levels, spectral shape, and noise directivity. Finally, a comparison is made to data collected with normal turbine settings at the same rotor RPM, i.e. at lower wind speeds. This final comparison gives an assessment of the hypothetical scenario of a strong gust-front pushing the entire turbine rotor into flow separation—effectively a worst-case noise increase.

The layout of this dissertation is as follows. Chapter 2 gives a summary of the prior research leading to the current state of the art in the field of wind turbine acoustics, beginning with fundamental aeroacoustics theory and leading to modern research topics. Chapter 3 discusses the experimental facility where all data for this dissertation was gathered, including a description of the research turbine, sensor networks, and data acquisition systems. Chapter 4 details a novel turbulence characterization method developed specifically for the turbulent inflow noise investigation described in Chapter 5. Chapter 5 shows the experimentally observed effects of turbulence on measured noise levels (Question 1), and Chapter 6 makes comparisons of these observations to a commonly implemented turbulent inflow noise prediction model (Question 2). Finally, Chapter 7 details the methods and results of an investigation into the effects of aerodynamic flow separation on wind turbine acoustic noise emission (Question 3).

1.4 Nomenclature

A	Kolmogorov constant for three dimensional turbulent energy spectrum
D	Airfoil acoustic noise directivity factor
$E(k)$	Three dimensional turbulence energy spectrum
E^*	Combination of sine and cosine Fresnel integrals
$H(f)$	Impulse response function between blade lift and acceleration
$\mathrm{I_T}$	Turbulence intensity
$\mathrm{I_{T,eq}}$	Equivalent turbulence intensity measured by blade accelerometers
J_i	Bessel function of the first kind of the ith order
L	Turbulence integral length scale
$\hat{L}$	Unsteady loading function defined by Equation 2.16
L_r	Sectional lift force per unit length
M	Mach number
S	Approximation for compressible Sears function
SPL^H	High frequency asymptote of the turbulent inflow noise model
$S_{LL}(f)$	Power spectral density of blade sectional lift
$S_{aa}(f)$	Power spectral density of blade-accelerometer signal
$S_{ii}(f)$	Power spectral density of velocity along the i axis
T_{rel}	Airfoil thickness as fraction of chord
T_{ij}	Lighthill stress tensor defined by Equation 2.2
U	Mean wind speed
V	Characteristic flow speed
a_0	Freestream speed of sound
b	Airfoil or blade semi-chord
c_l	Sectional 2d lift coefficient
$c_{l,\alpha}$	Rate of change of lift coefficient with angle of attack

$c_{l,0}$	Sectional lift coefficient at zero angle of attack
d	Airfoil semi-span
f	Frequency
g	Transfer function between vertical velocity and airfoil surface pressure
k	Turbulence wavenumber
k_a	Acoustic wavenumber
k_e	Turbulence wavenumber scale (Equation 4.8)
k_i	Wave vector component along the i axis
l	Characteristic length scale
$\vec{n}$	Outward unit normal vector for enclosed surface
p	Perturbation/acoustic pressure
r	Source-observer distance
t	Time
u_i	Fluid velocity in the i direction
u_{in}	Local blade section inflow speed
v_i	Solid surface velocity in the i direction
x_i	Spacial coordinate along the i axis
Γ	Gamma function
$\Phi_{ii}(k)$	Wavenumber spectrum for boundary layer turbulence in the i direction
Ω	Rotor rotational rate in rad/sec
α	Angle of attack
α_u	Kolmogorov constant for streamwise power spectral density
β	$\sqrt{1-M^2}$
δ	Boundary layer thickness to 99% freestream conditions
δ^*	Boundary layer displacement thickness
$\delta(\vec{x})$	Dirac delta function
ϵ	Turbulence dissipation rate

κ	Turbulence kinetic energy
λ	Acoustic wavelength
λ_T	Turbulence hydrodynamic wavelength
ξ	Microphone viewing angle
ρ	Air density
σ	Compressible coordinate quantity, Equation 2.15
σ_i	Root-mean-squared perturbation velocity along the i axis
$\hat{\omega}$	Non-dimensional frequency parameter equal to kb

Chapter 2

History and Background

2.1 Fundamental Aeroacoustic Theory

This section details some of the foundational physics of aeroacoustics, upon which the topics of this dissertation are based. The theory presented is generally arranged chronologically, beginning in the early 1950's and leading into the late 1980's. More importantly, the topics are arranged with the broadest, theoretical work presented first, and with each subsequent study building upon the last, leading finally to the specific case of airfoil noise.

2.1.1 Lighthill's Acoustic Analogy

Lighthill [47] produced some of the earliest theory on sound that is generated aerodynamically and perhaps the first work to properly analytically explore the *intensity* of sound generated by a given flow field. As noted by Lighthill and later Curle [26], prior work had been largely concerned with the frequencies in aerodynamically generated acoustic fields. Those that had explored acoustic intensities had been in error; approximations were made too early in the derivations that, in Lighthill's words, "throw away the one small part of the sound field which it is desirable to keep, or swamp it with much larger terms".

The exact governing equations for the fluid flow are given in Equation 2.1 below. Equation 2.1a is the compressible continuity equation, and 2.1b is the exact conservation of momentum equation, as of yet making no assumptions about the stress-strain relation, e.g. Newtonian fluid behavior or Stokes' hypothesis.

$$\frac{\partial \rho}{\partial t} + \frac{\partial}{\partial x_i}(\rho u_i) = 0 \tag{2.1a}$$

$$\frac{\partial}{\partial t}(\rho u_i) + \frac{\partial}{\partial x_j}(\rho u_i u_j + p_{ij}) = 0 \tag{2.1b}$$

Above, ρ is the density of the fluid, u_i is the fluid velocity in the x_i direction, and p_{ij} is the total stress tensor. Lighthill notes that the second term in Equation 2.1b is an equivalent stress term, signifying that a fluid in fluctuating motion experiences changes in local momentum ρv_i equal to the local changes in momentum a fluid at rest would experience if it were acted upon by a real stress equal to $\rho u_i u_j + p_{ij}$.

We now define—and will later give physical insight to—what is known as the Lighthill stress tensor,

$$T_{ij} = \rho u_i u_j + p_{ij} - a_0^2 \rho \delta_{ij}, \tag{2.2}$$

which, by manipulation of Equation 2.1b, leads to the relation

$$\frac{\partial}{\partial t}(\rho u_i) + a_0^2 \frac{\partial \rho}{\partial x_i} = -\frac{\partial T_{ij}}{\partial x_j}. \tag{2.3}$$

Here, a_0 is the speed of sound in the fluid at rest and δ_{ij} is the Kronecker delta. Now, subtracting the partial time derivative of continuity, Equation 2.1a, from the gradient of the Ligthill momentum equation, Equation 2.3, eliminates the ρu_i terms and yields

$$\frac{\partial^2 \rho}{\partial t^2} - a_0^2 \nabla^2 \rho = \frac{\partial^2 T_{ij}}{\partial x_i \partial x_j} \tag{2.4}$$

Equation 2.4 is the inhomogeneous wave equation analyzed by Lighthill in his consideration of the aerodynamic sound generation problem. It is equivalent to a general forced wave equation with a forcing term $-\frac{\partial^2 T_{ij}}{\partial x_i \partial x_j}$, and is thus referred to as Lighthill's acoustic analogy. Considering a flow comprised of a region of bulk flow and a region that is approximately a uniform acoustic medium at rest, e.g. turbulent jet flow [48], the Lighthill stress represents an imbalance between the equivalent stress of the bulk flow $\rho u_i u_j + p_{ij}$ and the hydrostatic pressure stress of the acoustic medium, equal to $a_0^2 \rho \delta_{ij}$.

Note that Equation 2.4 is still exact, as it has been derived directly from the compressible continuity equation and a reformulated conservation of momentum equation. The Lighthill stress term T_{ij} encompasses effects such as viscous dissipation and local variations in the speed of sound. In other words, the system has not been linearized, as is typically done in derivation of the acoustic wave equation [10]. In regions where flow perturbations are small, however, the right hand side of Equation 2.4 vanishes, because the velocity perturbation term is of second order, and pressure perturbations are balanced by density perturbations. In this case the system reduces to the homogenous, linear acoustic wave equation.

Further insight is gained by examination of the forcing term of the inhomogeneous wave equation, namely $-\frac{\partial^2 T_{ij}}{\partial x_i \partial x_j}$. The solution to the inhomogeneous wave equation for a forcing function $-\frac{\partial F_i}{\partial x_i}$, where $\vec{F}$ represents a force acting locally on the fluid—perhaps by a vibrating surface—is given by a distribution of dipoles of strength $\vec{F}$ per unit volume with axes in the direction of the force $\vec{F}$. A stress tensor, including the equivalent Lighthill stress tensor, effectively describes equal and opposite forces at each side of an infinitesimal fluid element, and is then equivalent to a combination of dipole sources at each surface of the fluid element. Pure pressure stresses then represent longitudinal quadrupole sources (axes aligned) and shear stresses represent lateral quadrupole sources (axes perpendicular). This qualitative analysis is the foundation of Lighthill's analytical solution to Equation 2.4, which is Equation 2.5 below and represents a distribution of quadrupoles of strength $-\frac{\partial T_{ij}}{\partial x_j}$ per unit volume.

$$\rho - \rho_0 = \frac{1}{4\pi a_0^2} \frac{\partial^2}{\partial x_i \partial x_j} \int T_{ij}\left(\vec{y}, t - \frac{r}{a_0}\right) \frac{d\vec{y}}{r} \tag{2.5}$$

Here, ρ_0 is the density of the fluid at rest and $r = |\vec{x} - \vec{y}|$, where $\vec{x}$ is the position of an observer and $\vec{y}$ is the position of a fluid element within the integration region. The integral may be carried out over the region where bulk flow is significant, and so if the bulk flow field is exactly known the fluctuation properties of the external acoustic medium can be considered known.

This solution, Equation 2.5, requires the assumption of an unbounded medium, and therefore is not sufficient for sound generated by a wing or turbine blade; it does not account for the effects of rigid surfaces on the bulk flow, nor the effects of reflections of acoustic waves at rigid surfaces. For this purpose one must turn to later analyses.

2.1.2 The Influence of Solid Boundaries

Curle [26] extended the theories developed by Lighthill to include the influence of solid boundaries on aerodynamically generated sound, acknowledging, as Lighthill did, how significant an influence solid boundaries might have. Curle's analysis also begins with the exact governing equation of the form developed by Lighthill, Equation 2.4. His approach here diverges from Lighthill's, though, as he turns to the most general solution to the inhomogeneous wave equation, in this case taking the form below.

$$\rho - \rho_0 = \frac{1}{4\pi a_0^2}\int_V \frac{\partial^2 T_{ij}}{\partial x_i \partial x_j}\frac{d\vec{y}}{|\vec{x}-\vec{y}|} + \frac{1}{4\pi}\int_S \left[\frac{1}{r}\frac{\partial \rho}{\partial n} + \frac{1}{r^2}\frac{\partial r}{\partial n}\rho + \frac{1}{a_0 r}\frac{\partial r}{\partial n}\frac{\partial \rho}{\partial t}\right] dS(\vec{y}) \qquad (2.6)$$

Here, S is the surface of a solid boundary and $\vec{n}$ is the outward normal from the fluid (or the inward normal to the surface). All flow variables on the right hand side of Equation 2.6 are taken at retarded time $t - r/a_0$ to account for the propagation delay between source and observer. After significant manipulation, and ultimately the inclusion of a zero normal velocity boundary condition at the surface, the general solution above is reformulated into the more intuitive form

$$\rho - \rho_0 = \frac{1}{4\pi a_0^2}\frac{\partial^2}{\partial x_i \partial x_j}\int_V T_{ij}\left(\vec{y}, t - \frac{|\vec{x}-\vec{y}|}{a_0}\right)\frac{d\vec{y}}{r} - \frac{1}{4\pi a_0^2}\frac{\partial}{\partial x_i}\int_S P_i\left(\vec{y}, t - \frac{r}{a_0}\right)\frac{dS}{r}, \qquad (2.7)$$

which notably reduces to Lighthill's quadrupole solution for an unbounded flow. Here, $P_i = n_j p_{ij}$ is the inward normal component of the *real* stress tensor—as opposed to the Lighthill stress tensor—at the surface. Thus, the second term on the right hand side of Equation 2.7, which differentiates it from Lighthill's solution, represents a distribution of dipoles on the bounding surface of strength equal to the normal force per unit area. The acoustic field is the sum of a contribution from a volume distribution of quadrupoles due to the Lighthill stress fluctuations and a contribution from a surface distribution of dipoles due to surface point-force fluctuations. The solution is again exact, making no assumptions about the stress-strain relation, and only assuming that the normal velocity of the surface and fluid at the surface is zero. This implies that the surface is fixed, or at least not vibrating out of its local tangential plane; this is an accurate assumption in airfoil applications, including wind turbine noise.

A dimensional analysis is used to show the relative contribution of the quadrupole volume distribution as compared to the dipole distribution. For a flow of length scale l and velocity scale V, on a dimensional basis, Lighthill predicts the sound power due to such a quadrupole volume distribution to scale as

$$L_q \sim \rho_0 V^8 a_0^{-5} l^2. \tag{2.8}$$

This is the well established 8th power speed dependence of, for example, turbulent jet noise [48]. On the same dimensional basis, Curle predicts sound power produced by a surface distribution of dipoles to scale as

$$L_d \sim \rho_0 V^6 a_0^{-3} l^2. \tag{2.9}$$

Thus, for similar flows and if the effects of Reynolds number are not significant, the relative contribution of the two sources is

$$\frac{L_q}{L_d} \sim \left(\frac{V}{a_0}\right)^2 = M^2. \tag{2.10}$$

This means that the relative efficiency of the volume distribution of quadrupoles will increase with Mach number M squared, and that at low Mach number—as is the case for wind turbine aeroacoustics—the dipole distribution is dominant. Amiet [4, 7] uses only the dipole argument in his analytical models of thin airfoil noise, ignoring quadrupole sources completely, and achieves strong agreement with experiment (a more thorough analysis of Amiet's work is given in Section 2.1.4). Based on Amiet's experimental Mach number, this seems to indicate that the dipole distribution contribution dominates in flow regimes relevant to wind turbine acoustics.

2.1.3 Boundaries in Arbitrary Motion: The Ffowcs Williams-Hawkings Equation

Ffowcs Williams and Hawkings [80] extend the foundational aeroacoustics analysis of Lighthill and Curle to the more general case of a bounding surface in completely arbitrary motion. In contrast, Curle's analysis was based on the assumption of zero normal velocity at the surface, which restricts the body to the particular cases of either rigidity or in-plane surface vibration. The Ffowcs Williams and Hawkings equation is then perhaps the most general formulation of the governing equations in aeroacoustics, while still being an exact formulation of the Navier-Stokes equations.

It is derived through a significantly different approach than that of either Lighthill or Curle, as the inhomogeneous wave equation (Eqn. 2.4) is not the basis of the analysis. Derivation begins with a sort of thought experiment, where mathematical surfaces in an unbounded flow field represent real, bounding surfaces. A volume is considered where a surface S with sides 1 and 2 divides a volume V into regions 1 and 2. The surface is first defined in such a way that it represents general discontinuities in the mass and momentum conservation equations at the surface. As such, its mathematical form is that of a distribution of mass and momentum sources, given below.

$$\frac{\partial \rho}{\partial t} + \frac{\partial}{\partial x_i}(\rho u_i) = \left[\rho\left(u_i - v_i\right)\right]_{(1)}^{(2)} \delta(f) \frac{\partial f}{\partial x_i} \tag{2.11a}$$

$$\frac{\partial}{\partial t}(\rho u_i) + \frac{\partial}{\partial x_j}\left(\rho u_i u_j + p_{ij}\right) = \left[p_{ij} + \rho u_i\left(u_j - v_j\right)\right]_{(1)}^{(2)} \delta(f) \frac{\partial f}{\partial x_j} \tag{2.11b}$$

Here, $\delta(f)$ is the Dirac delta function, $\vec{u}$ is the fluid velocity, $\vec{v}$ is the surface velocity, the notation $[A]_{(1)}^{(2)}$ denotes the difference in the quantity A on either side of the surface, and the function $f(\vec{x})$ is equal to zero at the surface, positive on side 2 of the surface, and negative on side 1 of the surface. Thus, ∇f is normal to the surface and points into region 2. Note that the nomenclature changes slightly after this section, where the co-ordinate frames will typically be fixed to an airfoil surface. The nomenclature used for the remainder of this dissertation is detailed in the sections that follow.

The mathematical surface, represented by mass and momentum source distributions in the modified continuity and momentum equations above, are given physical meaning once the impermeability condition $u_n = v_n$ is imposed. Additionally, the surface is assumed to enclose region 1, the fluid within the surface is assumed to be at rest and flow variables within the surface are set equal to the free stream conditions, i.e. $\vec{u} = 0$, $\rho = \rho_0$ and $p_{ij} = 0$ within the surface. The relations of Equation 2.11 then simplify to a description of the non-trivial flow conditions outside the surface,

$$\frac{\partial \rho}{\partial t} + \frac{\partial}{\partial x_i}(\rho u_i) = \rho_0 v_i \delta(f) \frac{\partial f}{\partial x_i} \tag{2.12a}$$

$$\frac{\partial}{\partial t}(\rho u_i) + \frac{\partial}{\partial x_j}\left(\rho u_i u_j + p_{ij}\right) = p_{ij} \delta(f) \frac{\partial f}{\partial x_j}. \tag{2.12b}$$

These equations are then combined by taking the time derivative of the first and the divergence of the second in order to eliminate the ρu_i term, giving

$$\frac{\partial^2 \rho}{\partial t^2} - a_0^2 \nabla^2 \rho = \frac{\partial^2 T_{ij}}{\partial x_i \partial x_j} - \frac{\partial}{\partial x_i}\left(p_{ij}\delta(f)\frac{\partial f}{\partial x_j}\right) + \frac{\partial}{\partial t}\left(\rho_0 v_i \delta(f) \frac{\partial f}{\partial x_i}\right). \tag{2.13}$$

Here, $T_{ij} = \rho u_i u_j + p_{ij} - a_0^2 \rho \delta_{ij}$ is again Lighthill's stress tensor. This is referred to as the Ffowcs Williams-Hawkings (FW-H) equation. The second and third terms on the right hand side of the FW-H equation differentiate it from the form of the inhomogeneous wave equation used by Lighthill and Curle. They represent dipole and monopole acoustic sources originating from the pressure distribution on and acceleration of the surface, respectively. Thus, the generalization to an arbitrarily moving surface allows for the arbitrary definition of the surface velocity $\vec{v}$ and results in the addition of a monopole distribution about the surface equal in strength to the acceleration of the surface; the term vanishes for a surface moving with a constant velocity. The authors' solution to the equation, which requires no further assumptions, reveals a second differentiating factor, so to speak: Each source is adjusted by a convective amplification term $|1 - M_{rel}|^{-1}$, where M_{rel} is the Mach number of the source (quadrupole, dipole, or monopole element) projected along the source-observer direction.

2.1.4 Acoustic Scattering by a Flat Plate Airfoil

The theoretical work of Lighthill, Curle, and Ffowcs Williams and Hawings is extremely general, and is not very practical unless the flow field is very well known. Amiet [3, 4, 7, 6], Paterson [70], and Schlinker and Amiet [74] apply these general theories—particularly that of Curle—to the case of flow around a flat plate airfoil. By making some assumptions about the geometry of the aerodynamic body and the turbulence field, a much more manageable model is derived for the noise mechanisms relevant to the proposed study.

The sound produced by a flat plate, finite-span airfoil in a turbulent stream is first considered. The mean flow u_{in} is in the positive x direction with the airfoil span aligned with the y axis, as depicted in Figure 2.1 (the nomenclature $e_{\text{x,y}}$ for the respective axis labels is to distinguish between coordinate frames; see Figure 2.6). The airfoil has a span *2d* and chord length *2b*. The vertical velocity fluctuations $w(x, y, t)$ impinging on the airfoil are assumed frozen in a translating coordinate frame given by $x' = x - u_{\text{in}}t$. For a turbulence field with spatial Fourier components $\hat{w}(k_x, k_y, t)$ in the airfoil fixed frame, the temporal Fourier transform of the difference in pressure across the flat airfoil is given below [3].

$$\Delta\hat{P}(x, y, \omega) = 2\pi\rho_0 b \int_{-\infty}^{\infty} \hat{w}(k_x = K_x, k_y) g(x, k_x = K_x, k_y) e^{ik_y y} dk_y \tag{2.14}$$

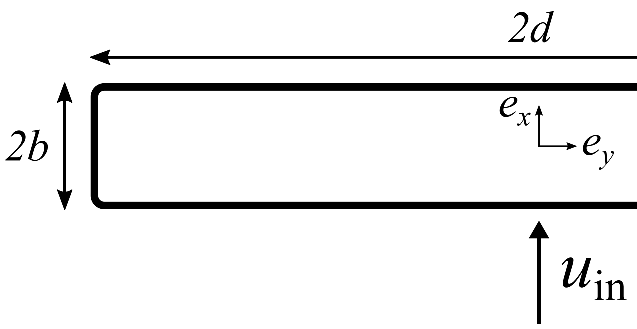

Figure 2.1: Flow orientation, airfoil dimensions, and coordinate system for the analysis of R.K. Amiet.

In Equation 2.14, $\omega = 2\pi f$ is the angular frequency and $K_x = -\frac{\omega}{u_{\text{in}}}$. The latter shows an important result of the derivation, which is that a given angular frequency component ω of the pressure jump $\Delta\hat{P}$ is produced entirely by the turbulence component with x axis wavenumber $k_x = -\frac{\omega}{u_{\text{in}}}$. This is a product of the frozen turbulence assumption, but can be expected to be at least a reasonable approximation. The time-oscillations of $\hat{w}(k_x, k_y, t)$ due to convection of the turbulence field are also absorbed in arriving at this result. The function $g(x, K_x, k_y)$ is the frequency dependent transfer function between the incident turbulent gust and the pressure on the airfoil surface.

The dipole term of Curle's result given in Equation 2.7 can then be derived by setting

$P_z = \Delta P$. It is noted that, in a physical sense, the pressure on either side of the airfoil might be used to derive a dipole distribution for the entire surface. However, because the airfoil is thin, the sum of the resulting dipole distributions would be exactly equivalent to this pressure jump dipole distribution.

The derivation is carried out using statistical quantities and spectra rather than time-series. For turbulence wavelengths significantly smaller than the span of the airfoil, it is shown that the power spectral density (PSD) S_{pp} of the far field noise at a location (x, y, z) is given by

$$S_{pp}(\vec{x},\omega) = \left(\frac{\omega z \rho_0 b}{a_0 \sigma^2}\right)^2 U d\pi \left|\hat{L}(\vec{x}, K_x, \frac{\omega y}{a_0 \sigma})\right|^2 \Phi_{zz}(K_x, \frac{\omega y}{a_0 \sigma}). \tag{2.15}$$

Here, $\Phi_{zz}(k_x, k_y)$ is the energy spectrum of the vertical velocity fluctuations, $\sigma = \sqrt{x^2 + \beta(y^2 + z^2)}$, and $\beta = \sqrt{1 - M^2}$. The function $\hat{L}(x, K_x, k_y)$ is a chordwise unsteady loading function defined as

$$\hat{L}(\vec{x}, K_x, k_y) = \int_{-b}^{b} g(x_0, k_x, k_y) e^{-i\omega x_0 (M - x/\sigma)/a_0 \beta^2} dx_0. \tag{2.16}$$

Physically, the pressure jump distribution is resultant from the incident vertical velocity fluctuations as well as an additional distribution required for satisfaction of the Kutta condition at the leading and trailing edges of the airfoil [74]. Another important result is illuminated by Equation 2.15, which is that an observer predominantly hears the effects of the turbulence with y axis wavenumber $k_y = \frac{\omega y}{a_0 \sigma}$. This result is explained geometrically by the fact that this turbulence wavenumber produces an acoustic wavefront that is perpendicular to the source observer line, so the acoustic signals produced at different spanwise locations arrive at the observer in phase. Contrarily, sound due to other y axis wavenumber components interferes randomly at the observer location.

For the purposes of the proposed study, scaling of Equation 2.15 and radiation directivity are of particular importance. That is, the behavior of the far field sound as a function of inflow speed, turbulence intensity, and observer position are pivotal in predicting wind turbine aeroacoustic noise generation patterns. Several other parameters such as angle of attack are of interest, of course, and these are outlined in the sections that follow. Amiet shows that for a von Kármán inflow turbulence spectrum, the sound intensity I scales as

$$I \sim M^5 I_T^2. \tag{2.17}$$

Here, I_T is the *local* turbulence intensity given by Equation 2.18, where σ_i is the root-mean-square fluctuation velocity along the i axis. It is important to note that when applied to wind turbines, there is a turbulence dilation effect due to the motion of the blades. That is, the turbulence intensity (Equation 2.18) observed by a blade section is reduced by a factor of u_{in}/U_w relative to the turbulence measurement in the stationary frame, where U_w is the mean wind speed and u_{in} is the local inflow speed to a blade section due to the vector addition of the wind speed and the rotational motion of the blade. This factor can approach 10 for modern, large wind turbines.

$$I_T = \frac{1}{u_{\text{in}}}\left[\frac{1}{3}\left(\sigma_x^2 + \sigma_y^2 + \sigma_z^2\right)\right]^{1/2} \tag{2.18}$$

Amiet [7] later extended this theory to include noise due to turbulence in the boundary layer of the airfoil itself. The function is generally similar to the form of Equation 2.15 and is not shown here. Schlinker and Amiet [74] derive the frequency dependent emission directivity of this analytical function for trailing edge noise. While the full directivity expression is fairly complex and will lend little insight by inspection (discussed fully in Section 6.2.4), certain limiting cases are of interest. For turbulence wavelengths that are large with respect to the airfoil chord ($K_x b \ll 1$) and for an observer in the acoustic far-field of the airfoil ($K_x r \gg 1$), the acoustic emission pattern is dipole-like, depicted in Figure 2.2.

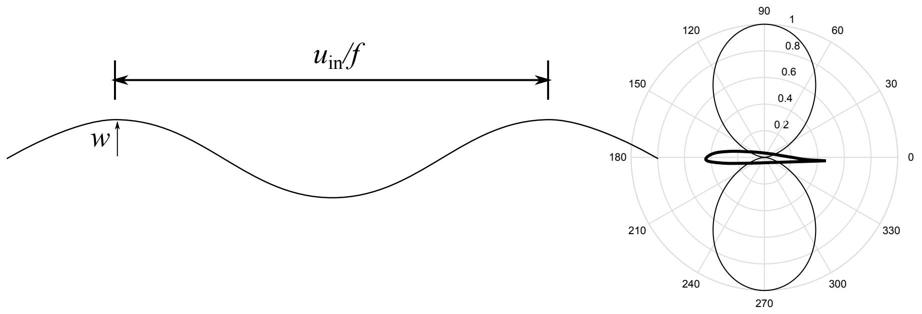

Figure 2.2: Low frequency directivity pattern for an acoustic frequency f and turbulence convection speed u_{in}.

For turbulence wavelengths on the order of or smaller than the airfoil chord, the emission pattern has a preferential direction opposite the scattering edge [53, 65]. That is, noise generated by inflow turbulence crossing the trailing edge will preferentially be directed upstream, and noise generated by boundary layer turbulence crossing the leading edge will preferentially be directed downstream; the directivity patterns are inverted as shown in Figure 2.3. A thorough assessment of theoretical airfoil noise directivity is given in Chapter 6, including a derivation of the exact, frequency dependent directivity factor.

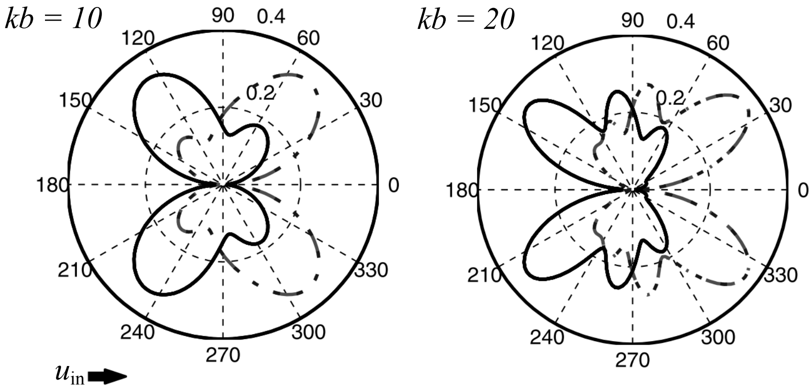

Figure 2.3: Theoretical directivity patterns for turbulent boundary layer trailing edge noise (solid lines) and turbulent inflow noise (dashed lines). The non-dimensional parameter kb—where k is the acoustic wavenumber and b is the airfoil semi-chord—is equal to 10 at acoustic frequencies of approximately 340 Hz for wind turbine noise ($c \sim 1m$). Figure credit to Moreau et al. [53].

2.1.5 Semi-empirical Prediction of Airfoil Noise

The well known experimental aeroacoustics work of Brooks, Pope, and Marcolini [15] are summarized here. Brooks et al. conducted their experimentation in the aeroacoustic wind tunnel facility at NASA's Langley Research Center. The purpose of the study was to develop effective non-dimensionalized empirical models that reduce the number of variables to be considered in prediction of airfoil self noise. Emphasis is then placed on trends and scaling laws. In the tests, NACA-0012 airfoils of six chord lengths ranging from 2.5 to 30 cm were placed in an anechoic wind tunnel with flow speeds up to 71 m/s, corresponding to a Mach number of 0.21. Angles of attack were swept from 0° to 25°. Finally, trailing edge extensions of various thicknesses were added for investigation of trailing edge bluntness effects. For a sampling of this test matrix, hot-wire measurements of boundary layer profiles near the airfoil trailing edges were carried out, resulting in empirical formulas for boundary layer thickness δ, displacement thickness δ^*, and momentum thickness θ as a function of chord Reynolds number Re and angle of attack α—the boundary layer parameters having been previously used successfully in prediction self noise mechanisms [74].

The hot-wire anemometer was removed, and acoustic experimentation was conducted into airfoil self noise. The term "self noise" refers to aerodynamic noise generation mechanisms that would be present in a perfectly laminar inflow field. That is, self noise is entirely generated by the aerodynamic body—inflow turbulence noise is not considered self noise, for example. Brooks et al. place their focus on five self noise mechanisms:

(1) Turbulent Boundary Layer Trailing Edge Noise – Noise generated due to turbulence in the boundary layer of the airfoil passing over the discontinuity of the trailing edge; the turbulence being a result of inherent flow instability for relatively high Re.

(2) Laminar Boundary Layer Vortex Shedding Noise – Narrowband noise arising from coherent vortex shedding structures at the trailing edge of an airfoil with a laminar boundary layer.

(3) Separation Stall Noise – Noise radiated from the surface of an airfoil during separated flow conditions, generally for high angles of attack.

(4) Trailing Edge Bluntness Noise – Noise due to small scale vortex shedding at a trailing edge of finite thickness.

(5) Tip Vortex Formation Noise – Noise due to tip vortex turbulence structures interacting with the outboard potions of a wing or blade.

Acoustic tests were carried out in an anechoic wind tunnel, and further extraneous noise reduction was accomplished by coherent processing of data from multiple microphones. This allowed for noise source identification as well, as the peak time delay in a cross correlation measurement directly corresponds to the difference in propagation time from a source location to the two microphone locations. An interesting result, which supports the predictions of Amiet, is a strong *anticorrelation* peak measured between microphones on opposite sides of the airfoil, consistent with dipole radiation patterns.

Using the gathered data, empirical models were developed for the five self noise mechanisms listed above. Data is reduced by the use of several non-dimensional parameters, including the chord Reynolds number and freestream Mach number. Use of the reduced frequency, or Strouhal number based on a boundary layer length scale, is used for spectral scaling. Amplitude scaling laws were also established, which are founded on the theoretical results of Ffowcs Williams and Hall [79]. Unscaled and scaled experimental results for the 30.5 cm chord airfoil are shown in each panel of Figure 2.4. Here, the scaled amplitudes are given by Equation 2.19, where r is the observer distance, d is the semi-span of the airfoil section, and δ^* is the boundary layer displacement thickness. Curves were then fitted to the remaining variation, yielding general prediction models for both tripped and untripped flows that require only angle of attack, Reynolds number, Mach number, and boundary layer length scales as inputs.

$$\mathrm{SPL}_{1/3,scaled} = \mathrm{SPL}_{1/3} - 10\log_{10}\left[M^5 \frac{2\delta^* d}{r^2}\right] \tag{2.19}$$

In order to test the general applicability of the measured trends, only a portion of the gathered data was used to develop the models. The resulting models are then assessed against the remaining experimental data. The dataset is extensive, so varying degrees of success are achieved. Spectral shapes are qualitatively well predicted in most of the of the cases shown, and third-octave absolute levels are typically predicted to within 3-5 dB and often within 1-3 dB. Predictions are least accurate for the smallest airfoils at high angles of attack, with some cases missing the mark by more than 10 dB. Laminar boundary layer vortex shedding noise predictions are also inaccurate in some cases, though this is not of particular concern in wind turbine acoustics [35, 59].

Predictions were also made for comparison to three external aeroacoustic data sets, for which spectral agreement was usually within 1-3 dB. Figure 2.5 shows the models' application to the data of Schlinker and Amiet [74]. This gives some confidence in the general applicability of the empirical relations. It is noted that all airfoils used in validation of prediction models were NACA 0012 or of a very similar profile. Application to airfoils of more general cross section can be accomplished using the TNO-Blake model [58, 45], which calculates more detailed boundary layer characteristics and contains less empiricism than that of Brooks et al.

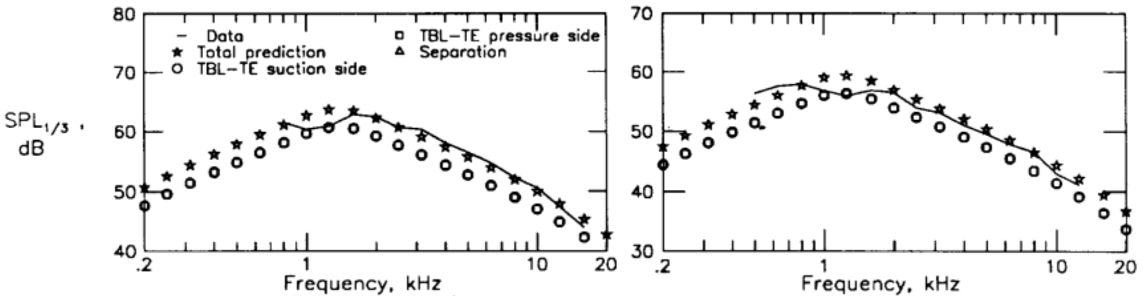

(a) U = 71.3 m/s

(b) U = 55.5 m/s

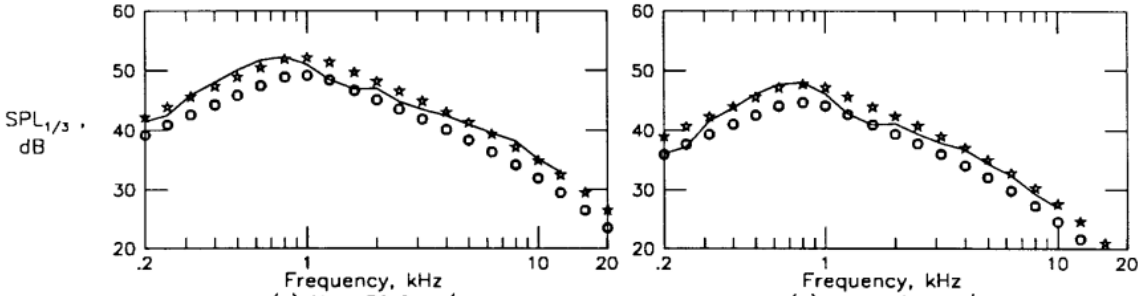

(c) U = 39.6 m/s

(d) U = 31.7 m/s

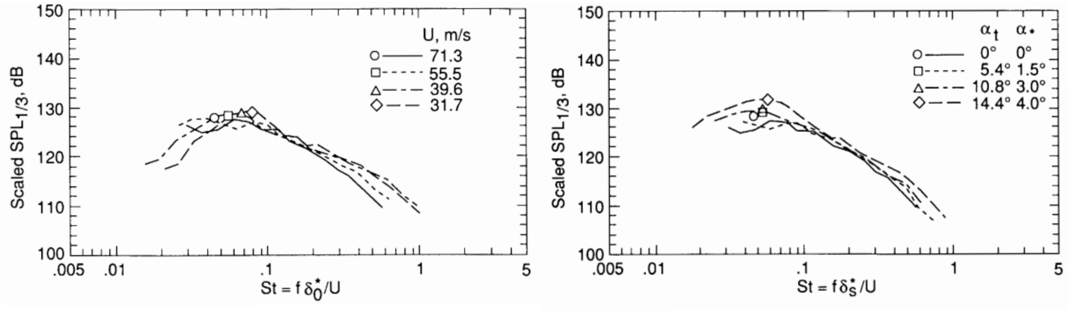

Figure 2.4: Unscaled acoustic data (top and middle) and corresponding scaled acoustic data (bottom) 30.5 cm NACA 0012 airfoil. Figure credit to Brooks et al. [15].

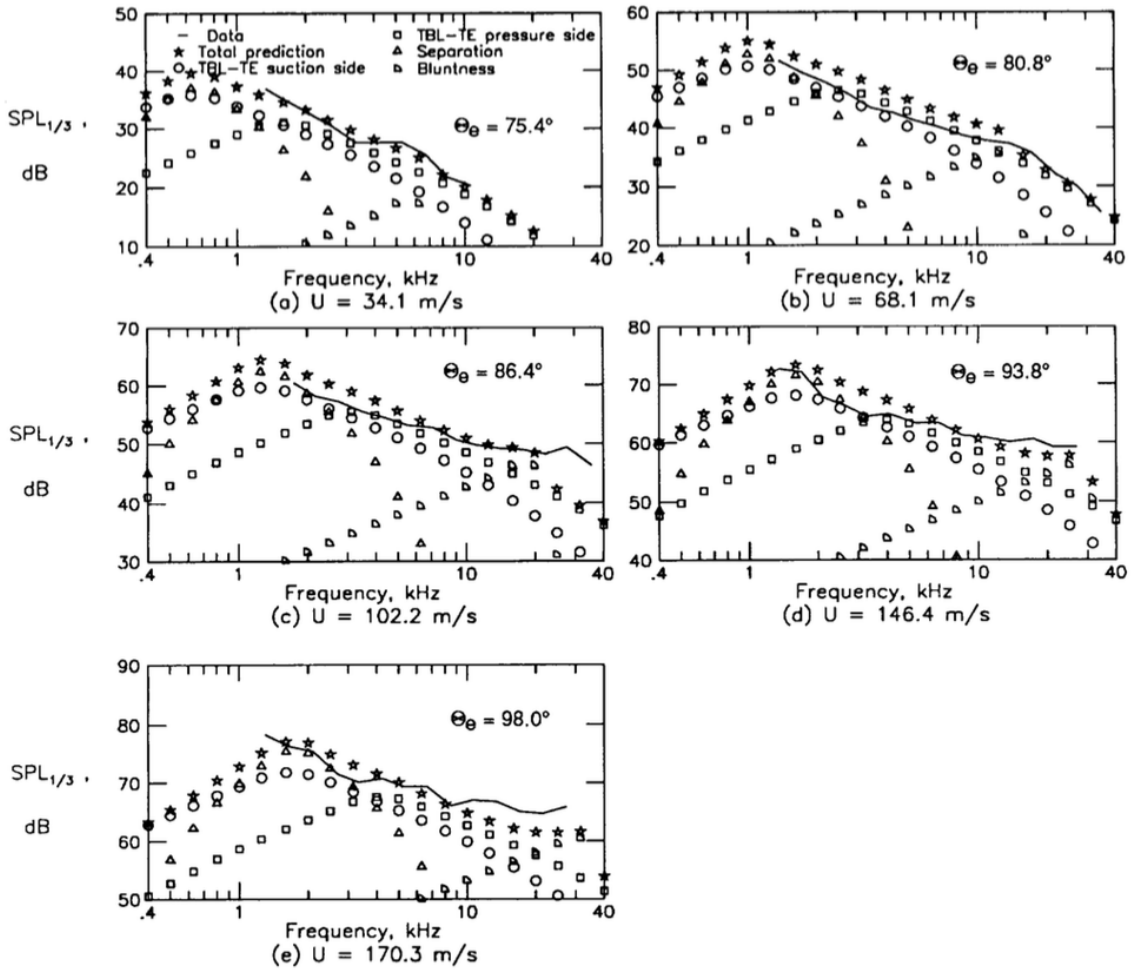

(a) U = 34.1 m/s

(b) U = 68.1 m/s

(c) U = 102.2 m/s

(d) U = 146.4 m/s

(e) U = 170.3 m/s

Figure 2.5: Comparison of Brooks, Pope, and Marcolini predictions to the data of Schlinker and Amiet. The parameter Θ_e is the retarded observer position [74]. Figure credit to Brooks et al. [15].

2.2 Wind Turbine Acoustic Noise Prediction

Significant research has been conducted into wind turbine acoustics over the past few decades. Particular interest has been placed on modeling and prediction of wind turbine noise for design purposes, such as noise reduction, wind farm planning, and to optimize the trade-off between noise and power production. This dissertation is intended to further the understanding of wind turbine noise emission, so these models and the results of their respective experimental validation are of particular interest.

The acoustic system of a wind turbine is very complex. The range of aerodynamic length scales of interest varies from the airfoil boundary layer length scales on the order of millimeters to the atmospheric surface layer length scales on the order of tens or hundreds of meters. For this reason, prediction of wind turbine noise is accomplished by making simplifying assumptions about the system. The aeroacoustics theories outlined in Section 2.1 provide the foundation for wind turbine noise prediction models that have been developed, which are outlined here. Development of these models is generally accompanied by experimental validation, which will be highlighted here for the purpose of comparison to the proposed experimental methods.

2.2.1 Co-ordinate Frames

It is now useful to define the coordinate systems to be used for the remainder of this dissertation. Two coordinate frames will generally be referred to: the blade/airfoil frame—depending on context—and the stationary frame. Figure 2.6 depicts the two frames and the nomenclature that will be used hereafter. In general, the subscripts “x” and “1” will refer to the flow-wise direction in the blade and stationary frames, respectively. Similarly, the subscripts “z” and “3” will refer to the vertical directions. Also note that the blade frame coordinates are fixed to the blade, so in the case of a finite angle of attack, $u_x \neq u_{in}$.

2.2.2 F.W. Grosveld’s Model

In 1985, Grosveld [35] provided one of the first prediction models for wind turbine noise not based simply on empirical results. His model includes three separate noise mechanisms, which are turbulent boundary layer trailing edge noise, trailing edge bluntness noise, and turbulent inflow noise. The first two of these mechanisms are explained in Section 2.1.5, though notably the work of Grosveld was conducted before that of Brooks et al. [15]. Turbulent boundary layer noise is predicted by the model of Schlinker and Amiet [74], originally applied to helicopter rotor noise. Trailing edge bluntness noise is predicted based on the scaling laws of Brooks’ earlier research [14] and a directivity function given by Howe [40]. Finally, turbulent inflow noise is predicted by the

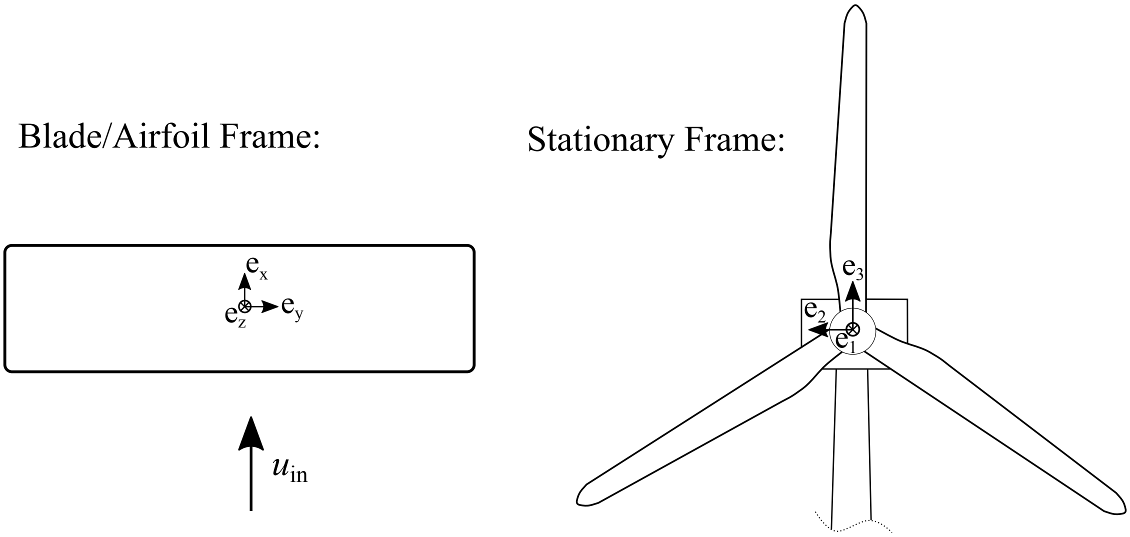

Figure 2.6: Illustration of the two coordinate frames to be used in the analysis of this dissertation. A cross within a circle represents the direction into the page.

low frequency approximation of a blade as a line of dipole—or point force—sources, as described by Lighthill [47] and consistent with the theories of Amiet [4] at low frequencies.

Grosveld [35] validates the model by comparison to experimental data acquired at four turbines, three of which have rotors downwind of the tower. Inflow turbulence characteristics were calculated by a simple model as a function of wind speed and height above the ground. No comparisons were made to observed turbulence conditions during testing. Acoustic measurements were conducted with individual microphones at various downwind or upwind distances. Despite the physical mechanisms that are missing from the model, predictions are generally within 4 dB. Spectral shape is also fairly well predicted, with a distinct feature being the narrow band peak due to trailing edge bluntness noise. A sampling of the predicted and measured spectra are shown in Figure 2.7.

A plot of the relative contribution from each of the three noise mechanisms for the two-bladed, upwind-rotor machine, referred to as the MOD-2 machine, is shown in Figure 2.8 and predicts turbulent inflow noise to be dominant. However, Lowson [49] points out that this result is produced in error. Grosveld allows for a tuning parameter on the turbulence inflow noise prediction,

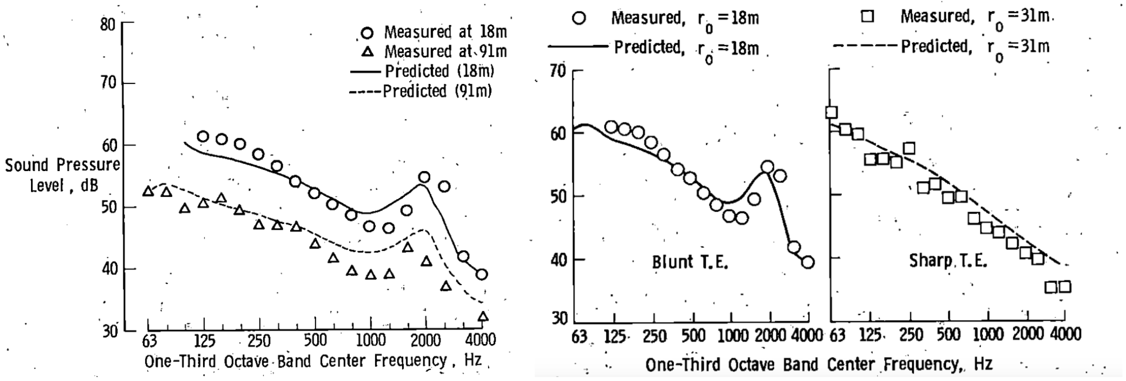

Figure 2.7: Grosveld's [35] predicted and measured sound levels for a US Wind Power 50 kW downwind-rotor machine. The far left plot shows the effect of observer distance on sound pressure level, and the center and right plot show the effect of blunt trailing edge and sharp trailing edge on sound pressure level, respectively. Figure credit to Grosveld [35].

which is tuned to match the measured spectra of one turbine—the measured data on the left plot of Figure 2.8. Grosveld fails to correct for the pressure doubling at the microphone board (see Section 3.3), meaning that the tuning parameter is tuned to data that was incorrectly amplified by 6 dB. It is therefore skewed towards a higher influence than the reality.

2.2.3 Semi-Empirical Prediction: Lowson's Model

Lowson [49] provides a prediction model that is based on blade discretization. That is, the blade is broken into finite segments such that each may be assigned an angle of attack, chord length, and local inflow speed that is approximately accurate for that segment. Noise levels are then summed to predict the total emission level of the turbine. Several physical mechanisms are included that have been omitted from the model of Grosveld, and particular consideration is given to inflow turbulence noise prediction. Lowson also provides an assessment of the complexities of wind turbine noise prediction beyond, for example, the simplifying assumptions of Grosveld [35] and Glegg [33] in their wind turbine noise model, or the simplifying assumptions of Amiet [4, 7] in his airfoil noise theory. Such concerns include the effect of finite blade thickness on high frequency noise, the influence of small scale inflow turbulence, and the effect of discrete frequency radiation

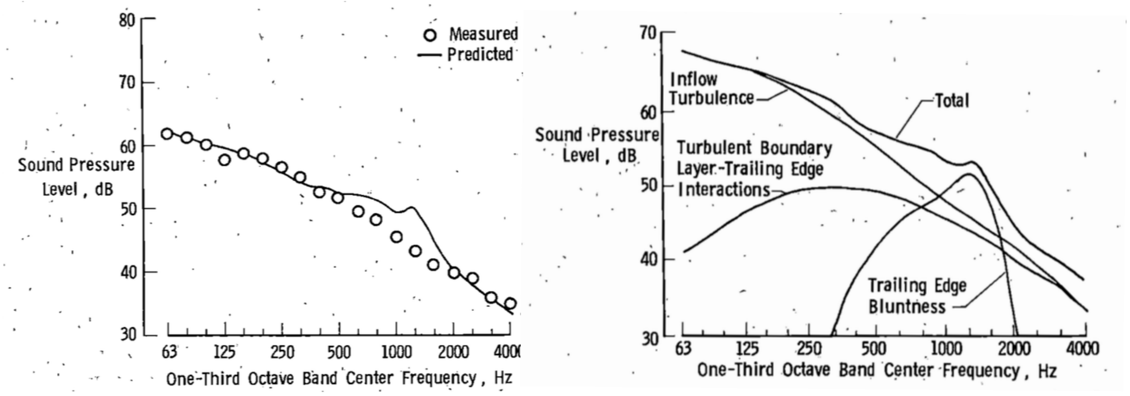

Figure 2.8: Grosveld's [35] predicted and measured spectra (left) and predicted relative contribution of three noise mechanisms (right) for the MOD-2 two-bladed, upwind-rotor turbine. The process leading to this prediction contains an error in that the inflow turbulence contribution was tuned improperly; the total noise and inflow turbulence contribution should be ∼6 dB lower. The difference in absolute levels is due to the difference in observer location between the plots. Figure credit to Grosveld [35].

at harmonics of the blade passing frequency, particularly in the case of downwind rotors.

In Lowson's model, the five self noise mechanisms characterized by Brooks, Pope, and Marcolini [15] are included. Each are modeled at least in part by the empirical results of that work. For this reason, Lowson's model is described as "semi-empirical", meaning that it draws from both empirical and analytical results. For example, turbulent boundary layer trailing edge noise is predicted by the scaling function of Brooks et al., which is originally based on the work of Ffowcs Williams and Hall [79].

$$\mathrm{SPL}_{1/3,Peak} = K + 10\log_{10}(M^5\delta^* d/r^2), \tag{2.20}$$

Above, $\mathrm{SPL}_{1/3,Peak}$ refers to the peak third-octave band sound pressure level, K is an empirical constant determined from the experimentation of Brooks et al. [15], and d is the semi-span of the airfoil section. The spectral shape function is based on a simplified form of the empirical results of Brooks et al. [15]. Trailing edge displacement thickness δ^* is based on a well established flat plate empirical relation, with a multiplying constant left as a tuning parameter. Lowson notes that the flat plate approximation should reasonably approximate the mean of the thinner pressure side boundary layer and the thicker suction side boundary layer, though the thickness of the section will tend to increase the displacement thickness as a whole.

Lowson's discussion of the matter of turbulent inflow noise is thorough, and is summarized here due to its relevance to the proposed study. Inflow turbulence noise is generated as a result of the fluctuating velocity field being converted into a fluctuating pressure field at the surface of the blade, which radiates as a distribution of dipoles according to the theories of Curle [26]. If the blade is subject to an incoming sinusoidal gust of wavelength λ_t, the pressure fluctuations at the surface of the blade will be of frequency $f = U_c/\lambda_t$, where U_c is the convection velocity of the gust. The radiated frequency is the same, so the radiated wavelength is then given by $\lambda_a = \lambda_t/M$. In the case of wind turbines, M is the local Mach number, which varies as a function of radial position, meaning that this frequency conversion varies along a turbine blade. One must also consider the influence of the rotor on the turbulence field itself. As Lowson notes, the streamline expansion process in the inflow to the rotor due to axial induction—the slowing of the flow resultant from streamwise thrust—will result in an increase in turbulence intensity and an altered turbulence spectrum from the free stream. This effect is not predicted by Lowson, but an approximation should be feasible based on some rudimentary wind turbine thrust calculations.

The frequency dependence of the turbulent inflow noise mechanism is also noted in the discussion of turbulent inflow noise, as radiation efficiency and directivity vary considerably depending on the relative scale of the turbulence with respect to the chord length. This variation was analyzed by Schlinker and Amiet [74] and is described in Section 2.1.4. A modified version of Amiet's model [4] is used in Lowson's predictions, where the low frequency approximation and high frequency approximation are combined into the form given by Equation 2.21.

$$\mathrm{SPL}_{1/3} = \mathrm{SPL}^H + 10\log_{10}\left(\frac{\mathrm{LFC}}{1+\mathrm{LFC}}\right) \tag{2.21a}$$

$$\mathrm{SPL}^H = 10\log_{10}\left(\frac{2dL}{r^2}\rho_0^2 a_0^4 M^5 \mathrm{I}_\mathrm{T}^2 \frac{(k/k_e)^3}{(1+(k/k_e)^2)^{7/3}}\right) + 78.4 \tag{2.21b}$$

$$\mathrm{LFC} = \frac{10 S^2 M \hat{\omega}^2}{\beta^2} \tag{2.21c}$$

$$S^2 \approx \left[\hat{\omega}/\beta^2 + (1 + 2.4\hat{\omega}/\beta^2)^{-1}\right]^{-1} \tag{2.21d}$$

Here, $\mathrm{SPL}_{1/3}$ is the one-third octave band sound pressure level relative to 20 μPa, and the constant 78.4 comes from normalization by the reference acoustic pressure 20 μPa and multiplication by a third-octave bandwidth. A rigorous derivation of this relationship is given in Section 6.2.1. The superscript H refers to the high frequency contribution, and LFC is a correction applied at low frequencies. The parameter d is again the semi-span of the airfoil section, L is the turbulence integral length scale, $\mathrm{I_T}$ is the local turbulence intensity, $k = \frac{2\pi f}{u_{\mathrm{in}}}$ is the local turbulence wavenumber, k_e is the energy-containing wavenumber scale (Section 6.2.1), and $\hat{\omega} = kb$. Equation 2.21d is an approximation to the compressible Sears function [70]. Lowson does not apply a directivity function in his formulation for simplicity.

Lowson [49] conducted a validation study of the complete prediction model using experimental measurements on three full scale wind turbines. The wind turbines include a two-bladed, 2.5 MW machine of 91.44 m diameter (data also used by Grosveld [35]), a three-bladed, 500 kW machine of rotor diameter 39 m, and a three-bladed, 300 kW machine of rotor diameter 39 m. All three machines have rotors upwind of the tower. Acoustic data consists of single microphone measurements. A logarithmic wind speed profile is assumed, and turbulence intensity is given as a simple function of wind speed and approximate roughness height of the local landscape. Turbulence integral length scale is left as a tuning parameter based on acoustic measurements. The turbulence spectral shape is assumed to be a von Karman spectrum, consistent with the models of Amiet. Like Grosveld, Lowson does not provide measured validation for the turbulence conditions used in predictions.

Lowson's predictions for the same data set used by Grosveld (see Figure 2.8) are shown in Figure 2.9. The turbine being measured is the 2.5 MW two-bladed machine. The predictions show a much more balanced contribution from turbulent boundary layer trailing edge noise and turbulent inflow noise than the predictions of Grosveld (which were shown to be in error, see Section 2.2.2). The turbulence length scale used is 100 m, and the turbulence intensity is approximately 10% at hub height based on Lowson's formulas.

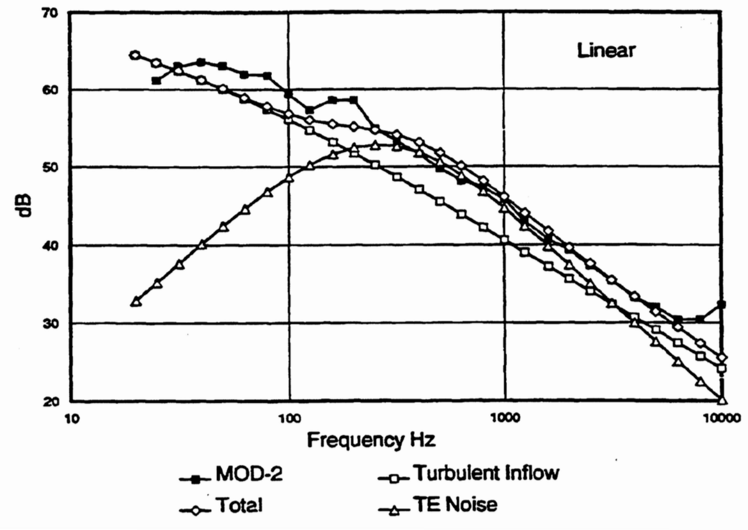

Figure 2.9: Predicted contributions of turbulent inflow noise and trailing edge noise, and measured spectra. Compare to Figure 2.8 for the same dataset. MOD-2 refers to measurements on the MOD-2 two-bladed, upwind-rotor, 2.5 MW turbine. Figure credit to Lowson [49].

2.2.4 Improvements to Semi-empirical Prediction

Similar semi-empirical models have been developed by Fuglsang et al. [31] and Moriarty et al. [59, 57]. The prediction code of Moriarty et al. was developed to be included in NREL's FAST aeroelastic simulator (this noise prediction model will hereafter be referred to as the FAST model). Similar to Lowson's model, the FAST model uses the empirical relations of Brooks et al. [15] to predict self noise and the same approximation of the Amiet model [4] to predict turbulent inflow noise. Two differentiating factors are included compared to Lowson's model. The first is a correction to turbulent inflow noise prediction for finite airfoil thickness and angle of attack developed by Guidati et al. [36]. The second is that trailing edge boundary layer thickness is calculated based on the 2d airfoil simulation code XFOIL, rather than by assuming a flat plat profile.

Predictions of the FAST model were compared to experimental results for two full scale wind turbines—a 50 kW downwind-rotor machine and a 600 kW upwind-rotor machine. Acoustic measurements were taken by a single microphone according to IEC Standard 61400-11 for the 50 kW turbine, and turbulence characteristics were assumed constant and based on the recommended values given by IEC 61400-11. For the case of the 600 kW turbine, three microphones were used—two downwind and one to the right of the turbine as viewed from upwind. Turbulence intensities at this turbine were based on sonic anemometer measurements 1.5 rotor diameters upwind. Figure 2.10 shows the predicted and measured spectra for these turbines, including the contributions from each of the noise mechanisms modeled.

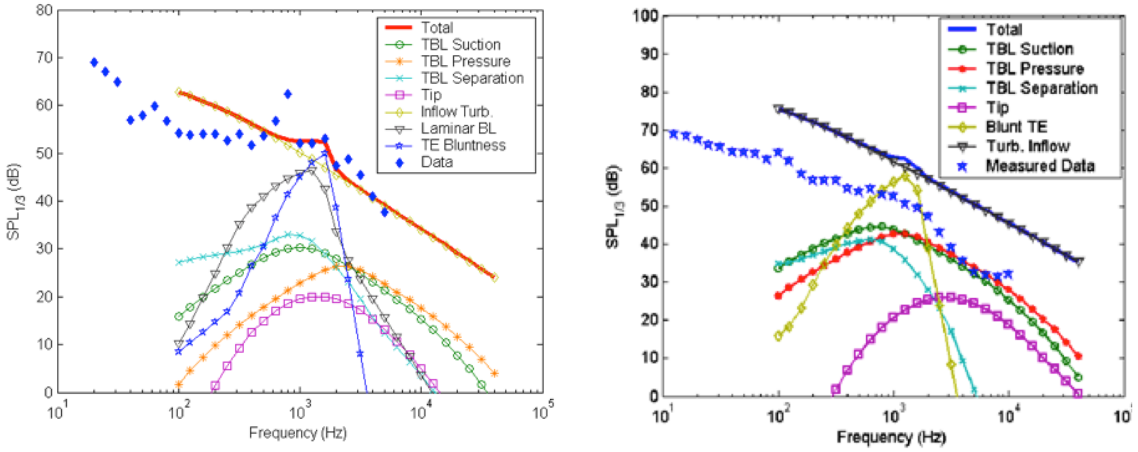

Figure 2.10: Predicted contributions and measured spectra for the AOC 50 kW turbine (left) and for the CART-2 600 kW turbine (right). Figure credit to Moriarty et al. [59, 57].

Agreement is fairly good for the 50 kW turbine, though the model overpredicts the noise at low frequencies by as much as 10 dB. The turbulent inflow noise prediction is higher than the total measured levels in the low frequency region for this turbine. Predictions are considerably less accurate for the 600 kW turbine, where results are overpredicted by 10 dB or more across the spectrum. Turbulence noise is dominant for most of the spectrum in the predicted level for this turbine, and is higher than the total measured level across the spectrum. This is expected to be due to the method of calculating turbulence intensity, particularly the integration time used.

Moriarty et al. discuss the issue of calculating turbulence intensity and mean wind speed for prediction of wind turbine noise. The complexity arises from the large scale turbulence common in surface layer turbulence and in particular at the NWTC, where the experiments of Moriarty et al. [59, 56] were conducted and where the experiments of this dissertation research are conducted. The largest-scale turbulent fluctuations occur over long periods of time—often several minutes. Moriarty gives the example of wind speeds shifting from 1 m/s to 10 m/s over a one-minute period, for which simple calculations would yield a mean wind speed 5.7 m/s and turbulence intensity of 47%. This issue is addressed in Section 4 by a novel method of calculating the turbulence levels for shorter periods of time based on in situ measurements with blade-mounted accelerometers.

2.2.5 Trailing Edge Noise Prediction and Measurement

The wind turbine noise studies that have been described thus far illustrate that single microphone measurements leave much unknown about a wind turbine as a noise source. Tuning of predictions to results [35, 49] limits the predictive power of the model, and any inaccuracy in prediction becomes difficult to explain with confidence. On a fundamental level, there are more unknowns (six noise mechanisms, for example) than there are sources of information (one microphone). Oerlemans et al. [65, 64] address this issue using a 148-element microphone array for source localization, and eight single-microphone elements in a 240 m ring about the turbine for directivity assessment. Measurements were taken of a 2.3 MW, 94 m rotor diameter turbine and a 850 kW, 54 m rotor diameter turbine. The experimental setup is shown in Figure 2.11. An additional feature of the test is that for the 850 kW turbine, the surface of one blade was cleaned, one blade was left untreated, and one blade was intentionally tripped near the leading edge using 0.4 mm zig-zag tape on the suction and pressure sides of the airfoil.

Using array measurements, the effect of each surface treatment on noise generation was assessed, showing that the tripped boundary layer produced 3.6 dBA increase in noise from this blade, but the untreated blade was only slightly (0.1 dBA) louder than the cleaned blade, with the spectral difference above 2 kHz. Oerlemans et al. [65] point out that this small effect may simply be due to the small amount of soiling that had accrued on the untreated blade. Contrarily, the 3.6 dBA increase of the tripped blade is quite significant.

Perhaps the most influential result of this research is that the noise from the downward

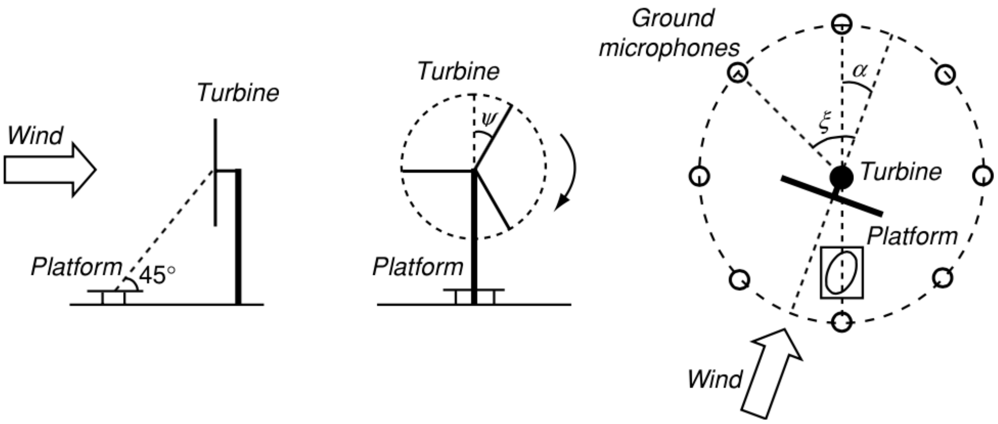

Figure 2.11: Experimental setup used by Oerlemans et al. for source localization and directivity assessment. The platform shown is a 148-element microphone array. Figure credit to Oerlemans et al. [64].

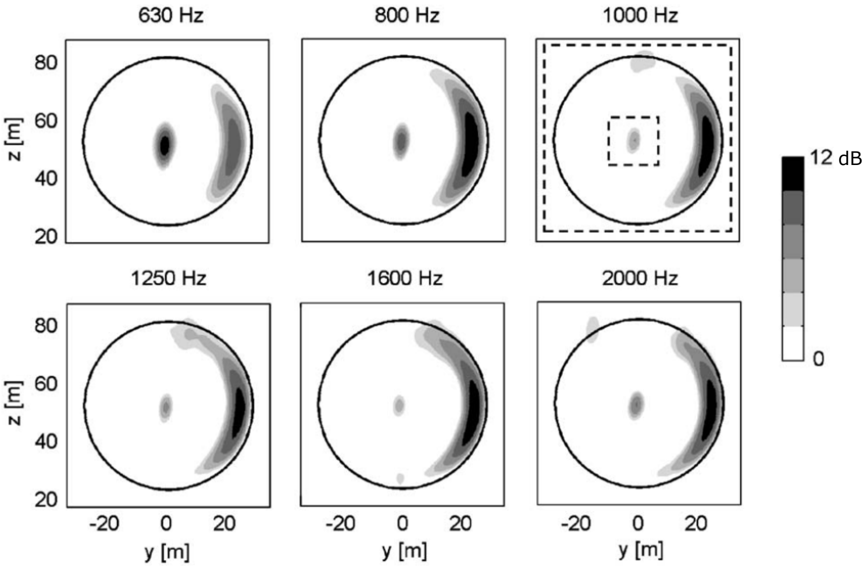

Figure 2.12: Noise maps generated from upwind array measurements of a 850 kW wind turbine. Figure credit to Oerlemans et al. [65].

passing blade—as measured at the array position—was dominant by roughly 15 dB, as seen in Figure 2.12. Oerlemans hypothesizes that this is consistent with the directivity patterns of trailing edge noise amplified by the relative motion of the source (convective amplification), which is then tested by the implementation of a semi-empirical code that models *only* trailing edge noise. Trailing edge noise prediction is based on the empirical relations of Brooks et al. [15] but with a modified directivity pattern. Predictions agree well with experimental observations for source localization and directivity. That is, the array measurements were well reproduced using the simulated data at the array element locations, and sound levels were reproduced at the eight single-microphone measurement locations to within 2 dB. Broadband amplitude modulation is also predicted to within a few dB, and qualitative agreement is very good. Figure 2.13 illustrates predicted and measured amplitude modulation and directivity.

The level of agreement between simulation and experiment implies that the assumption that trailing edge noise was the dominant noise mechanism is likely correct, particularly because little tuning of the model to observations was done. The only adjustment made based on observations was to the directivity pattern of the trailing edge noise prediction, which was based on a smoothed version of the high frequency analytical directivity pattern. The research was then successful in its goal of showing that trailing edge noise is significant—in this case dominant. This is confirmed by the effect of the zig-zag tape on the emitted levels, as well as later studies into the noise-reducing properties of serrated trailing edges [63], which is now standard practice for several wind turbine manufacturers.

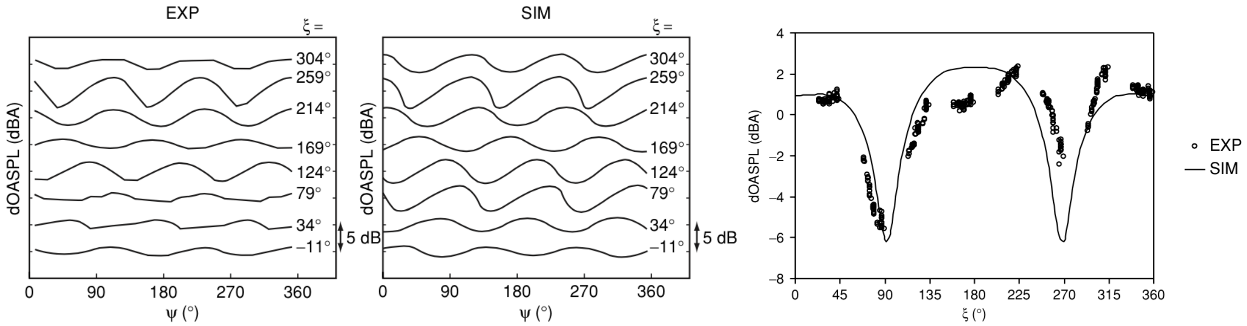

Figure 2.13: Measured and simulated (left and center, respectively) broadband amplitude modulation as a function of rotor azimuth Ψ and observer viewing azimuth ξ , and directivity of average sound levels for measurements and simulation (right). Figure credit to Oerlemans et al. [64].

2.3 Recent Wind Turbine Acoustics Research

An overview is given of wind turbine acoustics research topics that have been focused upon within the past six years. This section will serve to illustrate how the results of this dissertation fit within the framework of the state of the art in wind turbine acoustics.

2.3.1 Amplitude Modulation and Dynamic Stall Noise

Significant research has been conducted recently into amplitude modulation (AM) of wind turbine noise [64, 71, 27, 46], and specifically what has been deemed "other amplitude modulation" (OAM) [50, 61, 62]. The AM characteristic of wind turbine noise refers to the periodic variation of wind turbine aeroacoustic noise at the blade passing frequency, as illustrated in Figure 2.13, and is commonly cited as the reason for wind turbine noise being subjectively more annoying than other sources of noise at similar levels [72, 71, 46]. Under normal turbine operation, particularly within a few rotor diameters of the turbine, this is often described as the "swish" of wind turbine noise. Oerlemans et al. [65, 64] attributed this phenomenon to the directivity and convective amplification of the trailing edge noise. The "thump" noise—a related phenomenon, but far more intense—had been somewhat elusive. Several studies have since addressed this issue [61, 62, 50] and attribute the phenomenon to periodic stalling of the blade due to operation under high wind shear conditions, wind veer (wind direction variation with altitude), high yaw error, large scale turbulence, or operation in the wake of another turbine. Herein this phenomenon will be referred to as "dynamic stall noise".

Oerlemans [61] developed a prediction code for dynamic stall noise, in which the Brooks et al. [15] model was used in both attached and stalled noise prediction. The stall noise prediction code model is modified by adding 7 dB to its output in order to reflect quantitative behavior of stall noise from prior research [69, 54], i.e. a 10 dB total increase under stalled conditions. Dynamic stalling was triggered by high shear inflow profiles, and predictions matched the qualitative description of "thump" noise. Madsen et al. [50] analyze experimental unsteady surface pressure and inflow data from the DANAERO wind turbine research project. In the data, similar to the simulations of Oerlemans, dynamic stalling was triggered by a period of particularly high inflow shear. Surface pressure data show clear periodic variation, and during stall the absolute levels increase by 14 dB with energy is predominantly in the low frequency portion of the spectrum. These results are shown in Figure 2.14. Notably, the far field noise is not measured in these experiments, but could potentially be related to the unsteady surface pressure measurements [14, 54].

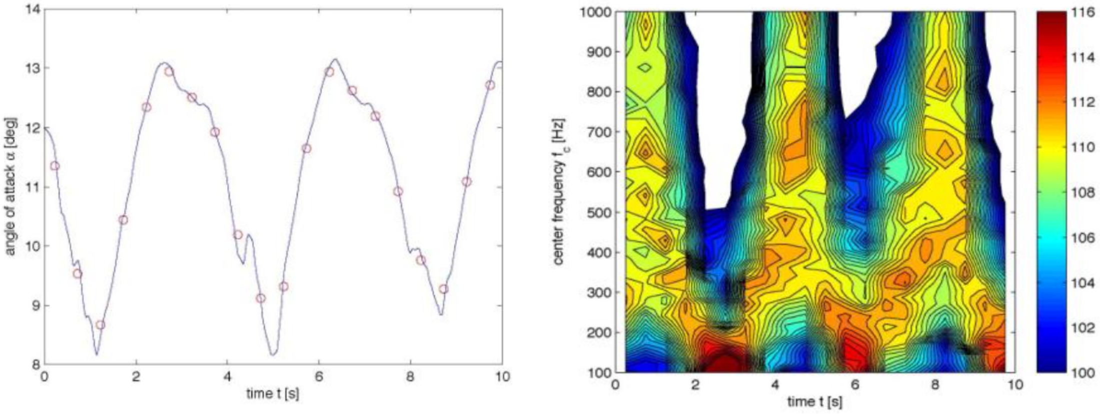

Figure 2.14: Angle of attack measured by a pitot probe at 82% span (left) and resulting surface pressure spectral variation measured by transducer close to the trailing edge (right). The color bar has units of dB re. 20 μPa. Figure credit to Madsen et al. [50].

2.3.2 Near-field Measurement of Aerodynamic Noise Sources

Another study was conducted by Bertagnolio et al. [9] using data from the DANAERO project, where surface pressure fluctuations at various chordwise locations due to boundary layer turbulence and inflow turbulence are compared to the surface predictions. Predictions are based on the TNO-Blake model for boundary layer turbulence fluctuations [11, 67] and Amiet's flat plate model for inflow turbulence [4]. The TNO-Blake model is based on a boundary layer turbulence spectral model, where boundary layer parameters such as the turbulence kinetic energy and boundary layer thickness are taken from Reynolds Averaged Navier-Stokes (RANS) simulations of the particular airfoil shapes. Bertagnolio had previously developed an improvement to the TNO-Blake method [8] that includes boundary layer turbulence anisotropy effects; the anisotropic model is used in the surface pressure study. The second prediction method is based on the surface pressure model of Amiet [3, 4] given by Equation 2.14 rather than far-field acoustic noise model. These surface fluctuations could then be used to predict the radiated noise according to the integrations methods of Curle [26], though the authors do not carry out this evaluation; as discussed before, far-field measurements were not taken during this study.

Surface pressure fluctuations near the trailing edge are compared with the TNO-Blake model [11, 67], whereas fluctuations near the leading edge are compared with the Amiet model. This choice of measurement locations is due to the fact that for non-compact sources—i.e. airfoils with chords lengths on the order of or larger than acoustic wavelengths—boundary layer surface pressure fluctuations tend to concentrate near the trailing edge, and turbulent inflow fluctuations tend to concentrate near the leading edge. The TNO-Blake predictions tend to match up within several dB with surface pressure measurements near the trailing edge, and better at frequencies above a few hundred Hz in this study. However, leading edge fluctuations induced by inflow turbulence only agree with predictions in the most basic qualitative expectations: The amplitude of the fluctuations does decrease with distance from the leading edge, but the extent to which they decrease is not reproduced. Additionally, the absolute levels and spectral shape are not reproduced, as shown in Figure 2.15. Several factors likely contribute to the disagreement here. The turbulence intensity and integral length scales are measured by a meteorological tower “a couple of 100 m” from the turbine, which means that the conditions at the turbine will be de-correlated at least to some extent from measurements. It is also noted that only one value for turbulence intensity (8%) and integral length scale (28 m) are included, though no information on the variability of these conditions is given. Additionally, it is not clear how many measurements are averaged to give these spectra, but some deviation may simply arise from non-convergence of results. Finally, as noted by the authors, for the sensor at 49% chord, it is likely that boundary layer fluctuations have begun to dominate, but are not included in these predictions.

Wind tunnel measurements were also made during this campaign using a blade section match-

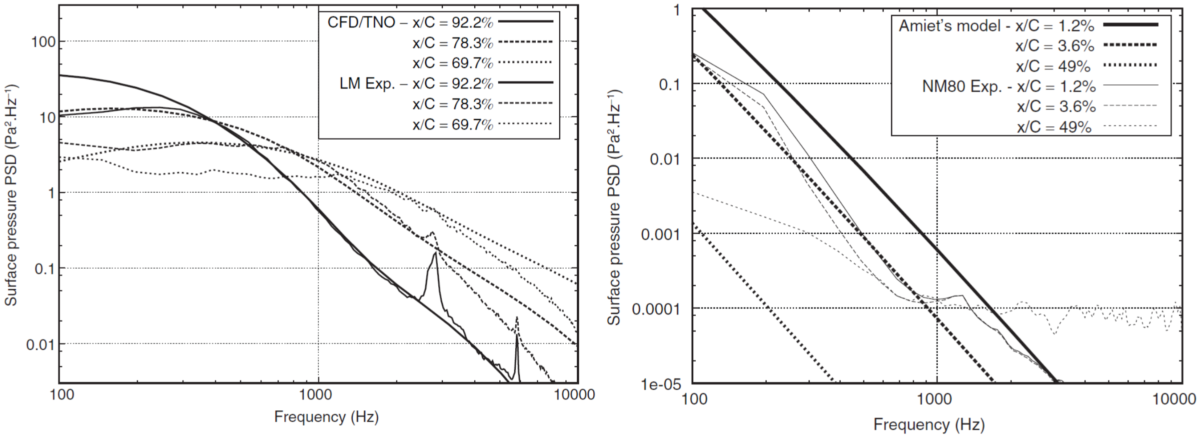

Figure 2.15: Boundary layer turbulence induced surface pressure fluctuations near the trailing edge with comparison to the TNO-Blake predictions (left), and turbulent inflow induced surface pressure fluctuations near the leading edge with comparison to Amiet predictions (right). Figure credit to Bertagnolio et al. [9].

ing the geometry of the actual turbine blade in the vicinity of these surface microphones. Inflow turbulence in the tunnel was generated using a grid in the test section upstream of the model. Turbulent inflow induced fluctuations appear to match well with predictions in the inertial subrange of the turbulence, but deviate significantly at low frequencies. The authors attribute this to a potential deviation from the nominal von Kármán spectrum used in predictions.

2.4 Related Work in General Aeroacoustics

This section offers an outline of some research that has been conducted in recent decades in the broader field of aeroacoustics that is seen as particularly relevant to this dissertation. Aeroacoustics as a research field is far more extensive than the niche field of wind turbine acoustics, so only considering the latter would be quite limiting. The research that is discussed here is broken into two categories that are particularly relevant: Research into 2D airfoil noise and research into axial fan acoustics. The former is of interest because the extension of two dimensional aeroacoustics to wind turbines is common practice, e.g. [49, 57, 65], and the latter is of interest because of the geometrical similarity between other types of axial fans, such as helicopter rotors and compressors, and wind turbines. Specific emphasis is placed on the non-dimensional characteristics—Reynolds, Mach, Strouhal, etc.—of each study and how these will relate to wind turbine noise from modern, industrial scale wind turbines.

Under normal operating conditions and for wind turbine blades with trailing edges that are thin with respect to the turbulent boundary layer—as is a common design philosophy for noise mitigation reasons [63]—the acoustic noise of modern, industrial scale wind turbines is generated predominantly by turbulent boundary layer trailing edge noise (TE noise) and turbulent inflow noise (TI noise) [49, 65]. This is because, whereas other noise mechanisms such as tip vortex noise, separation and stall noise, and mechanical noise can be mitigated by careful design, TE and TI noise are intrinsic to the relevant Reynolds numbers and operating conditions of modern designs. Stall noise is of interest in this dissertation, but background theory for this noise mechanism is discussed in Chapter 7. Thus, this section will give an outline of the analytical theory, numerical predictions, and experimental results from literature pertaining to TE noise and TI noise. The canonical works of Brooks et al. [15] and Amiet [4, 7] are discussed in Section 2.1 and are only included here for comparison.

Sections 2.1.2 and 2.1.3 give analytical expressions for how surface pressure fluctuations radiate to the far-field of an acoustic source. The Amiet model utilized this relationship between near-field fluctuations and far-field acoustic noise to develop analytical expressions for turbulent inflow noise [4] and trailing edge noise [7] from a flat plate airfoil of finite chord at a zero angle of attack. Now, while this is irrefutably a classical work within the field of aeroacoustics, these constraints are quite limiting. Wind turbines, for example, use thick airfoils at high angles of attack, making such predictions questionable if applied directly. Several approaches have been used in order to circumvent these limitations. Brooks et al. [15] created a semi-empirical model by non-dimensionalizing relationships such that their model could be nominally extended to any reasonable airfoil shape and size. The non-dimensionalization was of course not perfect, so one must take great care when making predictions for conditions that deviate significantly from the testing conditions of this work. The relationships are developed almost entirely based on measurements of

NACA0012 airfoils, for example.

A simple approach to alleviating this issue was taken by Moriarty et al. [57] in their wind turbine noise code, which was to calculate the boundary layer thickness using the airfoil solver XFoil and using this in the models of Brooks et al. [15]. This is expected to be significantly more accurate than the flat plate analytical expression used in the wind turbine noise code developed by Lowson [49] or the empirical expressions given by Brooks et al. [15] based on boundary layer measurements of the NACA0012. A more robust and physically detailed approach was developed by Parchen [67] based on the work of Blake [11], which was later adopted by Moriarty et al. [58]. The model, referred to hereafter as the TNO model (also often called the "TNO-Blake" model), uses RANS calculations of various turbulence parameters in the boundary layer, including the turbulence kinetic energy κ and integral length scale L_z for vertical velocity fluctuations, to calculate the wavenumber spectrum of the surface pressure fluctuations. Moriarty [58] notably takes an alternative approach of using the boundary layer parameters calculated by XFoil along with analytical approximations for κ and L_z in predictions. Regardless of the calculation method, the two quantities then define a von Kármán turbulence spectrum as a function of distance from the airfoil surface. The surface pressure is then calculated by the relation given by Blake [11], reproduced in Equation 2.22.

$$\Phi_p(\omega, k) = 4\rho_0^2 \int_0^\delta L_z(z) \left(\frac{\partial u_x}{\partial z} z\right)^2 \sigma_x^2(z) \Phi_{zz}(k, z) \Phi_m[\omega - u_c(y) k_x] e^{-2kz} dz \tag{2.22}$$

Here, δ is the boundary layer thickness, L_z is the vertical integral length scale, σ_2 is the root-mean-squared fluctuation velocity in the mean flow direction, u_c is the turbulence convection velocity, Φ_{zz} is the turbulence wavenumber spectrum of the vertical velocity fluctuations, and Φ_m is the so-called moving axis function that describes how the presence of the trailing edge distorts the boundary layer turbulence. The far-field acoustic spectrum is then found from the calculated surface pressure fluctuations Φ_p using the radiation theory of Howe [40]. Several modifications to the TNO model have been made since its initial development, including the anisotropic formulations of Bertagnolio et al. [8] and Kamruzzaman et al. [45], but a detailed assessment of the merits of these modifications is not relevant to this dissertation. Moriarty et al. [58] conducted a direct comparison of their implementation of the TNO model and their previous method based on the model of Brooks et al. [15], showing that the TNO model is generally as good or better than the Brooks model at matching the absolute levels, spectral shapes, and trends with angle of attack observed in wind tunnel data.

Whereas trailing edge noise is generated by interaction of boundary layer turbulence with the discontinuity of the trailing edge, turbulent inflow noise is generated by the interaction of inflow turbulence—either atmospheric or aerodynamically produced—with the leading edge of an airfoil [53]. Thus, it is important to note that under ideal conditions of flat plate airfoils at zero angle of attack, the physical mechanism for acoustic radiation is very similar between the two, and a similar mathematical approach can be taken for each as discussed in Section 2.1.4. The Amiet model [4] for leading edge noise from a flat plate, finite chord airfoil at zero angle of attack forms the foundation for the turbulent inflow noise predictions of this dissertation, along with modifications for finite thickness and angle of attack [36, 57]. Roger et al. [73] conducted an investigation in 2010 into the Amiet formulation of the leading edge noise mechanism. Comparisons were made to wind tunnel aeroacoustic measurements of a NACA0012 airfoil with 10 cm chord, a flat plate with 3% relative thickness and 10 cm chord, and a 24° cambered thin airfoil with 13 cm chord. A second thin, cambered airfoil with 13 cm chord was tested in a different wind tunnel. Turbulence intensities were 5% and integral length scales were 0.9 cm. Results from both tunnels are shown in Figure 2.16 along with predictions.

Predictions for thin bodies—the flat plate and the two cambered airfoils—match quite well to experiments. The camber is shown to have minimal effect on the noise in the left plot of Figure 2.16, but thickness has a very strong effect, reducing the noise by up to 10 dB at high frequencies. The convergence between the two shapes at low frequencies illustrates that the relevant parameter is the ratio of the turbulence scale to the thickness of the airfoil [36, 57, 73], discussed further below. Another notable feature are the spectral dips and humps of the second airfoil in the right plot of FIgure 2.16, which are reproduced quite well by the model and are noted to be due to acoustic non-compactness. Acoustic non-compactness occurs as the acoustic wavelengths of interest are on

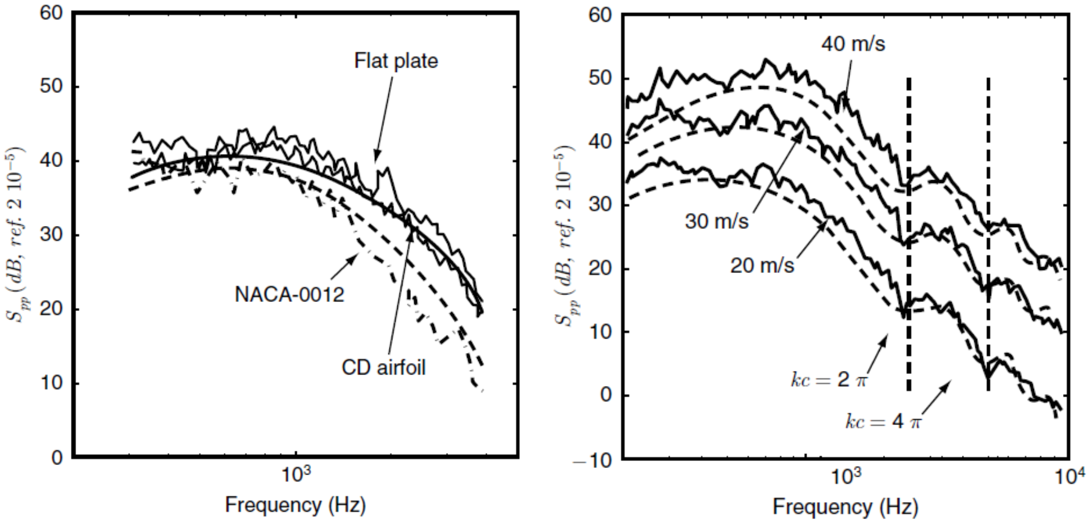

Figure 2.16: Predicted (solid smooth line; dashed line is corrected for finite airfoil thickness) and measured turbulent inflow noise at 30 m/s for a flat plate, a cambered thin airfoil, and a NACA0012 airfoil (left) and for a different cambered airfoil measured in a different tunnel at three flow speeds (right). Figure credit to Roger et al. [73].

the order of or smaller than the airfoil chord and are resultant from phase interaction of radiation from different portions of the airfoil. It is not clear from the paper why these features do not arise for the measurements *or predictions* of the other wind tunnel, given that the chord lengths are very close between all models. In any case, such non compactness effects should be noted, as they are perhaps the cause of similar features observed in the experimental data of this dissertation (e.g. Figure 6.3, right; Figure 7.7, right). The smooth dashed line in Figure 2.16 includes the corrections for finite thickness airfoils developed by Moreau et al. [55]. Moreau based his corrections on two contributing factors: The difference in radiation caused by the orientation of the surface of a finite thickness airfoil, and the distortion of turbulence by the airfoil. The former, while interesting, is shown to be a secondary effect to the latter and is based on unverified assumptions about the surface pressure fluctuation characteristics. The latter, contrarily, is modeled via rapid distortion theory [51] and is shown to be quite significant both in simulation and experimental observations, as can be seen in Figure 2.16.

Guidati [36] also developed a model for the effect of finite thickness airfoils on turbulent inflow noise. The Guidati model takes a different approach than that of Moreau et al. [55], using a potential flow solution of the undisturbed flow about the airfoil to account for the thickness, rather than using rapid distortion theory to modify the surface pressure spectrum. The fundamental governing equation is the inhomogeneous, linear, convected wave equation with the stagnation enthalpy B as the acoustic variable given below.

$$\left\{ \frac{1}{a_0} \left(\frac{\partial}{\partial t} + \vec{U} \cdot \nabla \right)^2 - \nabla^2 \right\} B = \sigma(\vec{x}, t) \equiv \nabla \cdot (\vec{\omega} \times \vec{U}) \tag{2.23}$$

Here, $\vec{U}$ is the undisturbed base flow—assumed incompressible, irrotational, isentropic, and large with respect to disturbance velocities—and $\vec{\omega}$ is the vorticity term used to account for the turbulent disturbances (not related to the angular frequency ω). The term on the far right side denoted σ defines an acoustic source. Further, a variable transformation is defined as

$$\mathcal{B} = \hat{B} e^{iMk\Phi}, \tag{2.24}$$

where $\hat{B}$ is the Fourier transform of B, M is the Mach number, and k is the wavenumber. Φ is the undisturbed velocity potential defined by $\vec{U} = U_0 \nabla \Phi$, where U_0 is the free stream inflow speed. This transformation allows the the acoustic equation to be written as the Helmholtz equation

$$k^2 \mathcal{B} + \nabla^2 \mathcal{B} = -\hat{\sigma}(\vec{x}, \omega) e^{iMk\Phi}, \tag{2.25}$$

where $\hat{\sigma}$ is the Fourier transform of the source term σ. We now have a relationship between the undisturbed flow defined by Φ, the turbulent disturbance $\vec{\omega}$, and the acoustic field B, the latter of which can readily be related to the acoustic pressure. Equation 2.25 is then transformed into an integral equation using a Green's function solution for the impulse response of the left hand side. The undisturbed potential flow Φ may be solved by, e.g. classical vortex panel methods. The integral equation is then numerically solved with the boundary condition of zero normal velocity at the surface of the airfoil.

The disturbance vorticity field $\vec{\omega}(\vec{x}, t)$ remains to be defined in order for any predictions to be made. The linearity of Equation 2.25 allows this to be done as a summation of periodic vorticity waves $\hat{\omega}(\vec{x}, \omega)$ with angular frequency ω. To derive the model, Guidati assesses the case of a point vortex that passively convect along the streamlines of the base flow. These disturbance point vortices are set in pairs of equal amplitude along parallel streamlines such that the flow perturbation velocity in the streamwise direction along the centerline is canceled. The methodology then takes advantage of the fact that a convecting point vortex is equivalent to an infinite sum of harmonic vortices in the frequency domain. Specifically, Guidati first relates the radiation pattern to Amiet's model by determining the convected vortex strength that gives the same vertical fluctuations at a given frequency as $w(x,t)$ defined in Section 2.1.4. For a flat plate airfoil in inviscid, uniform flow, the vorticity field of the point vortex is defined by Equation 2.26.

$$\omega_y(x,z,t) = \Gamma_0 \delta(x - Ut)\delta(z) \tag{2.26}$$

Here, δ is the Dirac delta function, and the same coordinate system of Figure 2.1 is used with z in the vertical direction. The Fourier transform is then given by

$$\hat{\omega}_y(x,z,\omega) = \frac{\Gamma_0}{U} e^{i\omega x_1/U} \delta(x_2). \tag{2.27}$$

This, along with the more general solution for arbitrary flow field, shows that a convecting vortex is equivalent to a harmonic vortex sheet oriented along its streamline. Note that Guidati then defines the vortex strength Γ as a function of frequency without any discussion of the implications in the time domain. This perhaps gives a more intuitive image of the vorticity distribution in the frequency domain but is not necessary for the remainder of the derivation. The vertical velocity field without an airfoil is then matched in amplitude at a single frequency to w_0 of Amiet, giving the relation

$$\Gamma_0 = i w_0 U^{|\omega\varepsilon/U|}. \tag{2.28}$$

Here, ε is half the vertical distance between the two point vortices. Thus, it is possible to use the convecting point vorticity field to assess the radiation frequency response of a finite thickness airfoil to a gust with defined vertical velocity fluctuation amplitude upstream of the airfoil. The dimension ε is tuned in experimentation but is found to have minimal effect if it is chosen to be within 1-3% of the airfoil chord. Guidati later worked with Moriarty et al. [57], modifying and tuning this vorticity distribution to include multiple vortex sheets, rather than just two.

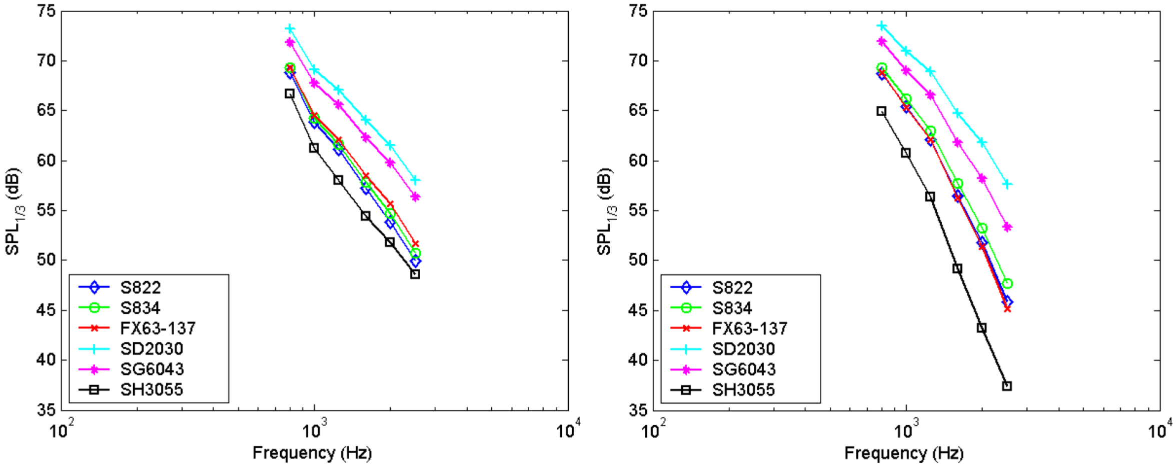

Figure 2.17: Measured (left) and predicted (right) third-octave levels for six airfoil shapes. Legends list the airfoil shapes of each measurement or prediction. Figure credit to Moriarty et al. [57].

In practice, the model is shown to accurately predict the relative effects of airfoil shape on radiated turbulent inflow noise [36, 57]. However, the absolute levels are not predicted either in Guidati's original study [36], nor in the later work of Moriarty et al. [57]. The implementation method is to rather assess the relative effects of the airfoil shape, and combine this with the absolute predictions of Amiet's model [4]. Figure 2.17 shows the predicted and measured turbulent inflow noise from a wind tunnel campaign including six airfoil shapes [57]. Measurements were made at the Netherlands National Aerospace Laboratory (NLR) using a 48-element acoustic array. Results show that the method accurately captures the effect of airfoil shape on spectral levels. The spectral shape prediction is also significantly improved above the Amiet flat plate model, for which spectra are not shown here. Moriarty et al. [58] then use a simplified model based on an interpolation of the output from this code, which greatly improves execution speed. This interpolated model is compared to experimental measurements in Chapter 6, showing significant improvement over the Amiet flat plate model. It is unclear how this method compares to the rapid distortion theory formulation of Moreau et al. [55] discussed above, but it is noted that both appear to give reasonable results in their respective studies.

Chapter 3

Experimental Facility

This chapter gives a description of the experimental setup used in this dissertation. The full scale wind turbine facility is detailed, including its available instrumentation and typical conditions. The signal processing methods used on the acquired acoustic and operational data are then outlined, including several methods of parasitic noise mitigation. Finally, an analysis of the resulting signal to noise ratio of the acoustic system is given, showing that background levels are typically more than 5 dB below measured turbine noise, even at the lowest wind speeds and frequencies analyzed.

3.1 Boulder Research Turbine

Experimentation was conducted on a full-scale, Siemens 2.3-108 prototype wind turbine at the National Wind Technology Center (NWTC) just south of Boulder, Colorado. A map showing the location of the NWTC is shown in Figure 3.2. Several notable studies have been conducted at this turbine site [22, 2] due to the available local instrumentation. The turbine rotor is 108 m in diameter and three-bladed. The tower height is 80 m. The rotor operates upwind of the tower, and the turbine is pitch regulated—both consistent with the majority of modern industrial scale turbines [20]. Trailing edges at the outboard portion of the blades are treated with DinoTail$^{\text{TM}}$ serrations for trailing edge noise reduction [63]. The turbine is highly instrumented for research purposes. Available data channels throughout this research campaign include turbine power, rotor rate, blade pitch angles, yaw angle, wind speed (cup anemometer) and direction (wind vane) measured at the back of the nacelle. Accelerometers in all three blades were shown to be useful for characterizing turbulence in the rotor plane (Chapter 4), and static pressure ports on the surface of a single blade were used in detecting aerodynamic stall (Chapter 7). These channels are all sampled at 25 Hz, except for the pressure system which is sampled at 110 Hz, though the effective bandwidth due to the physical frequency response of the system is lower. The turbine is shown in Figure 3.1.

Figure 3.1: The Siemens 2.3 MW turbine at the National Wind Technology Center. The red and white trussed tower in the left portion of the figure is the M4 meteorological tower. Photo credit to Dennis Schroeder, NREL.

The NWTC is located approximately 5 km east of the foothills of the Rocky Mountains as shown in Figure 3.2. The site is frequently subjected to strong winds out of the mountainous west—shown in Figure 3.1—owing to a drainage wind current from the Eldorado Canyon [22]. Winds out of the west are typically highly turbulent, making this an excellent site for the assessment of turbulence effects on wind turbine acoustics.

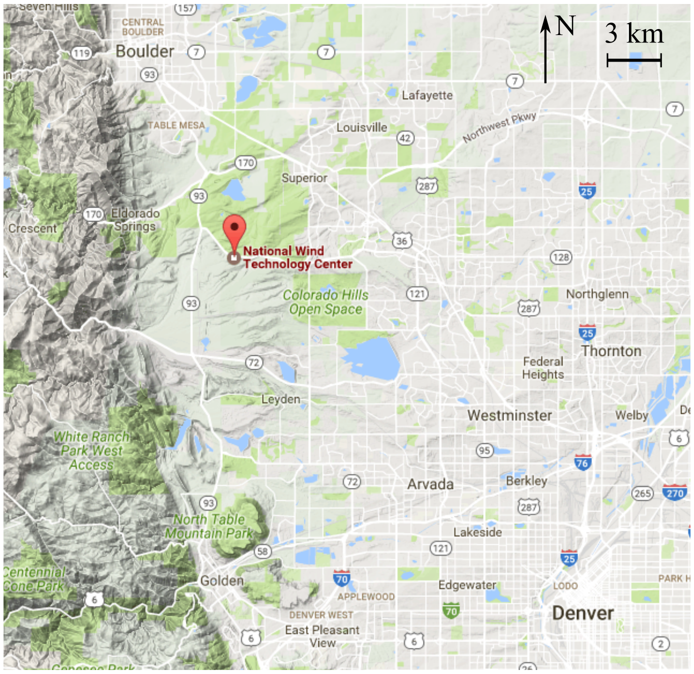

Figure 3.2: Map showing the location of the National Wind Technology Center with respect to Boulder, Denver, and the Rocky Mountains. The mountains are located in prevailing wind direction, causing turbulence levels to be relatively high—turbulence intensities typically between 10% and 30% for the present data acquisition campaign.

3.2 Meteorological Tower

In addition to the measurements systems within the Boulder turbine, a meteorological tower located 200 m west of the turbine measures wind speed, wind direction, and temperature up to approximately the maximum blade tip height. West is typically the upwind direction, so measurements at the meteorological tower usually constitute inflow measurements. Of particular interest are measurements from six Applied Technologies Inc. (ATI) three-axis ultrasonic anemometers. The ultrasonic anemometers are sampled at 20 Hz and contain no moving parts, which makes them particularly suitable for measurement of turbulence conditions. ATI specifies a wind direction accuracy of 0.1° and a velocity accuracy of 0.01 m/s. The ultrasonic signal path length is 15 cm [42]. Four of the six ultrasonic anemometers are used in this study—one was significantly below the minimum rotor height and one had technical issues—with heights of 30 m, 50 m, 76 m, and 100

m. Cup anemometer data was acquired at several heights and used mostly for verifying averaged conditions. A single three-axis ultrasonic anemometer is shown in Figure 3.3. The MET tower is shown in relation to the Siemens turbine in Figure 3.1.

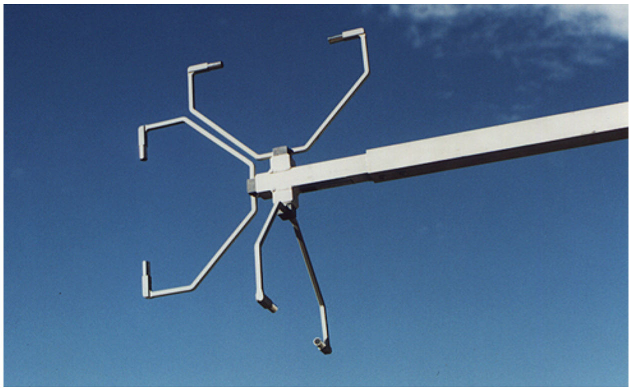

Figure 3.3: ATI 'K' Type 3-axis ultrasonic anemometer.

3.3 Acoustic Ground Ring System

Acoustic data is acquired at the Boulder turbine by twelve G.R.A.S. Type 40PH 1/4-inch diameter microphones. Factory provided frequency response curves are available for each microphone, which are flat to within 1 dB from 10 Hz up to ∼10 kHz. Further, the frequency response curves are flat to within 0.5 dB from 50 Hz to 500 Hz, which is the frequency regime shown to be dominated by turbulent inflow noise and analyzed in this paper. The microphones were calibrated several times during the testing campaign using a single-tone Brüel & Kjær Type 4231 calibration source, though due to the extensive nature of the campaign (Section 5.2) it was not possible to calibrate before each measurement. The measured channel sensitivities varied by less than 0.5 dB.

The microphones are placed on 3/4" thick circular wooden boards 1 m in diameter, for acoustic pressure doubling and thus a 6-dB increase in signal power for sufficiently high frequencies. The mounting method is in accordance with IEC Standard 61400-11. The boards are also edge treated with sand for standing wave mitigation and improved pressure doubling at low frequencies, and 66-mm diameter Brüel & Kjær hemispherical wind screens are included for wind noise reduction.

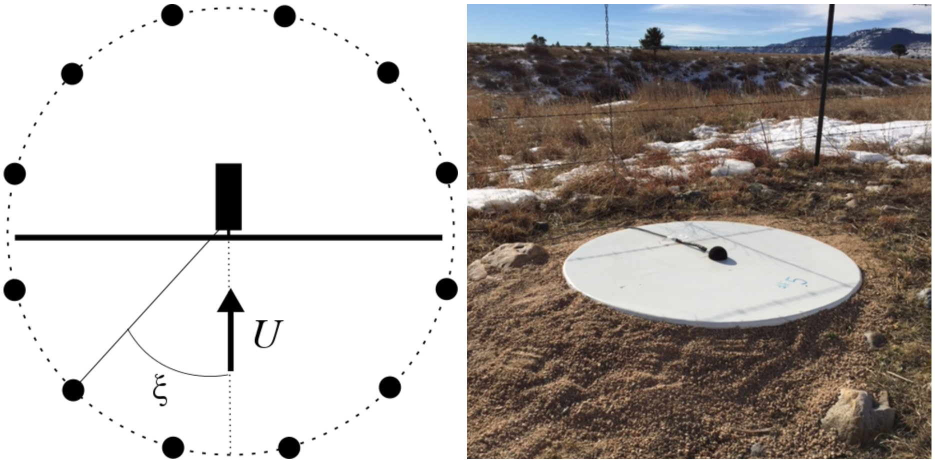

Figure 3.4: A diagram of the acoustic ground ring system (left), and one element of the ground ring system including microphone board, sand edge treatment, and windscreen (right). The angle ξ is referred to as the viewing angle for a given microphone and is measured clockwise with respect to the upwind direction.

Significant care was taken to ensure that the wind screens were dry during all testing. Microphone axes are aligned in the direction of the tower base. An example microphone is shown in Figure 3.4.

The twelve microphones are arranged equally spaced in a one-rotor radius ring about the turbine tower, as illustrated in Figure 3.4. This arrangement offers several advantages over the IEC standard position of a tower height plus rotor radius downwind of the turbine. The first advantage is that the use of this distribution of microphones allows for examination of the turbine's emission directivity regardless of the wind direction. By leveraging the theoretical directivity patterns of wind turbine noise mechanisms a clearer picture can be painted of the behavior of the acoustical system. An additional advantage of the ground ring system is that the proximity of the microphones to the turbine gives a strong signal to noise ratio, even in the presence of the other turbines at the NWTC. Section 3.6 shows that the ground ring typically achieves an energy-averaged SNR of between 8 and 10 dB for the frequencies and atmospheric conditions analyzed. It is noted that the SNR at frequencies below about 100 Hz may drop below 5 dB (Section 3.6), so significant care must be taken when drawing conclusions regarding results in this frequency regime.

Microphone signals are transmitted over ∼100 m of shielded, twisted-pair cables to a National

Instruments cDAQ-9139 integrated data acquisition (DAQ) system located in the turbine tower base. Three NI 9234 cards provide excitation current to the 12 microphones and acquire the transmitted microphone signal. A pseudo-differential acquisition configuration is used [43]. Data is sampled at either 25.6 kHz or 12.8 kHz—the latter for the purposes of stabilizing the system for extended periods of data acquisition. Anti-aliasing filters are automatically set by the DAQ system based on the sampling rate.

3.4 Signal Processing

For the analysis that follows data is processed into 15-second segments, which constitutes an average of between six and twelve blade passages at the wind speeds of interest. This segment length offers a balance between averaging over a sufficient number of blade passages and the stationarity of the atmospheric and operational conditions of the turbine within the segment. Discrete Fourier transforms are performed on block lengths of 2^{13} and 2^{14} samples for sampling rates of 12.8 kHz and 25.6 kHz, respectively, giving a frequency resolution of roughly 1.5 Hz. A Hanning window is applied to each block, and a 50% block overlap is used, so each 15-second segment spectrum represents an average of 18 spectra. The Hanning window is applied in order to prevent spectral leakage between neighboring frequencies and was shown via a convergence study to reduce the necessary bin width for convergence of calculated mean spectral levels for a 15 second data segment. The bin widths of 2^{13} and 2^{14} samples were shown to be sufficient based on this study.

Third-octave sound pressure levels are then calculated from these narrowband spectra by summing the energy within third-octave bands. Overall sound pressure levels are calculated by summing the energy from 50 Hz to 5.5 kHz. Analysis of the 25.6 kHz sampling frequency data shows that the signal energy above 5.5 kHz contributes less than 0.1 dB to the overall sound pressure level and 0.2 dB to the overall A-weighted sound pressure level. The low frequency cutoff of 50 Hz was chosen due to the high data scatter and background signal energy below this frequency. A-weighting, where applicable, is applied before energy summing. Significant care was taken to ensure that the spectra are properly calculated and normalized in order for measurements to be compared to predictions in Chapter 6. In particular, this was tested by applying the spectral method to a 94 dB single-tone calibration signal, which indeed gave the expected output of a 94 dB integrated signal power.

3.5 Electrical Noise Mitigation

Several non-negligible noise sources in acquired ground ring measurements were determined to be electrical in origin. This section describes three separate electrical noise mechanisms and how they have been mitigated in the acoustic measurement system.

3.5.1 AM Radio Interference

It was noted after some perplexing results that several of the channels of the ground ring system were picking up AM radio signals. In fact, this was determined by simply listening to the audio recordings, in which one could clearly hear sports radio, classical music, etc. Since the AM audio signal was observed to be within the frequency range of interest, was of significant strength with respect to the desired signal level, and was completely unpredictable, it had to be properly mitigated in order to trust the measurements made by the system.

After considerable troubleshooting, several features of the unwanted noise source were determined. The first was that the noise was picked up by the 100 m cables through which the microphone signals are transmitted. It was shown that the signal could be almost completely eliminated by coiling the cable into a ∼1 m diameter loop, effectively eliminating the antenna of this radio receiver. In addition, since the wires within the cables are oriented in a twisted pair configuration it was assumed that the noise is common mode in nature—i.e. common to both of the wires, rather than differential between the two—for which a pseudo-differential configuration has poor noise rejection properties [43]. Thus, the unwanted signals were mitigated using a commercially available filter solution produced by Fair-Rite Products®. The filter, referred to as a CMC (common mode choke), exploits the frequency differential between the audio signal (<13 kHz) and the AM radio signal (>500 kHz). The CMC's are placed at the DAQ end of the cables and filter the high frequency AM signal before it is converted to audio. Figure 3.5 shows that for a particular microphone, four CMC's reduced the AM signal by 15-20 dB, but five did not improve the result significantly. By similar analysis, a number of CMC's was chosen for each channel, effectively eliminating the effects of AM interference. The CMC's were also shown to have negligible effect at audio frequencies.

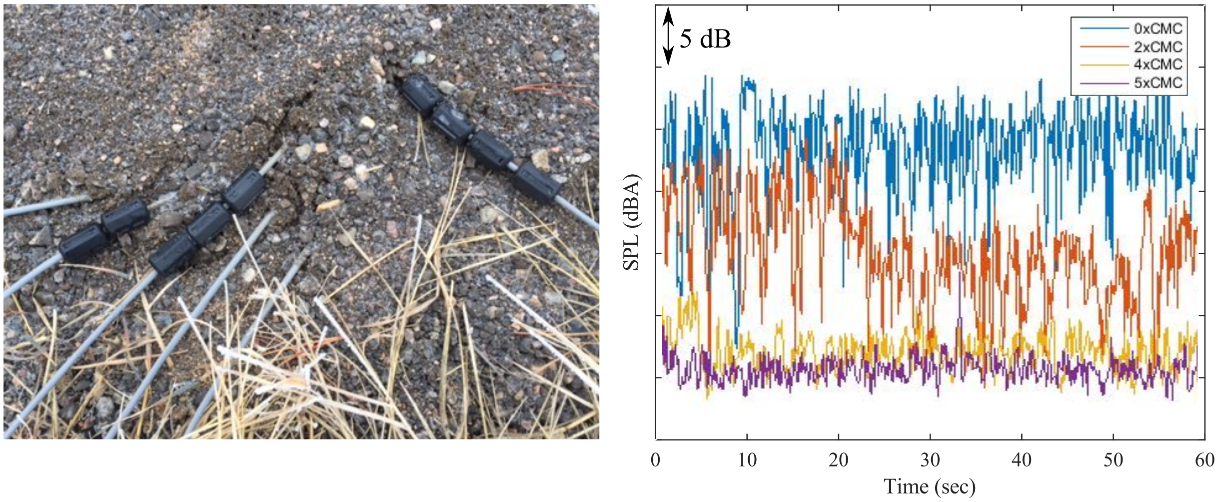

Figure 3.5: Common mode choke (CMC) devices on the ground ring cables (left) and their effect on the amount of AM signal that is picked up by the ground ring system (right). A-weighted levels in the right plot are calculated for 0.2-second data segments.

3.5.2 Broadband Electrical Noise from the Turbine

A second noise source was found in a similar way, i.e. by listening to signals that had given unexpected results. In this case, it was noted that when the turbine begins generating power the baseline level of broadband noise measured by the ground ring system increased by about 20 dB across all frequencies. The noise source is dominant when compared to the turbine's acoustic noise above about 3 to 4 kHz depending on the wind speed. Audibly, the signal sounds simply like static on an old television set and is clearly not aerodynamic in origin. The noise also does not appear to be a direct function of turbine power or RPM, for example, though it does vary in amplitude with time, again precluding the option of simply subtracting out its acoustic energy contribution.

It was determined that this source is also picked up by the microphone cables, though in this case it is transmitted through the air at audio frequencies instead of AM frequencies. This means that the CMC's have no effect on its level.

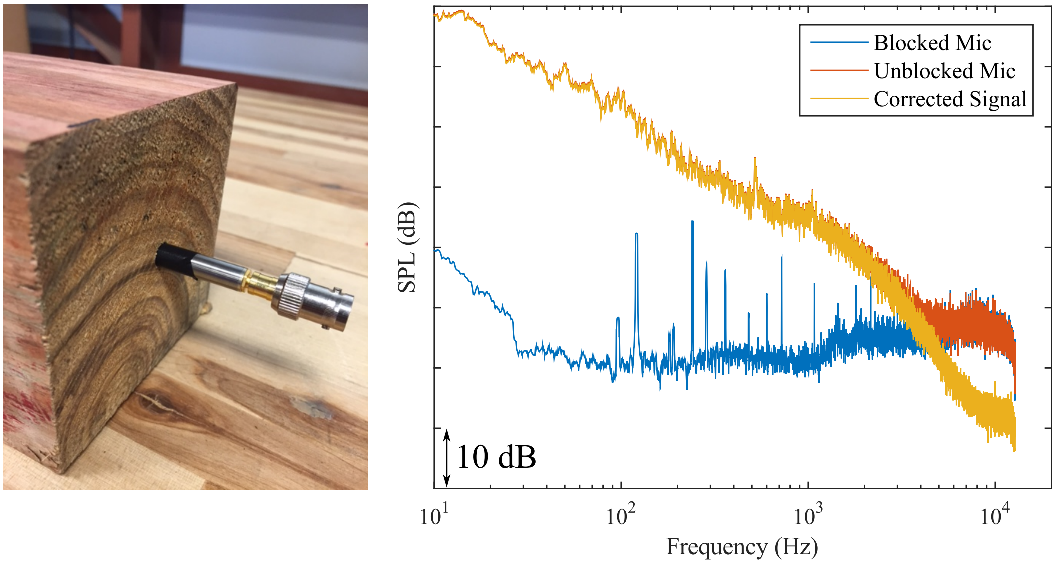

Figure 3.6: Sound-hard acoustic blocker (left) and the resulting corrected narrowband spectrum (right). Spectra shown are for 5 seconds of acoustic data with a mean wind speed of 9.5 m/s. A moving average of 15-sample width is applied to all spectra for smoothing.

A method was developed for mitigating this broadband electrical noise that actually takes advantage of the fact that the noise is transmitted at audio frequencies. The wavelengths for electromagnetic waves at audio frequencies are enormous—on the order of tens of kilometers. For this reason, the broadband electrical noise was shown to be highly coherent between channels, i.e. the electromagnetic waves arrive at each of the twelve ground ring cables in-phase. The method for mitigating the noise is then to block the acoustic signal arriving at a single microphone using a barrier that reflects the vast majority of impending acoustic energy, known as a sound-hard barrier [10]. The signal from this microphone is predominantly electrical noise, which can be subtracted from the other microphone signals *in the time domain*. Qualitatively, this method is justified by listening to the corrected signals, which audibly hold much less of this electrical noise. Quantitatively, the method is validated by examination of a signal spectrum before and after correction, as in Figure 3.6. The spectra of the corrected signal shows a significant reduction in high frequency levels. This indicates that the blocked microphone signal is dominated by the coherent, electrical noise and that subtraction is valid. Contrarily, if the signal contained incoherent noise, the spectral levels and total signal energy would increase when the signals are time-domain subtracted; measurements are rejected during processing if the signal energy increases after subtracting the blocked microphone signal. Zero-phase filtering is applied to the blocked microphone signal up to 1300 Hz for elimination of occasional low frequency wind noise penetrating the acoustic blocker. The filter is designed using Matlab's Signal Processing Toolbox and applied using the zero-phase filter function *filtfilt*, which filters the acoustic signal in the forward and reverse directions to increase stopband attenuation and negate any phase distortion; phase distortion would have been a detriment to the broadband noise subtraction method, which relies heavily on phase coherence between the two signals.

3.5.3 Tonal Electrical Noise

A final consideration was made for tonal electrical noise that became an issue at low wind speeds and low signal levels. The noise is expected to be electrical in origin both because it appears in the acoustically blocked microphone and because it typically appears at harmonics of 60 Hz grid noise. As is evident in Figure 3.6, the tonal noise apparent in the blocked microphone signal is about 10 dB below the wind turbine acoustic noise. However, as the noise scales roughly with blade tip speed to the fifth power, the acoustic signal drops significantly at reduced rotor RPM. Since the aerodynamic noise sources of interest in this dissertation—turbulent inflow noise, trailing edge noise, stall noise—are generally broadband noise sources [56], tonal noise is removed as described below. Special care is taken to ensure that this does not lead to misinterpretation of processes data. For example, deep stall noise [54] can result in tones due to large scale vortex shedding. In the stall noise analysis the signals before data processing at high angles of attack were examined showing no signs of aeroacoustic tones; no tones were present at all in fact due to the strong acoustic signal level.

The method of eliminating tones is to first define a criteria for a tone in the signals' spectra. A high order polynomial is fit to the logarithm of each spectrum. The order is chosen high enough to allow flexibility to the general broadband noise shape, while remaining numerically stable; 12th order polynomials proved to meet these criteria. A tone is then defined as a frequency for which the amplitude is abnormally larger than the fitted curve at that frequency. Figure 3.7 shows a histogram of the ratio of the measured spectra to the fitted curve. The distribution is roughly Gaussian—though not exactly Gaussian, because the ratio is a positive definite quantity—with a mean of 1.02 and a standard deviation of 0.3. A tone is then defined as a frequency where this ratio is greater than 3 standard deviations above the mean. Frequencies matching this criteria then have their respective amplitude replaced with that of the fitted curve, as shown in the right plot of Figure 3.7.

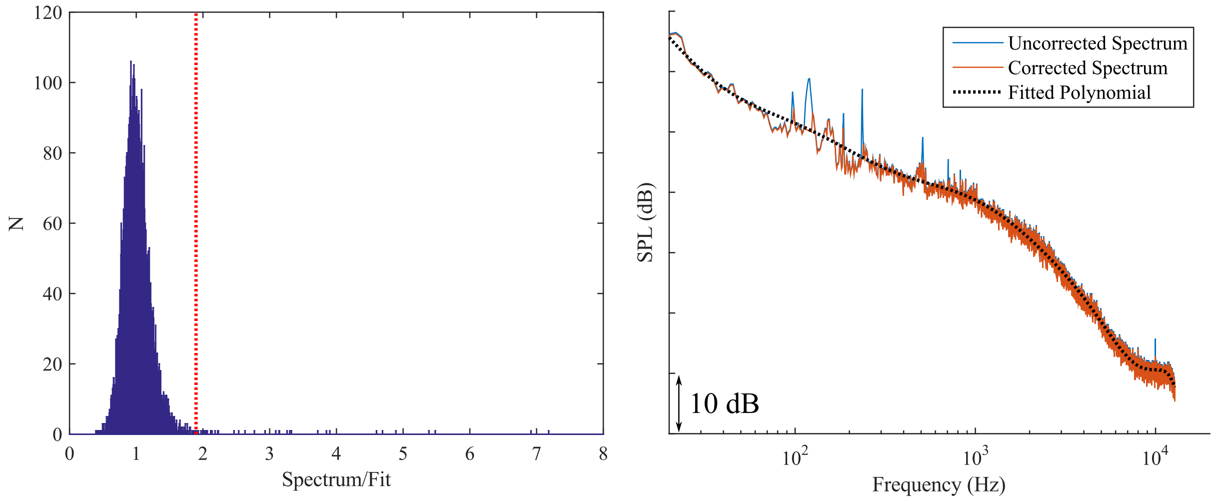

Figure 3.7: Histogram of the ratio of measured spectral levels to a fitted curve (left) and a plot showing the application of a electrical tone mitigation method based on this distribution (right). The dotted red line in the histogram represents three standard deviations from the mean. Spectra shown are for a 15-second segment and are calculated according to the methods outlined in Section 3.4. Mean wind speed is 7.5 m/s.

3.6 Signal to Noise Ratio

Background noise measurements were periodically taken during the data acquisition campaign for the purpose of determining the wind speed- and frequency-dependent relative level of background noise and correcting where necessary. To be clear, "signal to noise ratio" as it is used in this dissertation generally refers to the ratio in decibels of the total measurement level to the background noise level with the turbine off. Strictly speaking this is then a ratio of signal-plus-noise to noise, though it is approximately equal to the true SNR for SNRs on the order of 10 dB or higher.

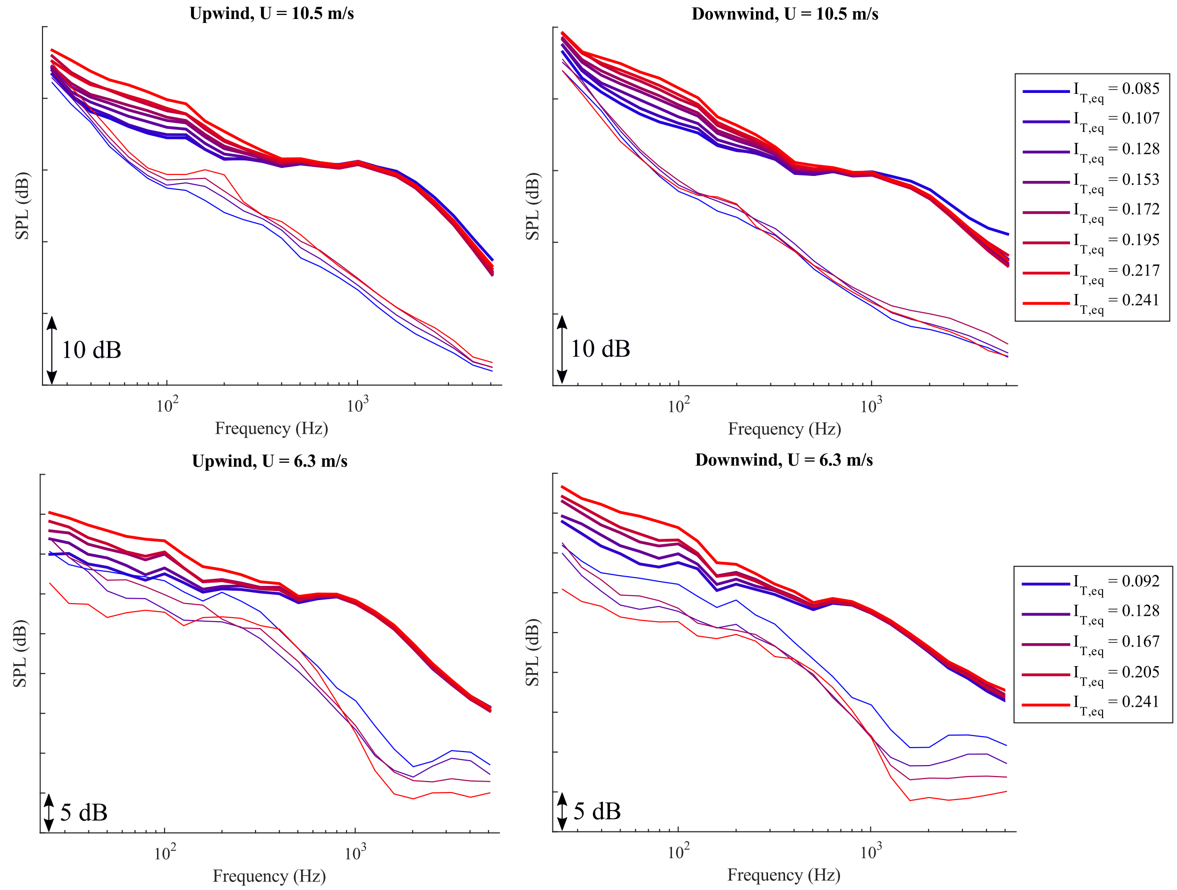

Figure 3.8: Third-octave levels with the turbine on (thick lines) and the turbine off (thin lines). Most spectra are averages of at least 10 constituent 15-second measurements, typically between 20 and 50 measurements. Equivalent turbulence intensity $I_{T,eq}$ is defined in Chaper 4.

Figure 3.8 shows the measured third-octave levels with and without the turbine on. Data is grouped by equivalent turbulence intensity (see Chapter 4) in order to show that the correlation between measured noise and turbulence—a research question of this dissertation—is not due to background noise. The relative level of the background noise is dependent on frequency, wind speed, turbulence intensity, and viewing angle about the turbine. Particular emphasis is placed on measurements made in the downwind direction at wind speeds of about 10.5 m/s in this dissertation. The top-right plot of Figure 3.8 shows that the SNR for this microphone location and wind speed is above 4 dB down to 50 Hz for the lowest turbulence levels. In the chapters that follow, 50 Hz is generally set as the low limit of analyses. Because the background levels will only have an appreciable effect at the lowest frequencies and the lowest turbulence levels considered, and because of the necessary complexity of a background correction that is frequency, wind speed, and spatially dependent, background corrections are not included for all measurements. Instead, the effect of background noise effects is considered on a case by case basis, and only corrected for when necessary, such as when considering very low frequency data or low wind speed data. The bottom plots of Figure 3.8 show that the SNR is reduced at a wind speed of 6.3 m/s, which is the lowest wind speed considered in the analysis that follows.

Chapter 4

Accelerometer-based Characterization of Turbulence

This chapter describes a method developed specifically for the study of turbulent inflow noise within this dissertation. The method uses accelerometers in each of the turbine's blades to measure turbulence-induced vibrations, from which the turbulence characteristics immediately in the vicinity of the blades can be deduced. An explanation of the motivation for the method is first given, followed by a derivation of the relationships between the accelerometer-measured blade vibrations and two turbulence parameters: the turbulence intensity and the turbulence dissipation rate. Finally, the benefit of the method is shown in the resulting reduction of data scatter.

4.1 De-correlation and Non-stationarity of Conditions

A significant research question in this dissertation is how turbulence in the inflow field to a turbine affects its acoustic emission. Fundamentally, the approach to answering this question is intuitive: Measure the atmospheric turbulence levels as well as the acoustic emission of the turbine and assess the relationship that emerges. Two factors complicate the experimental investigation. The first is intrinsic to the experimental setup described in Chapter 3. Specifically, the turbulence is measured using ultrasonic anemometers on the meteorological tower 200 m upwind of the turbine. What's more, the turbulence scales of interest in acoustics are extremely small with respect to the turbine to tower distance—acoustic frequencies above 20 Hz are generated by turbulence wavelengths of approximately 5 m and smaller. In a study on the applicability of Taylor's frozen turbulence hypothesis to the atmospheric boundary layer, Higgins et al. [38] determine from both lidar measurements of surface layer turbulence and large eddy simulation analysis that decorrelation of turbulence conditions between two points in space is highly dependent on the scale of the turbulence. Their experimental data shows the cross-correlation in wind velocity measurements taken less than 10 m apart for a length scale of 5 m is approximately 20%. This indicates that measuring the turbulence 200 m upwind of the tower and assuming that it convects downstream at the mean wind speed presents a high degree of uncertainty. Indeed, initial results from turbulence noise analyses using this basic assumption are shown in Section 4.5, and contain a level of data scatter that would preclude any insightful analysis.

The second factor takes effect only when relating noise to the *turbulence intensity*—a specific quantity that is often used to characterize turbulence in wind turbine acoustics [35, 33, 49, 31, 59] as well as in general aeroacoustics studies [4, 68, 53, 41]. The turbulence intensity is defined in Equation 4.1.

$$I_T = \frac{1}{\overline{u_1}\Delta t}\int_{t_0}^{t_0+\Delta t}\frac{1}{3}\left[u_1'^2 + u_2'^2 + u_3'^2\right]^{1/2} dt \tag{4.1}$$

Here, $\overline{u_1}$ is the mean wind for the period t_0 to $t_0 + \Delta t$, and u_i' is the velocity component in the i direction minus its mean value for that period. An issue arises particularly in wind turbine acoustics due to the large scales comprising atmospheric surface layer turbulence. Moriarty et al. [56] discuss how flow non-stationarity affected the validation process for a wind turbine noise prediction code that was developed for NREL. A particular case is shown where the wind speed increases from less than 1 m/s to 10 m/s within a 1-minute measurement segment. The time-series of the measured wind speed for this segment of data is shown in Figure 4.1, for which the turbulence intensity from Equation 4.1 is 47%. This is problematic because the TI noise prediction code in NREL's wind turbine acoustic model is fundamentally based on the Amiet model [4], which assumes a statistically stationary turbulence field. In particular, a von Kárḿan turbulence spectrum is assumed for the form of the model used by Moriarty et al. [59, 56]. This is not an issue in itself—it is shown in Section 4.3 that the turbulence spectrum at the NWTC is typically well described by a von Kármán turbulence spectrum. The issue lies in the fact that the integration time required to achieve flow stationarity in a statistical sense is very large for surface layer turbulence due to the large scale fluctuations that occur.

In their study of wind turbine inflow turbulence at the NWTC, Clifton et al. [22] use an integration time of ten minutes in accordance with IEC Standard 61400-12-1 [24]. Oncley et al. [66] discuss several previous studies for which averaging times varied from 15 to 60 minutes, and show in their own convergence study that between 5 and 30 minutes is sufficient depending on atmospheric stability conditions. Thus, the 1-minute averaging time used in the acoustic studies of Moriarty was likely insufficient for statistical convergence, meaning that the turbulence spectrum for this 1-minute period did not follow the assumed von Kármán spectrum. This is further evidenced by the fact that the noise prediction for this period was 10 dB higher than measurements (Figure 2.10). In short, the challenge is that using a long averaging time in wind turbine noise predictions is impractical because of the number of relevant operational conditions; one would have to average over not only the turbulence but also the mean wind speed, rotor RPM, and blade pitch angles,

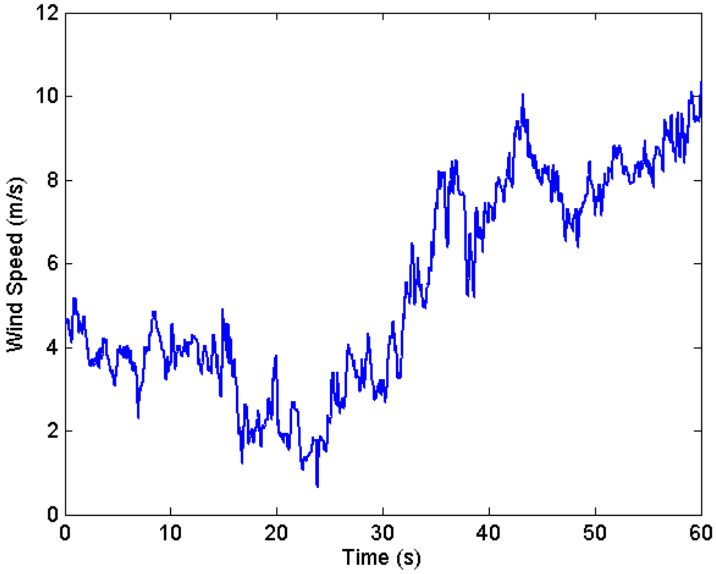

Figure 4.1: A wind speed time-series measured during the experimental campaign of Moriarty et al. [56] at the NWTC. The turbulence intensity for the period is 47%. Figure credit to Moriarty et al. [56].

making proper isolation of variables effectively impossible.

4.2 Band-limited, In-situ Turbulence Measurements

The method for solving these two problems is to use accelerometers mounted in each of the turbine's blades to characterize the turbulence directly in the plane of the rotor. Since the blades are the primary turbulence-noise generating bodies, such in-situ measurements eliminate the decorrelation uncertainty of the frozen turbulence assumption. The issue of flow non-stationarity is resolved by consideration of the fact that the large scale fluctuations in atmospheric surface layer turbulence, which contribute most of the energy to the turbulence intensity, are actually completely irrelevant in turbulent inflow noise (aside from the small effect of varying angle of attack). Again, we are generally interested in turbulence scales below about 5 m, whereas inflow turbulence energy is dominated by scales on the order of 100 to 200 m [22, 50]. This raises the question of whether it is necessary to integrate over such long period of time in order to characterize the small scale turbulence that is actually relevant in acoustics. This chapter will show that it is not. By assuming a turbulence spectral shape, the turbulence can be characterized by measuring only a finite frequency range. Further, by using only relatively high frequencies, the turbulence intensity—and later the turbulence dissipation rate—can be estimated in seconds, which significantly mitigates the issue of flow non-stationarity.

4.3 Estimation of Turbulence Intensity

Turbulence noise prediction has to this point been made based on measured or assumed turbulence intensity [35, 49, 31, 56]. For this reason, a method is first developed for estimating the turbulence intensity based on accelerometer measurements. A three-axis accelerometer is located at the 30 m radial position of each of the three blades. The signal used for turbulence measurement is aligned perpendicular to the section chord and the radial direction. This signal is used because the unsteady lift force due to turbulence is significantly higher than the unsteady drag force and therefore gives a stronger vibration signal. The pitch of the turbine blades remains nearly constant for the wind speeds analyzed in this dissertation, so consideration of changing sensor orientation does not need to be made. The accelerometer signals are sampled at 25 Hz by a separate data acquisition system from the microphone signals—a Gram & Juhl M-System. Time synchronization is accomplished by simultaneous acquisition of the same turbine signals by the two systems.

4.3.1 High-frequency Accelerometer Content

The metric used for the vibration strength is the integrated energy in the high frequency portion of the accelerometer signal spectrum. This quantity is referred to as the high frequency accelerometer content (HFAC) and is calculated according to Equation 4.2.

$$\mathrm{HFAC} = \left[\int_{f_1}^{f_2} S_{aa}(f)\mathrm{d}f\right]^{0.5} \tag{4.2}$$

Here, S_{aa} is the power spectral density of the accelerometer signal and f_1 and f_2 are the lower and upper bounds, respectively, of the frequency range of interest. For S_{aa} given in units of $(m^2/s^4)/\mathrm{Hz}$ the HFAC then has units of m/s^2 and is equivalent to the root-mean-square of the accelerometer signal if it were bandpass filtered between f_1 and f_2. The lower frequency bound was chosen as 5 Hz in order to avoid the dominant resonant modes of the blade, and the upper bound was chosen as the system's Nyquist frequency 12.5 Hz. Some losses due to the system's anti-aliasing filter may result from using the this upper bound. However, as the frequency response of the anti-aliasing circuit is linear and thus unaffected by the amplitude of the input to the system, the proportionality derived below is still expected to hold. This was verified using various upper frequency bounds.

4.3.2 Relation between HFAC and Turbulence Conditions

A scaling analysis is used to relate the HFAC to the turbulence conditions. Recall that the subscripts x, y, and z refer to velocity components in the blade frame, and 1, 2, and 3 refer to components in the stationary (anemometer) frame (Figure 2.6). The turbulence wavelength in the frame of the blade is given by Equation 4.3.

$$\lambda_T = u_{\mathrm{in}}/f = \sqrt{u_1^2 + (\Omega r)^2}/f \tag{4.3}$$

Here, u_{in} is the blade mean local inflow speed—the inflow speed incident at each radial position r along the blade due to the wind speed U and the rotor's rotational motion Ω (rad/sec)—and f is the frequency of the turbulent fluctuations at the blade surface. Axial induction, or the slowing down of the wind due to blockage by the rotor, is ignored here. Its effect would be negligibly small in this analysis because $\Omega f \gg u_1$. Given the stated frequency range of 5 to 12.5 Hz and the typical blade local inflow speed speeds of between about 30 and 50 m/s at the location of the accelerometers, the turbulent fluctuations causing these vibrations will have wavelengths on the order of 3 to 10 m (and larger further outboard). Thus, the turbulence wavelengths are typically large with respect to the blade chord lengths—less than 2 m—and a quasi-steady aerodynamic analysis is sufficient [11]. Under this assumption and the assumption of linear aerodynamics, i.e. small perturbations in angle of attack and no-flow separation, the sectional aerodynamic lift force is given by

$$L = \frac{1}{2}\rho u_{in}^2 b(c_{l,\alpha}\alpha + c_{l,0}), \tag{4.4}$$

where ρ is the air density, b is the section chord, $c_{l,\alpha}$ is the lift slope and $c_{l,0}$ is the lift coefficient at zero angle of attack. Assuming small perturbations in the perpendicular velocity component u'_z in comparison to u_{in}, perturbations in angle of attack α are given by $\alpha' \approx u'_z/u_{in}$. The perpendicular velocity component is approximately equal to the tangential perturbations in the stationary frame for small airfoil angles to the rotor plane, so $\alpha' \approx u'_1/u_{in}$. Thus, the the airfoil's unsteady lift response to a sinusoidal gust is proportional to the product of the mean inflow speed and the magnitude of the gust,

$$L'(t) \propto u_{in}^2\alpha' = u_{in}u'_1(t) \tag{4.5}$$

The vibrational acceleration $a(t)$ is predicted to be proportional to the unsteady aerodynamic force L' on the blade—i.e. neglecting blade stiffness and damping effects in the vibrational system—giving the expected proportionality below. In fact, it is shown in Section 4.4 that the blade stiffness and damping do not affect this proportionality as long as the vibrational system can be considered linear and time invariant. Thus, we have the proportionality

$$a(t) \propto u_{\text{in}}u'_1(t) \tag{4.6}$$

Here a is the acceleration of the blade section due to unsteady lift. The HFAC is related to the turbulence fluctuations through this relationship. We then have

$$\mathrm{HFAC} \propto u_{\mathrm{in}} \tilde{u_1} \tag{4.7}$$

where HFAC is the bandlimited root-mean-square of the blade acceleration from its definition in Equation 4.2, and $\tilde{u_1}$ is defined here as the bandlimited root-mean-square of the streamwise turbulence fluctuations $u_1'(t)$.

4.3.3 Relation between HFAC and Turbulence Intensity

Turbulent fluctuations within the specified frequency range $\tilde{u_1}$ now must be related to the overall incident turbulence spectrum—and specifically the turbulence intensity. The turbulence can be approximated by a von Kármán energy spectrum (Figure 4.2), given by Equation 4.8 [39, 51].

$$E(k) = \frac{Ik^4}{[1 + (k/k_e)^2]^{17/6}} \tag{4.8a}$$

$$I = \frac{55}{9\sqrt{\pi}} \frac{\Gamma(5/6)}{\Gamma(1/3)} \frac{\sigma_1^2}{k_e^5} \tag{4.8b}$$

$$k_e = \frac{\sqrt{\pi}}{L} \frac{\Gamma(5/6)}{\Gamma(1/3)} \tag{4.8c}$$

Here, $k = \sqrt{k_1^2 + k_2^2 + k_3^2}$ is the turbulence wavenumber, k_1, k_2, and k_3 are respectively the wavevector components in the wind direction, vertical direction, and cross-stream direction, Γ is the Gamma function, σ_1^2 is the overall mean-squared fluctuation velocity in the streamwise direction, L is the integral length scale of the turbulence, and k_e is the energy-containing wavelength scale of the turbulence.

In order to invoke Taylor's hypothesis and relate the wavenumber spectrum $E(k)$ to the frequency spectrum at the blade surface $S_{11}(f)$ (or equivalently $S_{zz}(f)$) it will be assumed that the inflow vector to the blade section forms a small angle with respect to the rotor plane, i.e. that the angle $\tan^{-1}(\mathrm{U}/\Omega r)$ is small. This is generally the case by virtue of the tip speed ratio of the Siemens turbine. Using Taylor's hypothesis, the longitudinal frequency spectrum $S_{11}(f)$ can be

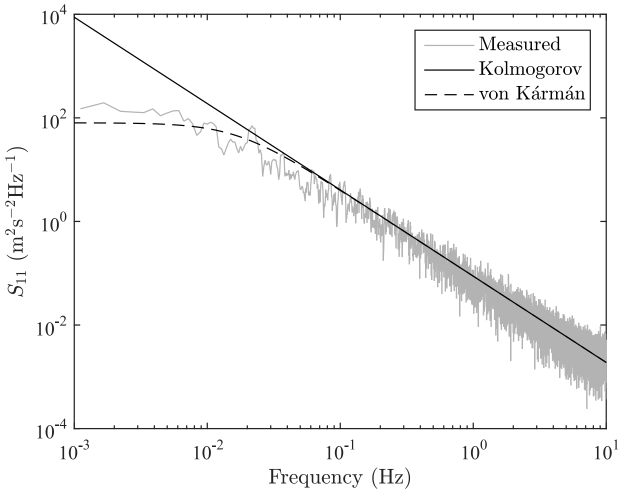

Figure 4.2: Example longitudinal turbulence power spectral density measured by the ultrasonic anemometer at hub height on the M4 tower, along with ideal Kolmogorov and von Kármán spectra. The spectrum is for thirty minutes of experimental data. A moving average of 3-sample width has been applied to the spectrum for smoothing. The mean wind speed is 11.2 m/s.

expressed by Equation 4.9 [39].

$$S_{11}(f) = \frac{2\pi}{u_{\text{in}}} E_{11}\left(k_2 = \frac{2\pi f}{u_{\text{in}}}\right). \tag{4.9}$$

Here, $E_{11}(k_2)$ is the power spectrum in the streamwise direction as a function of transverse wavenumber k_2 (or equivalently k_3). The kinematic relationship for isotropic, incompressible turbulence [39] relates $E_{11}(k_2)$ to the three-dimensional energy spectrum $E(k)$, given by Equation 4.10.

$$E_{11}(k_2) = \frac{1}{2}\int_{k_2}^{\infty} \frac{E(k)}{k}\left(1 + \frac{k_2^2}{k^2}\right) \mathrm{d}k \tag{4.10}$$

Using the von Kármán energy spectrum of Equation 4.8, this gives

$$E_{11}(k_2) = \frac{3Ik_e^4}{55} \frac{3 + 8k_2^2/k_e^2}{(1 + k_2^2/k_e^2)^{11/6}}. \tag{4.11}$$

Invoking Taylor's hypothesis, Equation 4.12 then gives the frequency spectrum in the frame of the accelerometer.

$$S_{11}(f) = \frac{2}{3} \frac{\sigma_1^2 L}{u_{\text{in}}} \frac{3 + 8f^2/f_e^2}{(1 + f^2/f_e^2)^{11/6}}. \tag{4.12a}$$

$$f_e = \frac{k_e u_{\text{in}}}{2\pi} \tag{4.12b}$$

Based on measurements of the turbulence spectra at the NWTC both during this study and in the research done at this site by Clifton et al. [22], the frequencies measured by the accelerometers are expected to be within the inertial subrange of the turbulent energy cascade. That is, the integral length scale of the atmospheric surface layer turbulence at the site is typically on the order of 100 to 200m, meaning that the ratio f/f_e is much greater than one. Thus, the high frequency asymptote of Equation 4.12 can be taken, giving

$$S_{11}(f) = \frac{16}{3}\frac{\sigma_1^2 L}{u_{\text{in}}}\left(\frac{f}{f_e}\right)^{-5/3} \tag{4.13}$$

And finally, the streamwise turbulent energy within the relevant frequency range is found by integrating Equation 4.13 as follows.

$$\tilde{u_1}^2 = \int_{f_1}^{f_2} S_{11}\mathrm{d}f = \frac{u_{\text{in}}^{2/3}\kappa}{L^{2/3}}\frac{16}{3}\left(\frac{1}{2\sqrt{\pi}}\frac{\Gamma(5/6)}{\Gamma(1/3)}\right)^{5/3}\left(f_1^{-2/3} - f_2^{-2/3}\right) \tag{4.14}$$

Here, the relation $\kappa = \frac{3}{2}\sigma_1^2$ for isotropic turbulence has been used, where κ is the turbulence kinetic energy [51]. Equation 4.14 then holds the relationship between the overall turbulence kinetic energy κ and the bandlimited turbulent fluctuations at the blade $\tilde{u_1}$,

$$\tilde{u_1}^2 \propto u_{\text{in}}^{2/3}\kappa. \tag{4.15}$$

The factor $u_{in}^{2/3}$ here is due to the effect of spatial sampling of the turbulence. Specifically, with increased inflow speed a given frequency fluctuation at the blade is generated by larger scale, higher amplitude turbulence. Figure 4.2 shows an example measured turbulence spectrum, illustrating the increased turbulence amplitude at larger scales (lower frequencies). The integral length scale of the turbulence L has been assumed constant in the scaling of Equation 4.15. This assumption is necessary because, by its nature, the measurement method will not be able to quantify the behavior at very low frequencies where this parameter has significant effect. This low frequency behavior, and thus L, have negligible effect at relevant frequencies to the acoustic analysis that follows. Its variation is therefore not generally of interest in this study.

The desired relationship between the accelerometer measured HFAC and the MET tower measured κ is now found from combining Equations 4.7 and 4.15.

$$\text{HFAC} \propto u_{\text{in}}^{4/3}\kappa^{1/2}. \tag{4.16}$$

4.3.4 Experimental Validation of Turbulence-Vibration Relation

The proportionality of Equation 4.16 was verified experimentally. Figure 4.3 shows the relationship between the measured HFAC and the quantity $u_{\text{in}}^{4/3}\kappa^{1/2}$. The mean local inflow speed u_{in} is calculated as the magnitude of the vector sum of the wind vector and rotational velocity at the location of the accelerometer. The value of HFAC is taken as the average value from the three blades. The turbulence kinetic energy κ is taken as the average value from four ultrasonic anemometers at heights between the bottom and top of the rotor, specifically 30 m, 50 m, 76 m, and 100 m. Each plotted point represents a ten-minute measurement, and thus the MET tower κ measurement captures turbulent energy down to about 1e-3 Hz. The entire data set used encompasses roughly 80 hours of data. The data is colored by the mean wind speed in order to show that the proportionality holds for a wide range of turbine operational conditions.

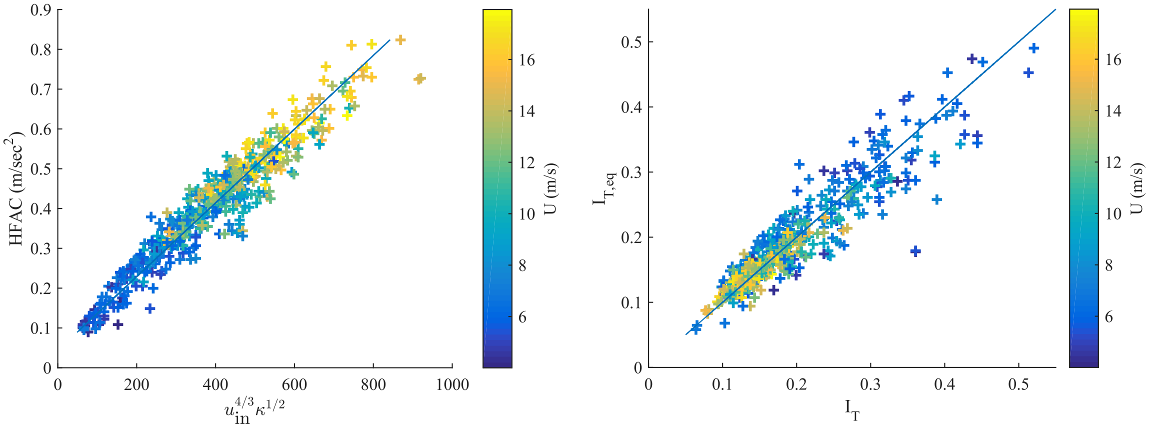

Figure 4.3: *Left*: High frequency accelerometer content (HFAC) vs. the quantity $u_{\text{in}}^{4/3}\kappa^{1/2}$, where k is the turbulence kinetic energy, along with a linear fit. *Right*: Accelerometer-mesured equivalent turbulence intensity $I_{T,eq}$ against MET tower measured turbulence intensity I_T along with an ideal one-to-one line. U is the mean wind speed. Each point represents ten-minutes of data.

The linear fit shown ($R^2 = 0.92$) may then be used to calculate the turbulence kinetic energy for a given data segment from the measured HFAC and the calculated u_{in}. In the analysis that follows, each HFAC value is mapped to a κ value from this linear relation, which is then used to calculate a turbulence intensity for each 15-second data segment. The resulting value for turbulence intensity is referred to as an "equivalent turbulence intensity" $\mathrm{I}_{\mathrm{T,eq}}$ in order to reflect the fact that it is not a formally calculated turbulence intensity, but rather a short-term estimate based on a narrowband measurement and an assumed spectral shape. The right plot of Figure 4.3 shows a comparison of accelerometer measured values of $\mathrm{I}_{\mathrm{T,eq}}$ against the MET tower measured values of I_{T}, along with the ideal one-to-one line. Each point again represents a 10-minute measurement. The plot shows a generally linear relationship with slightly increased scatter at high turbulence levels and low wind speeds. The root-mean-squared relative error, given by

$$\sigma_\varepsilon = \left[\frac{1}{N}\sum_{i=1}^{N}\left(\frac{\mathrm{I}_{\mathrm{T}} - \mathrm{I}_{\mathrm{T,eq}}}{\mathrm{I}_{\mathrm{T}}}\right)^2\right]^{0.5} \tag{4.17}$$

is equal to 0.137 for the data set shown. To give some context, an increase in turbulence intensity of 13.7% corresponds to a noise increase of 1.1 dB (see Section 2.2.3), but the scatter due to error in the model is smaller. Some of the remaining scatter in Figure 4.17 is due to de-correlation of conditions between the two measurement positions rather than the fidelity of the model, despite the 10-minute averaging time. It is difficult to isolate how much inaccuracies in the derived turbulence-vibration relationship contribute to the acoustic data scatter in Chapters 5 and 6. Given the improved experimental fidelity due to the use of this method (see Figure 4.6), the scatter of Figure 4.3 is deemed acceptable. It is also noted that due to the nature of this model development, the effect of rotor blockage on turbulence is not taken into account; this method and the acoustic analysis that follows specifically relate free-stream turbulence conditions to noise.

While I_{T} takes on the order of 10 minutes of wind speed data to calculate due to the large length scales comprising the turbulence [66, 22], the estimated value $\mathrm{I}_{\mathrm{T,eq}}$ can be calculated for periods on the order of seconds, since it is specifically comprised only of frequencies above 5 Hz. Now, this metric of course does not take into account the turbulent fluctuations outside the stated frequency range, 5 to 12.5 Hz. The use of this bandlimited measurement is justified by consideration of two facts: The first is that acoustic frequencies below 5 Hz are not of concern here, being that infrasound—acoustic fluctuations at frequencies below the human hearing threshold of about 20 Hz—is not within the scope of this investigation. The second is that the turbulent fluctuations within the stated frequency range are expected to be approximately proportional to the turbulent fluctuations at higher frequencies due to the energy cascade from large scale to small scale turbulent eddies. That is, the spectral form observed at the NWTC within the accelerometer-measured frequency regime is well described by the Kolmogorov spectrum law [39, 66], given in Equation 4.18.

$$S_{11}(f) = \alpha_1 \left(\frac{\epsilon U}{2\pi}\right)^{2/3} f^{-5/3} \tag{4.18}$$

Here, S_{11} is the power spectral density of u'_1, u'_1 is the fluctuation velocity in the mean flow direction, α_1 is the Kolmogorov constant in the mean flow direction, and ϵ is the turbulence dissipation rate. Note that this spectral form is consistent with the high frequency asymptote of the von Kármán longitudinal fluctuation spectrum for stationary point measurements, which can be derived in a similar manner to Equation 4.12. An example measured turbulence spectrum is shown in Figure 4.2 along with an overlayed $f^{-5/3}$ line and von Kármán spectrum. Now, while each 15-second measurement may not necessarily hold a converged $f^{-5/3}$ turbulence spectrum, averaging over a multitude of measurements does tend to give such a spectral shape in a mean sense. This energy cascade is expected to hold for scales larger than dissipation length scales, which should be on the order of millimeters in the atmospheric boundary layer[21], i.e. acoustic frequencies below approximately 10 kHz. Thus, higher frequency turbulence should increase in amplitude roughly in proportion to the measured turbulence, particularly when averaging over a multitude of measurements as is done in the acoustics analysis that follows.

4.4 Estimation of Turbulence Dissipation Rate

The previous section describes a method of estimating the turbulence intensity based on a band-limited accelerometer measurement, which mitigates the issues of non-stationarity and turbulence de-correlation uncertainty in the TI noise studies that follow. However, it is argued in Chapter 6 that, for the purposes of validating an acoustic prediction model, it is actually more logical to use a Kolmogorov spectrum [39] than a von Kármán spectrum to describe the turbulence. The Kolmogorov spectrum is more practical because it describes the inertial subrange of the turbulence, within which the acoustically relevant turbulent length scales reside for atmospheric surface layer turbulence. The spectrum is given in terms of a single measured quantity, the turbulence dissipation rate. This is in contrast to the von Kármán spectrum, which requires a second term, the turbulence integral length scale, to describe the generally irrelevant very large scale turbulence behavior. Thus, a similar method is developed here for estimating the turbulence dissipation rate based on bandlimited accelerometer measurements.

A slightly different approach is taken for this derivation, though the steps of Section 4.3 could be followed exactly to give the same result. Whereas in the derivation of Equation 4.16 it was assumed that the blade stiffness and damping effects were negligible, it is now shown that the stiffness and damping effects do not affect the proportionality so long as the blade vibrational system can be described as a linear, time invariant system with lift as an input and acceleration as an output. A transfer function $H(f)$ may then be defined that characterizes the blades' mass, stiffness, and damping properties.

Taking the power spectral density of the unsteady lift response of Equation 4.5 gives Equation 4.19.

$$S_{LL}(f) \propto u_{in}^2 S_{11}(f). \tag{4.19}$$

Here, S_{LL} is the power spectral density of the unsteady lift force and S_{11} is again the power spectral density of the upwash turbulence in the frame of the blade. For simplicity, Equation 4.19 is based on a 2-d unsteady lift formulation. In reality, the right hand side varies along the span of a wind turbine, making an exact expression for the total unsteady lift more involved. However, for the purposes of deriving a scaling relation between HFAC and ϵ, for which the proportionality constant may be taken from experimental data, this 2-d approximation proves to be sufficient. By definition of the transfer function $H(f)$ we then have

$$S_{aa}(f) = |H(f)|^2 S_{LL}(f) \propto |H(f)|^2 u_{in}^2 S_{11}(f) \tag{4.20}$$

Here, $S_a a$ is the power spectral density of the vibrational acceleration $a(t)$. Thus, the turbulence can be related to the measured HFAC by the combination of Equations 4.2 and 4.20.

$$\text{HFAC} \propto \left[\int_{f_1}^{f_2} |H(f)|^2 u_{in}^2 S_{11}(f) \mathrm{d}f \right]^{0.5} \tag{4.21}$$

The power spectral density of the upwash fluctuations in the blade frame S_{11} is given by the Kolmogorov spectrum law (Figure 4.2), Equation 4.22. [39, 66]

$$S_{11}(f) = \alpha_1 \left(\frac{u_{in}\epsilon}{2\pi} \right)^{2/3} f^{-5/3} \tag{4.22}$$

Here, α_1 is the Kolmogorov constant for the streamwise turbulence and ϵ is the turbulence dissipation rate. That is, upwash fluctuations in the frame of the blade are due to streamwise turbulent fluctuations in the stationary frame. Equation 4.18 assumes Taylor's hypothesis in order to translate wavenumber to frequency at the blade surface [66]. Substituting this turbulence spectral function into Equation 4.21 gives the relation

$$\text{HFAC} \propto \alpha_u^{0.5} u_{in}^{4/3} \left(\frac{\epsilon}{2\pi} \right)^{1/3} \left[\int_{f_1}^{f_2} |H(f)|^2 f^{-5/3} \mathrm{d}f \right]^{0.5}, \tag{4.23}$$

where the factors independent of frequency have been pulled out of the integral. Finally, noting that the term in brackets is effectively a turbine parameter that is nominally independent of operational conditions such as turbulence and wind speed, the final proportionality proposed is given by Equation 4.24.

$$\text{HFAC} \propto u_{in}^{4/3} \epsilon^{1/3} \tag{4.24}$$

Note the similarity to Equation 4.16, but with $\kappa^{1/2}$ replaced with $\epsilon^{1/3}$.

The proportionality of Equation 4.24 is now validated using experimental data. The same 80 hour dataset of Section 4.3 is used, and measurements are again broken into ten-minute segments in order to mitigate issues with de-correlation uncertainty. The HFAC is calculated for all three blades from the measured accelerometer data according to Equation 4.2, and the average value is taken. The turbulence dissipation rate ϵ is calculated as the mean value from the same four ultrasonic anemometers. The inertial dissipation method [66] is used based on the form of the Kolmogorov spectrum given by Equation 4.18 to solve for ϵ as in Equation 4.25, and the mean value within the inertial subrange is used. Note, that the mean wind U is used instead of the mean inflow speed u_{in}, as in Equation 4.22, because it is measured in the stationary frame rather than the blade frame.

$$\epsilon = \frac{2\pi}{U}\left[\frac{f^{5/3}S_{11}(f)}{\alpha_u}\right]^{3/2} \tag{4.25}$$

The Kolmogorov constant for longitudinal turbulent fluctuations α_u is set to 0.54 in accordance with the empirical measurements of Oncley et al. [66] and kinematically in agreement with the value of 1.65 used as the Kolmogorov constant for the three dimensional energy spectrum in the turbulence noise model in Chapter 6 [81]. The inertial subrange is taken as the region where the quantity $f^{5/3}S_{uu}(f)$ is sufficiently flat. Based on experimental observations, e.g. Figure 4.4, this region extends to very low frequencies for turbulence at the National Wind Technology center—for the case shown it appears to extend through the measured frequency range. This is consistent with measurements of previous studies showing relatively large scale turbulence at this wind site due to the mountainous topography [22]. For lower wind speed cases there does tend to be an apparent roll-off below some tenths of Hz, so the inertial subrange used for calculating ϵ is between 1 and 10 Hz.

The left plot of Figure 4.5 shows the measured values for the proportionality of Equation 4.24, along with a linear least-squares fit (R = 0.903). It is apparent that the measured relationship deviates from the proportionality for high wind speeds. With some further investigation it was determined that this is most likely due to the blade pitch angles being non-negligible at these wind speeds, which then changes the stiffness properties of the blade relative to the local inflow direction. This in turn affects the linear transfer function $H(f)$ that was assumed for Equation 4.20 and changes the proportionality. It not entirely clear why a similar effect is not observed in Figure 4.3 for I_T estimation, though it appears to be due to competing affects in the low frequency portion of the spectrum. Specifically, at high wind speeds the anemometers capture lower wavenumber components of the turbulence spectrum. This changes the spectral shape as more of the low frequency roll-off is incorporated into the κ calculation, and causes a deviation from the assumption of a constant spectral shape. Such effects could be further investigated in order to more reliably characterize the turbulence at very high wind speeds, but none of the acoustics analysis of Chapters 5 and 6 deals with such high blade pitch angles. The right plot of Figure 4.5 shows only the data within the operational conditions considered in the acoustics analysis of this dissertation. The fit has a correlation coefficient of R= 0.93, and the resulting root-mean-squared relative estimation error for $\epsilon^{1/3}$—analogous to $\mathrm{I_T}$—is 10.4%.

4.5 Fidelity Improvement Using the Accelerometer Method

In order to assess the effectiveness of the accelerometer-based measurement of turbulence, a sample acoustic analysis is performed. It is expected that the low frequency noise should be a strong function of turbulence conditions due to the dominance of TI noise at low frequencies. This is based both on existing analysis of other turbines in literature [35, 49, 56] and the noise predictions of this dissertation given in Chapter 6. Thus, the third-octave levels centered at 100 Hz are calculated and plotted as a function of turbulence conditions. The quantification of turbulence conditions will be given in terms of both turbulence intensity and turbulence dissipation rate, where either quantity is calculated first using sonic anemometer data, and second using the accelerometer methods derived in the preceding sections. Turbulence intensity is calculated from Equation 4.1, where the integration time used is 15 seconds—the same as the acoustic measurement segment length. Thus, the turbulence calculation will not include energy from very large scale and low frequency turbulence, but since this energy does not contribute to acoustic noise the resulting values of $\mathrm{I_T}$ are still expected to be a relevant metric for turbulence. Turbulence dissipation rate is calculated from Equation 4.25. Both quantities are calculated at hub-height. The third-octave sound pressure level (SPL) is calculated in the downwind direction where the turbulence noise is predicted and observed to be strongest in Chapters 5 and 6. Both plots show a significant reduction in data scatter using the accelerometer method. Scatter is reduced from 5-7 dB—on the order of the difference between maximum and minimum levels— to less than 3 dB. The remaining data scatter is resultant from numerous factors, including spatial variation of the turbulence, departure from the nominal $f^{-5/3}$ turbulence spectral roll-off, non-stationarity of conditions such as rotor rate and pitch angle, variation in acoustic propagation conditions, etc.

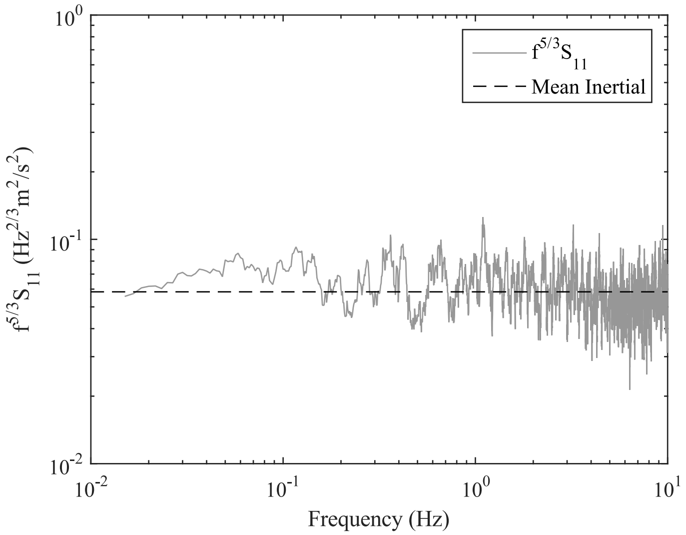

Figure 4.4: Normalized, measured spectrum for a ten-minute data segment, taken from the ultrasonic anemometer at hub height. A moving average of 20-sample width is applied to the spectrum for smoothing. Mean wind speed is 9.2 m/s, and the turbulence dissipation rate ϵ is 0.023 m^2/s^3.

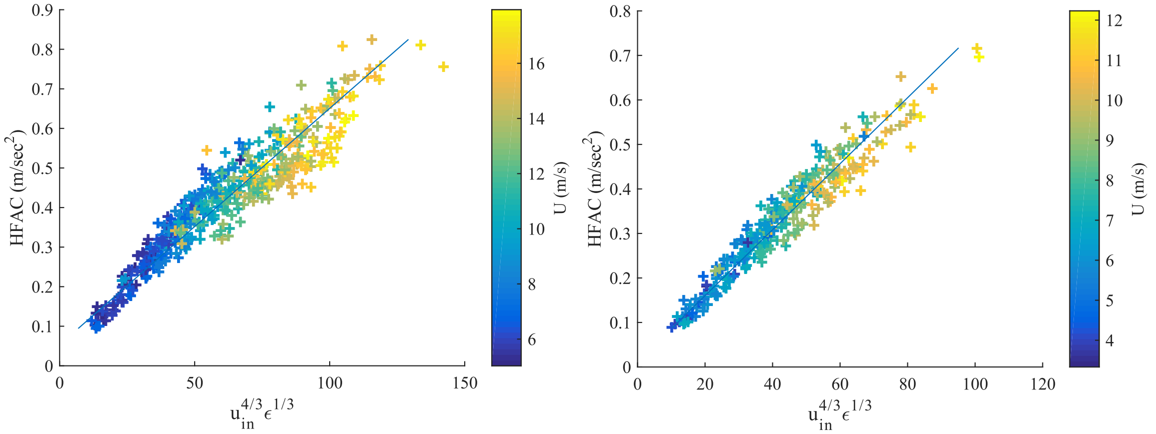

Figure 4.5: High frequency accelerometer content (HFAC) vs. the quantity $u_{\text{in}}^{4/3}\epsilon^{1/3}$, where ϵ is the turbulence dissipation rate, along with linear fits. The left plot shows all data, and the right plot is filtered to the operational conditions assessed in the acoustic analysis of Chapters 5 and 6.

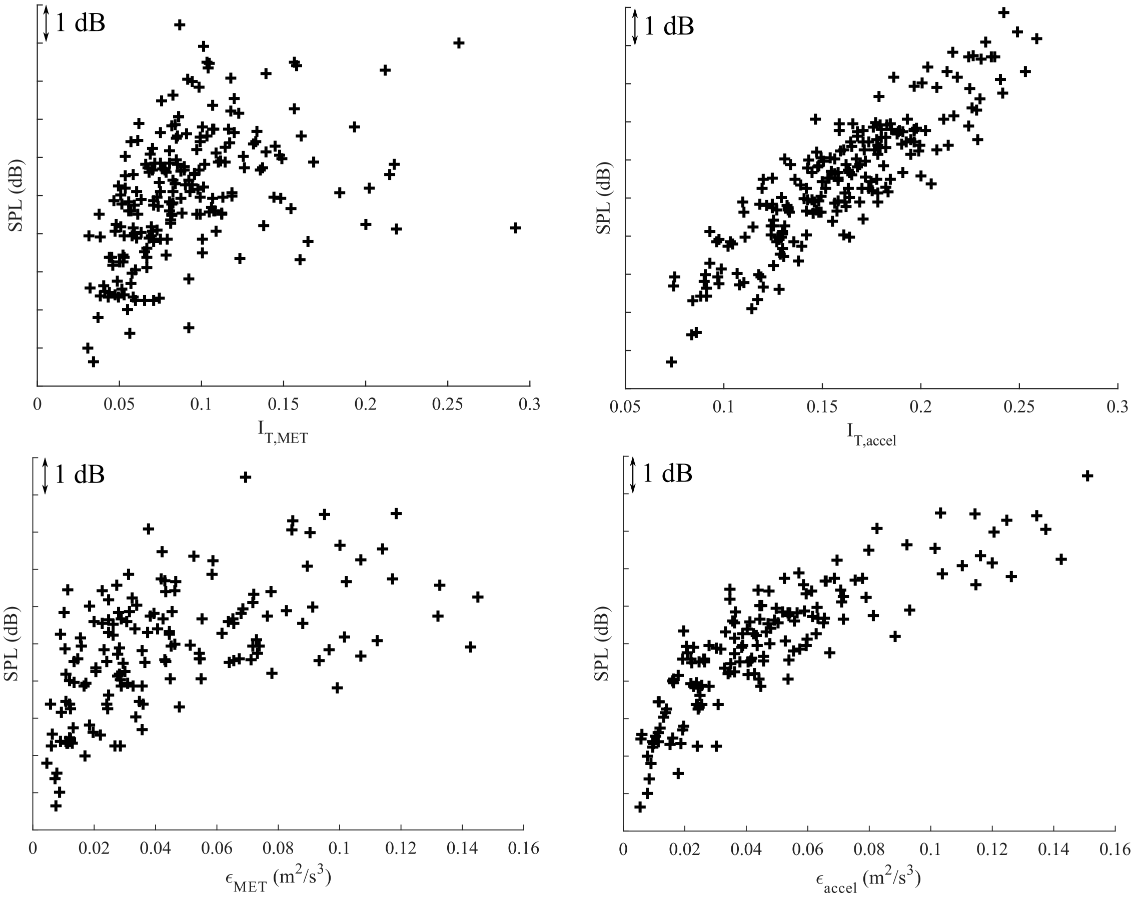

Figure 4.6: Third-octave SPL centered at 100 Hz versus turbulence intensity I_T (top) and turbulence dissipation rate ϵ, where the turbulence is measured at the meteorological tower (left) and using the blade-mounted accelerometers (right). Each point represents 15 second of data. Data taken at the meteorological tower is delayed by a period equal to the upwind distance of the tower divided by the mean wind speed.

Chapter 5

Turbulent Inflow Noise

5.1 Introduction and Background

The noise generated by modern industrial scale wind turbines is dominated by aerodynamic noise sources on the turbine blades [78, 65], each ultimately caused by some form of unsteady flow about the blade. Turbulent inflow noise (TI noise) is caused by atmospheric turbulence in the inflow field of a turbine interacting with the blades. The unsteady pressures resultant on the surface of the blades radiate according the unsteady surface pressure theory of Curle [26]. A similar phenomenon is caused by turbulence in the aerodynamic boundary layer of the blades interacting with the discontinuity of trailing edge, which is known as turbulent boundary layer trailing edge noise (TE noise). At the Reynolds numbers relevant to modern large wind turbines the aerodynamic boundary layer of a blade transitions naturally to a turbulent state, and this self-generated turbulence causes surface pressure fluctuations near the trailing edge and noise. Both of these noise mechanisms are thoroughly discussed in Chapter 2, and particularly in Section 2.4. Oerlemans et al. [65, 64] showed that TE noise dominates the mid- to high- frequency range—specifically, A-weighted overall noise levels—for a 2.3-MW turbine and a 850-kW turbine, and that the noise can be well predicted using a modified version of the semi-empirical TE noise model developed by Brooks, Pope, and Marcolini [15]. Oerlemans et al. [63] also showed that the noise source can be mitigated significantly by design of the trailing edge features.

The behavior of TI noise from wind turbines is less well established. While numerous prediction models that include TI noise have been implemented, experimental validation has been limited.

Grosveld [35] developed one of the first prediction models not based simply on empirical results. The model predicts TI noise based on a distributed dipole source approximation, and TE noise based on the model of Schlinker and Amiet [74], which was originally applied to helicopter rotor noise. Grosveld's model was validated using single-microphone measurements at various downwind and upwind positions. Notably, turbulence conditions were not measured during testing but were instead based on an assumed spectral shape scaled by a simple function of wind speed and height above the ground. The TI noise predictions were tuned to acoustic measurements. The model predicts TI noise to be stronger than TE noise for the entire measured spectrum of an upwind-rotor, two-bladed, 1-MW machine, but Lowson [49] later points out that this result was produced in error; correction of the error would lead to a more balanced noise contribution from the two mechanisms, with TI noise dominating the low frequencies and TE noise dominating at high frequencies. Lowson also developed a prediction model, which differs from Grosveld's in that it uses a frequency dependent function for TI noise based on the flat plate airfoil analytical predictions of Amiet [4]. Again, validation was carried out without direct measurement of turbulence conditions, and TI noise predictions were tuned to single-microphone measurements.

Moriarty et al. [59, 57] developed the acoustic prediction code for the National Renewable Energy Laboratory's (NREL) wind turbine computer-aided engineering tool FAST. The model includes a TI noise model based on Amiet's model combined with the modifications for finite thickness airfoils and angle of attack developed by Guidati et al. [36]. Turbulence conditions were measured during model validation using ultrasonic anemometers located on a meteorological tower upwind of the turbine. Agreement between predictions and observations are variable within this body of work. In particular, Moriarty notes a case where the non-stationarity of flow conditions—i.e. strong wind gusts—cause an unreasonably large prediction of TI noise. The wind speeds from this one-minute measurement varied rapidly between 2 m/s to around 10 m/s resulting in a calculated turbulence intensity value of 46%, which is then fed to the noise prediction code. The issue is that the gusts contributing to this turbulence intensity value comprise frequencies much lower than those of interest to acoustics—periods are on the order of a minute. This issue of non-stationarity is addressed in the analysis that follows. In general, it does not appear that enough data was gathered by Moriarty to confidently determine the accuracy of the TI prediction model or to correlate measured low frequency noise to inflow turbulence conditions.

The work presented in this chapter is intended to build upon prior research by definitively characterizing the effect of turbulence in the turbine inflow field on its acoustic emission. A large volume of experimental data is analyzed, for which both the atmospheric conditions and acoustic emission of the turbine are thoroughly captured. Turbulence is measured using the blade accelerometers, as detailed in Chapter 4. The method allows for assessment of turbulence conditions directly in the rotor plane, and also alleviates the issue of inflow non-stationarity [56] by measurement of only relatively small scale turbulence. A consistent relationship is observed between turbulence conditions and noise, particularly at low frequencies, constituting perhaps the most thorough experimental analysis of the effect of turbulence levels on wind turbine noise to date. Finally, several possible mechanisms for the observed behavior are discussed in order to further clarify its nature and cause, showing by far the most consistency with the expected behavior of TI noise.

5.2 Measurement Campaign

The measurement campaign for assessing the effects of turbulence on wind turbine noise constituted the most significant portion of the total experimental effort of this dissertation. Testing was conducted between December of 2014 and early February of 2015 resulting in over 150 hours of continuous acoustic data. Microphones were calibrated several times during this testing period. The extent of the testing campaign made calibration before every measurement prohibitively difficult, although the measured channel sensitivities showed a variation of less than 0.5 dB during the period. This is significantly less than the observed data scatter. Particular care was taken to ensure that the wind screens were completely dry before use to mitigate insertion loss variability, and that snow was cleared from within a meter of the ground boards. Most measurements were made with little or no snow on the ground surrounding the turbine. Due to the close proximity of the microphones to the predominant noise source—the turbine—snow would have minimal effect on measurements insofar as the change in propagation effects and would only likely serve to reduce background noise.

Several modifications were made to the system through the end of December, including the development and implementation of the electrical noise mitigation techniques discussed in Section 3.5 and the addition of 66 mm wind screens to replace the original 30 mm wind screens for improved wind-induced-noise mitigation at low frequencies. The final configuration was in place by early January. The analysis that follows is based only on the data acquired using this final configuration, as it is known to be of the highest quality. Removing the early data and taking only the data where the wind was high enough for the turbine to generate power leaves roughly fifty hours of continuous data. The dataset is reduced further by selecting measurements for which the mean wind direction is within 30° of the predominant wind direction (and meteorological tower direction), reducing the amount of data used to 34.4 hours, which is broken into 8,600 15-second segments (Section 5.3). This filter is applied because the inflow direction has been observed to have a significant effect on observed noise levels, particularly in the directions of local topographical recesses to the south and east of the turbine. While such inflow effects may be of interest for future work, the turbulent flow from these topographical features is not likely fully developed at the location of the turbine, making its characteristics less predictable. As such, these effects will not be assessed in the analysis that follows.

Figure 5.1 shows a histogram of the testing conditions during the experimental campaign. The colors represent the number of measurements taken at each specified wind speed and equivalent turbulence intensity—i.e. the turbulence measured with the blade accelerometers. Wind speeds reached well above 16 m/s. However, the acoustic signal to noise ratio was too low to be used reliably in analysis for wind speeds above about 14 m/s, and the analysis that follows only involves wind speeds up to 11.5 m/s. Equivalent turbulence intensities covered a range between about 0.1 and 0.3.

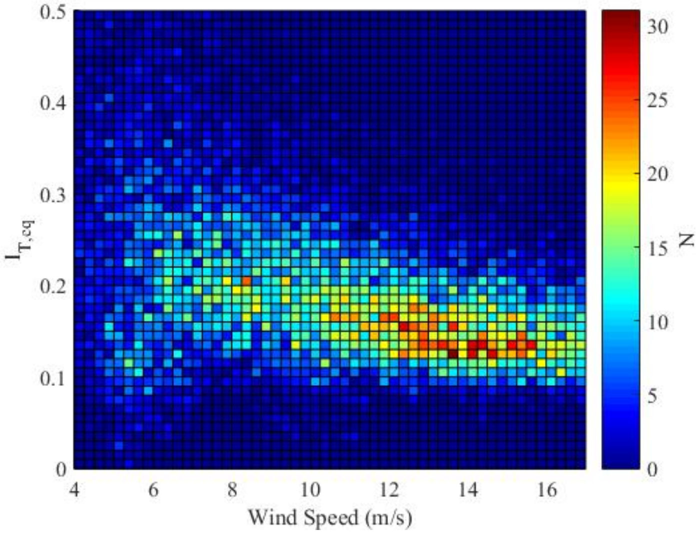

Figure 5.1: Histogram of testing conditions during the turbulent inflow noise data acquisition campaign. N is the number of 15-second measurements matching the respective wind speed and equivalent turbulence intensity.

5.3 Data Processing

The large volume of data collected for this particular study required an efficient processing method in order to facilitate reasonably fast analysis—the unprocessed acoustic dataset alone contains 70 GB of audio files. The data is processed in 15-second segments, which constitutes an average of between six and twelve blade passages at the wind speeds of interest. This segment length offers a balance between averaging over a sufficient number of blade passages to mitigate amplitude modulation effects and maintaining a reasonable level of stationarity of atmospheric and operational conditions within the segment. Averages and standard deviations are taken over the 15-second segment for relevant operational conditions such as wind speed and direction at various heights, turbine power, blade pitch, rotor RPM, turbine yaw angle, and high frequency accelerometer content (HFAC). For the acoustic data, discrete Fourier transforms are performed on block lengths of 2^{13} and 2^{14} samples for sampling rates of 12.8 kHz and 25.6 kHz, respectively, giving a frequency resolution of roughly 1.5 Hz. A Hanning window is applied to each block to reduce spectral leakage between frequency bins. A 50% block overlap is used, so each 15-second segment spectrum represents an average of 18 spectra. The electrical noise mitigation methods described in Section 3.5 are implemented. The data processing reduced the data from 70 GB to only 8 GB.

In post-processing, third-octave sound pressure levels are calculated from the narrowband spectra by summing the energy within third-octave bands. Overall sound pressure levels are calculated by summing the energy from 50 Hz to 5.5 kHz. Analysis of the 25.6 kHz sampling frequency data shows that the signal energy above 5.5 kHz contributes less than 0.1 dB to the overall sound pressure level and 0.2 dB to the overall A-weighted sound pressure level. The low frequency cutoff of 50 Hz was chosen due to the high data scatter and background signal energy below this frequency. A-weighting, where applicable, is applied before energy summing.

5.4 Results

This section details the results of the experimental campaign. Several experimental observations are presented for a range of turbulence conditions, including the directivity of measured noise, overall sound pressure levels, and third octave spectral levels.

5.4.1 Turbine Noise Directivity

Wind turbine noise directivity is first examined in order to leverage information captured by the full acoustic ground ring system and to determine the directionality of emitted turbine noise. Note that the term “directivity” by itself will refer to the noise directivity about the turbine—sound pressure level (SPL) as a function of viewing angle ξ (see Figure 3.4). “Airfoil directivity” will be used to distinguish the 2-d directivity about an airfoil section. Figure 5.2 shows the measured unweighted and A-weighted directivity patterns for wind speeds between 9 and 11.5 m/s. Wind speed is measured at the meteorological tower at hub height. Data is colored by equivalent turbulence intensity, and each point represents a 15-second measurement. Data is filtered such that the 15-second mean rotor RPM is within 4% of the mean value for the wind speed bin, and pitch is within 1° of the mean value for the wind speed bin. The small remaining variation in rotor rate is compensated for by normalizing the sound levels to the mean rotor RPM, assuming a $p^2 \sim v_{in}^6$

scaling, where p is the acoustic pressure. This reflects the theoretical scaling of low frequency turbulence noise [35, 49], and differs by less than 0.2 dB from the v_{in}^5 scaling of high frequency edge noise [15, 4] for this range of rotor RPM. Two extraneous measurements with unusually high equivalent turbulence intensities have been removed to improve the clarity of the figure, representing less than 1% of the included measurements; it is unclear whether the two outliers were due to electrical artifacts or actual high intensity vibrations. Data from this wind speed bin was selected for presentation because of the large number of data points meeting the filtering criterion. The presented results are generally representative of observations across the operational range of the turbine, and any deviations at other wind speeds are noted.

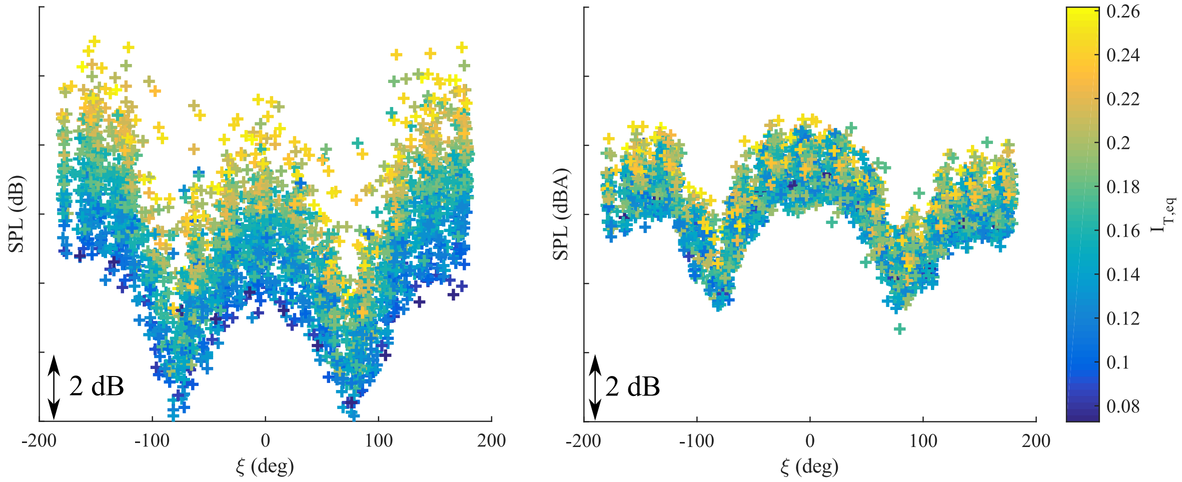

Figure 5.2: Unweighted (left) and A-weighted (right) overall sound pressure levels as a function of microphone viewing angle ξ. Data is colored by accelerometer-measured equivalent turbulence intensity. Each data point represents a 15-second measurement. Wind speeds are between 9.0 and 11.5 m/s.

Several features of the measured directivity patterns are notable. Both the unweighted and A-weighted levels are significantly reduced in the plane of the rotor—at $\xi = \pm 90°$—which has been previously observed in experimental measurements [65] and simulation data [31, 59, 64]. It is shown in Section 5.5 that this feature—referred to hereafter as the “noise dips”—is consistent with the formulation of Brooks and Burley [13] of the theoretical airfoil directivity patterns of

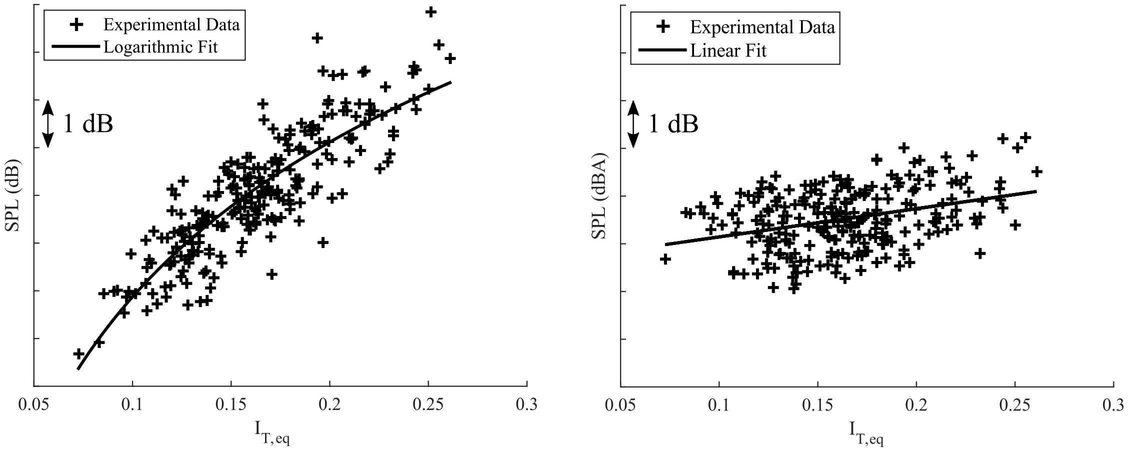

Figure 5.3: Unweighted (left) and A-weighted (right) overall sound pressure levels in the downwind direction as a function of equivalent turbulence intensity $I_{T,eq}$. Each data point represents a 15-second measurement. Wind speeds are between 9.0 and 11.5 m/s. Note that y-axes have different absolute scales.

turbulent boundary layer trailing edge noise as well as turbulent inflow noise, which have nulls in the plane of the blade. The second feature to take note of is the correlation between sound levels and turbulence conditions. The left plot of Figure 5.2, the measured directivity pattern, shows a consistent gradient in sound levels between the lowest and highest turbulence levels, particularly in the upwind and downwind directions. The left plot of Figure 5.3 illustrates the trend specifically in the downwind direction, where TI noise is both predicted and observed to be strongest (see Section 5.5). The included logarithmic fit is discussed further in Section 5.4.2.

The right plots of Figures 5.2 and 5.3 show A-weighted levels, which reflect the frequency dependence of human hearing and de-emphasize low frequencies. Only slight positive correlation to equivalent turbulence intensity is observed, illustrated by a linear fit included in the right plot of Figure 5.3 to assess this basic trend. The growth in A-weighted levels is between 0.5 and 1 dB across the range of turbulence intensities observed for all wind speed bins analyzed, which is less than the magnitude of the data scatter. However, the consistency of this positive correlation across all wind speed bins analyzed supports the claim that A-weighted levels are at least affected by turbulence conditions.

5.4.2 Scaling with Turbulence Intensity

The scaling of measured noise levels with turbulence intensity, as seen in Figure 5.3, is examined by fitting curves to the experimental data. Turbulent inflow noise is expected to scale according to $p^2 \sim \mathrm{I}_\mathrm{T}^2$ [4, 35, 49] (see Section 2.2.3), which means that a 6 dB increase in turbulent inflow noise is expected for a doubling of turbulence intensity I_T. This can be expressed mathematically by Equation 5.1, where A is equal to 6 and B is a constant.

$$\mathrm{SPL}_{TI} = A \log_2 \mathrm{I}_\mathrm{T} + B. \tag{5.1}$$

In order to check this relation, a logarithmic least squares fit following the form of Equation 5.1 is made to the experimental data of Figure 5.3, where the coefficients A and B are left as fit parameters. The downwind direction is used because the strongest turbulent inflow noise is both observed and expected here. The effect of background noise is accounted for by subtracting the mean background levels (Figure 3.8) on an acoustic pressure squared basis. The fitted parameter A represents the measured growth in SPL for a doubling of equivalent turbulence intensity. The fitted logarithm for unweighted levels is shown in Figure 5.3 (left) along with the measured levels in the downwind direction. The logarithm shows a growth of 3.7 dB per doubling of equivalent turbulence intensity. The mean value across all operational bins analyzed—between 6.5 and 13.5 m/s—was 3.6 dB, with little correlation to wind speed or rotor rate observed. This suggests that the noise contribution from turbulent boundary layer TE noise is likely on the order of the contribution from TI noise, reducing the effect on overall levels of TI noise.

Performing the same analysis on only the spectral energy in the third-octave band centered at 80 Hz yielded a growth of 4.8 dB per doubling of equivalent turbulence intensity, which is still less than the theoretical 6 dB for pure turbulent inflow noise. It is not likely that this can be attributed to the presence of TE noise due to the small expected contribution of TE noise at low frequencies based both on previous research [49, 56] and the noise predictions of this study shown in Chapter 6. Several other potential reasons for this deviation from theory have been examined. The turbulence measurement method was first scrutinized by examining how well the linear relationship established in Chapter 4 between turbulence and blade vibration holds for the particular operational conditions present for the data of Figure 5.1. Specifically, the data shown is for a very narrow rotor RPM window, and thus u_{in} window, meaning that one must examine the scaling relationship HFAC $\propto \kappa^{1/2}$ within this particular range of u_{in}. Indeed, the relationship does hold quite well, and the RMS estimation error given by Equation 4.17 is 8.8% for these operational conditions—better than the overall estimation error. Consideration has also been made of the fact that the theoretical scaling law is based on a perfectly rigid airfoil, whereas the aero-structural-acoustic system of the turbine is significantly more complex. If the vibrational velocity of the blade is significant with respect to the incoming turbulence fluctuations this could certainly affect the emitted noise. However, the vibration velocity of the blade—at least at the location of the accelerometers—has been observed to be quite small in comparison to the turbulent velocity fluctuations, by a factor of about 30. This factor was also observed to be independent of turbulence intensity, indicating an approximately linear system where any effect on noise can be expected to be independent of the amplitude of the turbulence. Such *linear* effects are unlikely to significantly affect the observed scaling. Instead, it is expected that the cause of this deviation from theory must be nonlinear in that it does not reduce the noise by a constant decibel value—it either increases the noise at low turbulence levels or decreases the noise at high turbulence levels. A turbine noise source at low frequencies (e.g. stall noise) could explain the former, for example, as such a source would not be detected in the background noise measurements.

5.4.3 Third-octave Spectra

Figure 5.4 shows the third octave spectral levels measured within 15° of the downwind position. Spectra are grouped by equivalent turbulence intensity and averages are calculated on an acoustic pressure squared basis. The lowest and highest turbulence intensity bins of Figure 5.4 are averages of two and three measurements' spectra, respectively. All others are averages of at least 13 constituent measurements. The resulting spectra show a clear positive correlation with equivalent turbulence intensity, particularly in the low frequency portion of the spectrum. A signal to noise ratio analysis was conducted in order to verify that this correlation was not simply due to low frequency wind induced noise on the microphone diaphragms, i.e. due to an increase in hydrodynamic pressure fluctuations at higher turbulence levels. This analysis is presented in Section 3.6 and does indicate that this low frequency correlation is not due to wind noise.

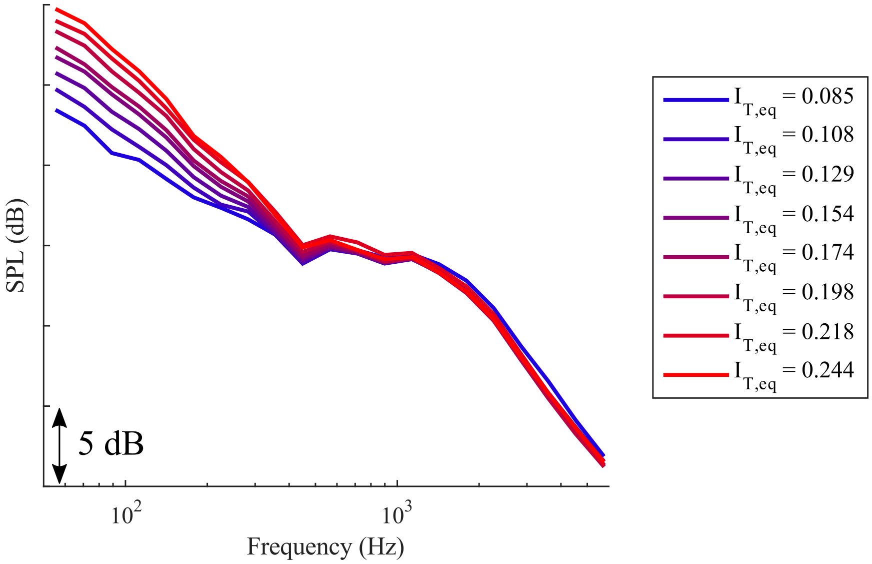

Figure 5.4: Third octave spectra for varying turbulence conditions, measured in the downwind direction. Each spectra shown is an average of at least 13 constituent 15-second measurements. Wind speeds are between 9.0 and 11.5 m/s. Note that spectra are not A-weighted.

Spectral levels above 600 Hz converge to within 0.7 dB. This result is consistent with the theoretical expectation that TI noise be dominant at low frequencies and TE noise be dominant at high frequencies [35, 49, 59]. That is, the relative consistency of levels above 600 Hz is characteristic of TE noise, which is expected to be nearly independent of inflow turbulence conditions—the minor effects of fluctuating angle of attack on trailing edge noise are discussed in Section 5.6.

5.4.4 Atmospheric Attenuation Effects

A-weighted noise levels reflect the frequency dependence of human perception and are therefore used in most noise regulations. As noted above, the measured, A-weighted levels at the ground ring are only minimally affected by the varying level of turbulent inflow noise. However, the low frequency nature of the turbulent inflow noise means that it will propagate more efficiently than higher frequency turbulent boundary layer trailing edge noise, and will therefore have more influence at large distances from the turbine.

Using the atmospheric attenuation model specified in ANSI S1.26-1995 and ISO 9613-1:1993 [10], and assuming; a temperature of 20°C, a barometric pressure of 1 atm, and a relative humidity of 50%, the frequency dependent attenuation of Figure 5.5 is calculated; these conditions are chosen for illustrative purposes only, but the low-pass filtering effect shown is present regardless of atmospheric conditions. Figure 5.6 shows the expected effects of this attenuation on A-weighted spectral levels. The left plot shows A-weighted third octave spectra measured at the ground ring in the downwind microphone position. The right plot shows the same spectra reduced by the atmospheric attenuation expected at a distance of 500 m. The difference in overall A-weighted levels between the minimum and maximum turbulence conditions is 0.5 dB, whereas at a distance of 500 m the projected difference is 1.8 dB. This result notably does not account for directivity effects, i.e. the difference in elevation angle between the ground ring and the theoretical 500 m observer point. Such effects need to be investigated. However, it is expected that these trends will be at least approximately representative of the true effects of atmospheric attenuation.

5.5 Comparison to Expected Behavior

The effect of turbulence conditions on noise has been presented in Sections 5.4.1 through 5.4.3, but the exact noise mechanism has not yet been considered. That is, the correlation could be due to induced pressure fluctuations on the blade due directly to the turbulence, referred to as TI noise; it could be due to variations in boundary layer thickness and TE noise levels; or it could be due to periodic stalling—and thus stall noise—due to extreme turbulence induced angle of attack variations. This section shows comparisons between the measured directivity pattern at various frequencies and theoretical directivity patterns for TI noise and TE noise. The noise directivity at low frequencies is consistent with TI noise. It is also shown that the directivity

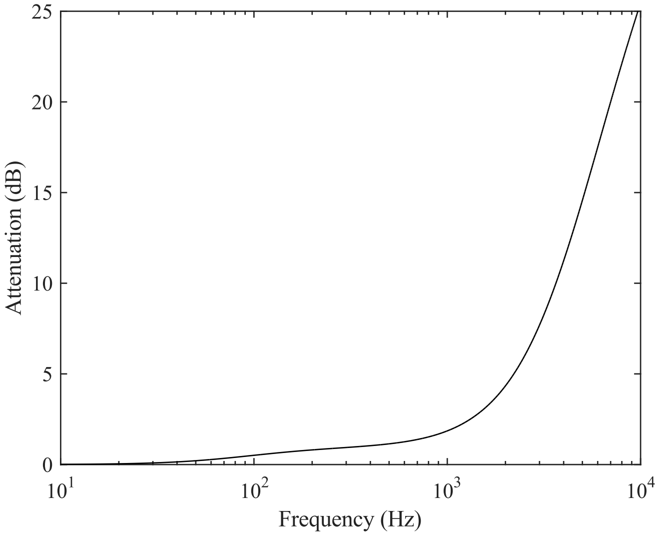

Figure 5.5: Atmospheric attenuation at a distance of 500 m as a function of frequency at a temperature of 20°C, a barometric pressure of 1 atm, and a relative humidity of 50%.

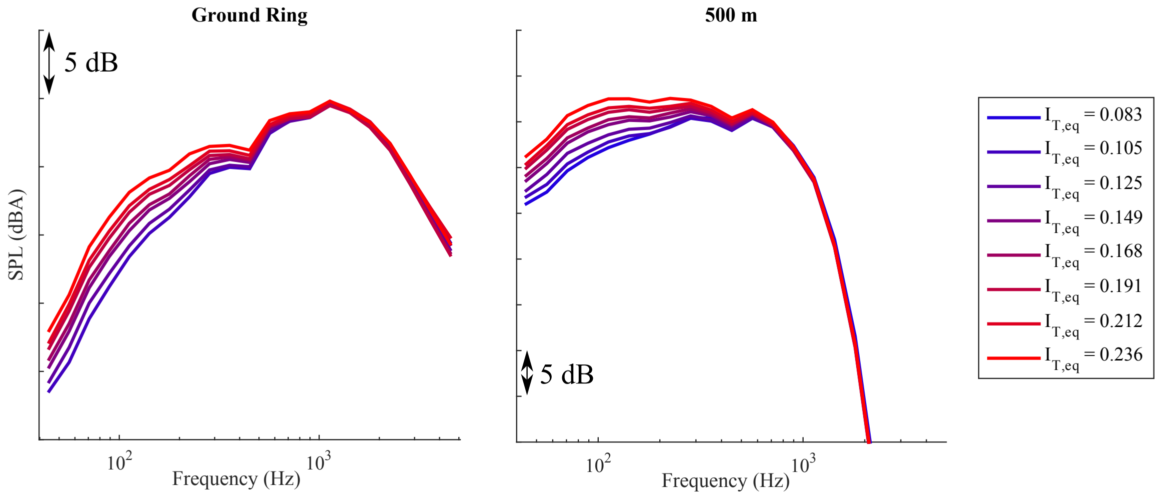

Figure 5.6: A-weighted third octave spectra measured by the downwind microphone of the ground ring (left) and predicted spectral levels at a distance of 500 m from the turbine based on the atmospheric attenuation conditions of Figure 5.5 (right). The y axes of the two plots are not the same; the low-frequency levels on the right plot are slightly quieter than the low-frequency levels on the left plot (see Figure 5.5).

pattern is decidedly inconsistent with trailing edge noise. Section 5.6 discounts the possibility that the observed correlation is due to periodic separated flow noise resulting from turbulence-induced angle of attack variations.

5.5.1 Point-source Model Development

A rudimentary wind turbine noise model was created based on an approximation of the turbine by three point sources—one on each of the blades. Theoretical observers are located in a 1-rotor-radius ring about the turbine tower base in order to mimic the ground ring measurements, and levels are averaged over a full rotor azimuth sweep. Absolute levels are not predicted, but rather the variation at the observer locations as a function of viewing angle due to directivity and convective amplification of the blade noise.

At very low frequencies, for which acoustic wavelengths are large with respect to the chord of the blade, the aeroacoustic source may be modeled as a compact, translating dipole [74, 15, 13]. The dipole directivity and convective amplification used are given by the numerator and denominator, respectively, of Equation 5.2.

$$D_l = \frac{\sin^2\theta \sin^2\phi}{(1 - M\cos\xi)^4} \tag{5.2}$$

Here, θ and ϕ refer to the location of the observer with respect to the airfoil and are defined in Figure 5.7. The angle ξ is the angle between the blade segment local inflow velocity and the source-observer line. That is, ξ is similar to θ in Figure 5.7, but measured relative to the inflow vector rather than the chord line for a finite angle of attack.

For higher frequency emission, TI noise is radiated due to interaction of the turbulence with the blade leading edge. Now, there are at least two theoretical formulations of the edge noise directivity pattern based on a flat plate approximation of an airfoil: The first, developed by Ffowcs, Williams, and Hall (FWH) [79], which was shown by Howe [40] to agree with analytical predictions of Amiet [7] for sufficiently high non-dimensional frequencies, gives a directivity of $p^2 \sim \sin^2(\theta_h/2)\sin\phi_h$, where θ_h and ϕ_h are defined in Figure 5.7. The second, a modified version of the directivity pattern given by Schlinker and Amiet [74] that was proposed by Brooks, Pope, and Marcolini (BPM) [15], gives a scaling of $p^2 \sim \sin^2(\theta/2)\sin^2\phi$. Both follow a cardioid pattern in the plane normal to the leading edge. The difference between the two can be observed in that the latter approaches zero for the entirety of the blade section plane, whereas the former is zero only in the upwind direction (downwind in the case of high frequency TE noise) and along the leading edge. As noted by Oerlemans et al. [64], the FWH pattern does not produce the noise dips in the rotor plane observed in both their study and the results presented here. Thus, the formulation of BPM is used here with the fourth power convective amplification factor of Brooks and Burley [13].

$$D_h = \frac{2\sin^2(\theta/2)\sin^2\phi}{(1 - M\cos\xi)^4} \tag{5.3}$$

The two airfoil directivity patterns are shown in Figure 5.8 below, excluding convective amplification effects.

Finally, the TE noise directivity is given by Equation 5.3, but with θ replaced by $\pi - \theta$ [53, 65]. This is due to the fact that the two mechanisms are quite similar in nature but radiated from opposite edges: TI noise is caused by atmospheric turbulence interacting with the discontinuity of the leading edge, whereas TE noise is caused by boundary layer turbulence interacting with the trailing edge.

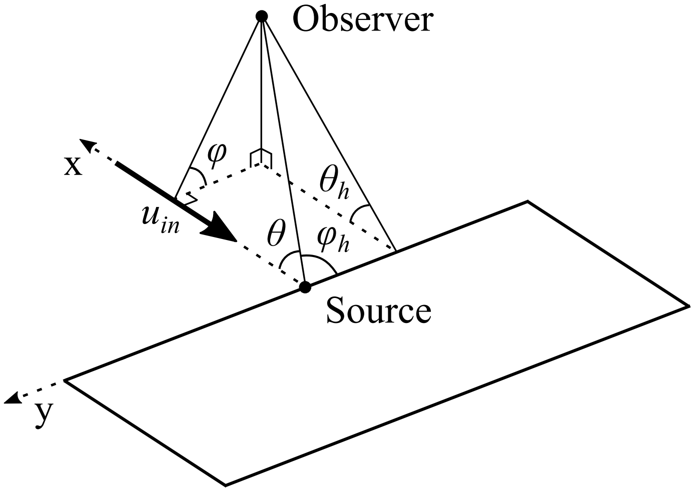

Figure 5.7: Definition of coordinate angles for the airfoil noise directivity functions. For a finite angle of attack all angles are referenced to the chord line, not the inflow vector.

The radial location of each source is chosen based on a scaling analysis of source strength as a function of radial location. Lowson [49] states that low frequency TI noise scales as $p^2 \sim u_{in}^4 u'^2$,

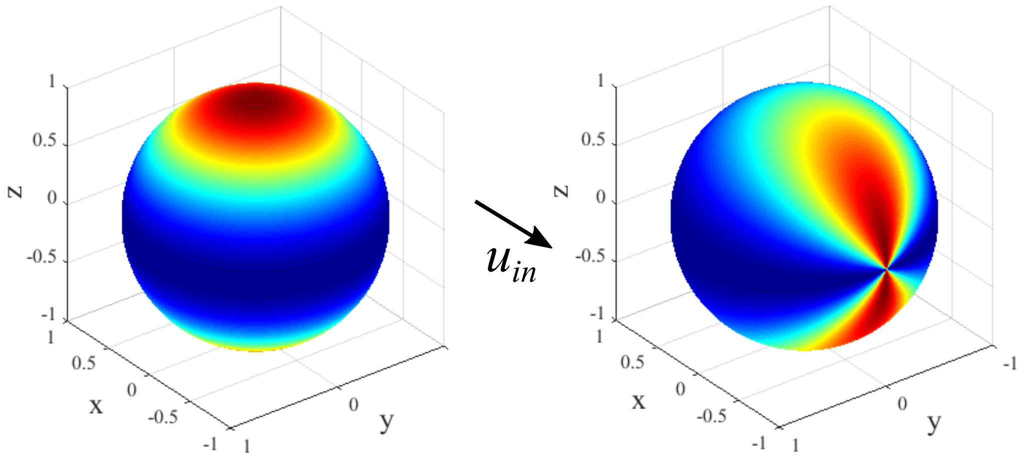

Figure 5.8: Theoretical low frequency dipole radiation pattern (left, Equation 5.2) and high frequency leading edge noise radiation pattern (right, Equation 5.3).

where again u_{in} is the mean blade inflow speed and u' is the perturbation blade inflow speed. In addition, as noted by Lowson [49], low frequency noise will scale with the square of the blade chord $p^2 \sim b^2$. Contrarily, at higher frequencies, Amiet [4] predicts that the TI noise within a given third-octave frequency bin will scale as $p^2 \sim u_{in}^3 u'^2$ and will be independent of blade chord. Assuming a uniform, isotropic turbulence field, u' can be assumed spatially constant in a root-mean-squared sense (this follows the same argument of Chapter 4). These scaling laws are physically consistent with the well established $p^2 \sim M^6$ and $p^2 \sim M^5$ laws for low and high frequency emission, respectively; the difference arises from the fact that u' is typically assumed to scale with u_{in}, whereas in the case of a wind turbine blade u' is independent of the local u_{in}. Noting that the mean inflow speed is roughly proportional to the radial coordinate r, the scaling relations $p^2 \sim b^2 r^4$ and $p^2 \sim r^3$ are used for low frequency and high frequency noise, respectively.

A similar approach is taken for TE noise. TE noise is shown by Schlinker and Amiet [74] to scale as $p^2 \sim M^5 \delta^*$, where M is the Mach number and δ^* is the turbulent boundary layer displacement thickness. Using the flat plate turbulent boundary layer relation [74]

$$\delta^*/b = 0.047\mathrm{Re}^{-0.2} \tag{5.4}$$

where Re is the chord Reynolds number, the scaling relation for trailing edge noise is found as $p^2 \sim b^{0.8} r^{4.8}$. This approximation does not take into account angle of attack, so this scaling analysis neglects the effects of angle of attack variations along the blade.

Taking the weighted average of these scaling functions along the blade span, a source location r_s is found as

$$r_s = \frac{\int p^2 r \mathrm{d}r}{\int p^2 \mathrm{d}r}, \tag{5.5}$$

where both integrals are taken along the full span of the blade. For the Siemens blade this yields a low frequency TI noise source position at 64% span, and 80% for the high frequency TI noise source. The TE noise scaling gives a source location of 79% span. This value was modified slightly to 85% span in order to better reflect experimental observations, specifically the difference in measured levels between the upwind and downwind directions. The modified source location is also consistent with the work of Oerlemans et al. [65], who experimentally found trailing edge noise to peak around 86% span and used this value in a similar point-source analysis. The effect of this adjustment was relatively minor—amounting to a difference of 0.3 dB in the downwind direction. A sensitivity analysis showed that, in general, the predicted noise characteristics are relatively insensitive to minor variations in the source location, and that the airfoil directivity pattern itself is the most significant variable.

5.5.2 Low Frequency Directivity

Figure 5.9 shows the predicted directivity compared to experimental levels. Experimental data shown are third octave levels centered at 80 Hz. The figure also shows average levels within 12° viewing angle windows. Experimental data is filtered to include only equivalent turbulence intensities between 12.5% and 14.5% because of the relatively large amount of data within this narrow turbulence window. All simulation data is normalized to match the maximum measured levels.

Several features of the simulations prove particularly valuable in comparison to experimental data. The first is the azimuthal location of the noise minima near the rotor plane—referred to

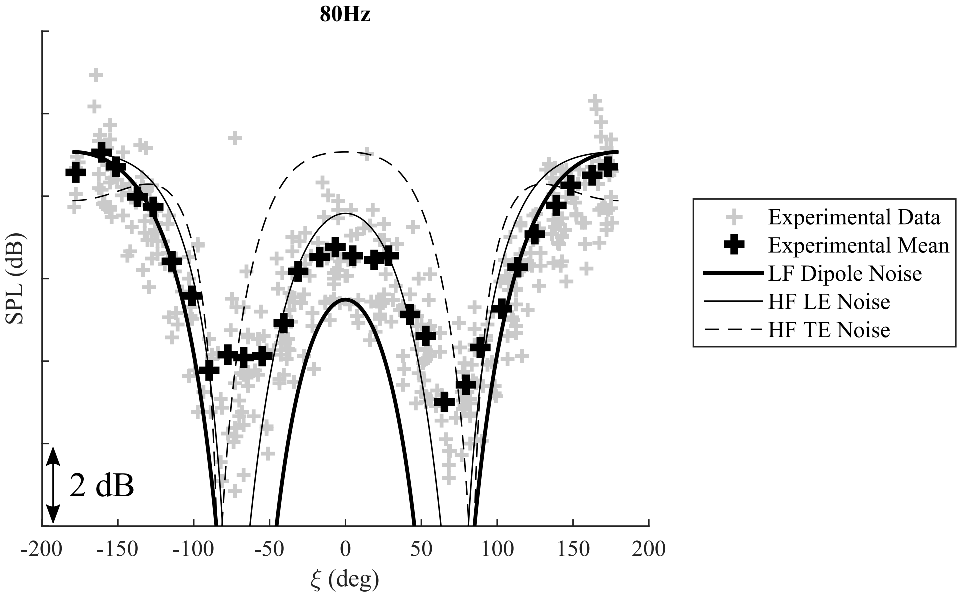

Figure 5.9: Comparison of experimental measurements to low frequency dipole, high frequency leading edge noise, and high frequency trailing edge noise patterns. Experimental data are third-octave levels centered at 80 Hz. Experimental wind speeds are between 9.0 and 11.5 m/s and equivalent turbulence intensities are between 12.5% and 14.5%.

as "noise dips"—which is directly related to the width of the upwind and down wind noise lobes. The noise dips are due to the nulls in the airfoil directivity patterns in the plane of the blade. Quantitative assessment of the location of the noise dips themselves is difficult because experimental data does not match the severity of the predicted dips. Instead, quantitative comparisons will be made based on the -3 dB beamwidth of the upwind noise lobe. For experimental data this is found via a least squares fit parabola to the averaged values within 50° of the upwind direction. The other feature useful for comparison is the difference in levels between the upwind and downwind directions. The upwind-downwind difference is caused by the rotor tilt angle with respect to th vertical plane in combination with source directivity and convective amplification. For a quantitative analysis, the upwind-downwind difference will be calculated as the difference between the means of all data within 12° of the upwind and downwind directions.

The dipole model qualitatively agrees with observations insofar as predicting noise minima in the rotor plane and the increased levels in the downwind direction versus upwind. However, the upwind-downwind difference is over-predicted by 1.3 dB. The dipole model also predicts an upwind directivity lobe that is 24° narrower than is observed. The high frequency leading edge model under-predicts the observed upwind downwind-difference by 0.8 dB. The upwind lobe-width prediction is also improved, narrower than observations by only 4°. A higher fidelity directivity study is conducted using a distributed-source model and is discussed in Chapter 6. The general result is in agreement with the point source model discussed presently: The measured directivity is more aligned with the predictions of a theoretical high-frequency edge noise pattern than with a compact airfoil, dipole-like radiation for frequencies above 100 Hz. A similar observation is discussed in the separated flow noise directivity study of Chapter 7, where separated flow noise measurements are shown to align better with the high frequency *trailing edge* noise directivity pattern than the expected compact dipole pattern [49, 13, 57].

Observations do not match the theoretical directivity of turbulent boundary layer trailing edge noise particularly well, aside from the prediction of noise dips: The upwind-downwind difference is opposite in sign and offset by 3.7 dB from observations, and the predicted beamwidth is 32° broader than observations. This supports the hypothesis that the noise mechanism resulting in the correlation to turbulence is truly TI noise and not increased TE noise due to angle of attack variations. Now, care must be taken before one can be confident in such conclusions drawn from this model due to the significant simplifications inherent in it. For example, the predicted upwind-downwind difference is highly affected by the directivity pattern used but is also affected by the source's radial location, which was chosen based on a rudimentary scaling analysis. The observed upwind-downwind difference at low frequencies could be matched using a TE noise airfoil directivity if the source were located at approximately 25% span. However, the scaling of TE noise, namely $p^2 \sim b^{0.8}x^{4.8}$, would cause TE noise at this inboard station to by weaker by roughly 20 dB than outboard TE noise, whereas the third octave spectra of Section 5.4.3 show the highest acoustic intensities at these low frequencies. In other words, the slow blade section speeds this far inboard are expected to be incapable of producing TE noise nearly as strong as the noise that is correlated to turbulence.

5.5.3 Frequency-dependence of Turbine Directivity

Figure 5.10 shows the predicted directivity along with experimental levels for four different third-octave frequency bins. The lowest frequency shown, 100 Hz, is slightly higher than that of Figure 5.9 and agrees well with the high frequency leading edge directivity pattern in both the upwind-downwind difference and in the upwind noise lobe beamwidth. This, along with the results of Figure 5.9, suggests that the transition from dipole-like radiation to leading edge noise occurs at frequencies below 100 Hz.

The bottom-right plot of Figure 5.10 shows that at frequencies above about 1 kHz the directivity follows the high frequency trailing edge noise insofar as the upwind-downwind difference and the width of the upwind and downwind noise lobes. The noise dips are far less pronounced in this frequency bin and at higher frequencies (not shown) than both observations at lower frequencies and predictions. In general, the magnitude of the noise reduction near the plane of the rotor is over-predicted, but particularly at frequencies near and above 1 kHz. The cause of the noise dips is the consistent location of the observer (microphone) near or in the plane of the blade section throughout the rotor passage, causing ϕ and, in turn, D_h of Equation 5.3 to remain near zero. Several factors likely contribute to the deviation from the predicted directivity pattern, including the approximation of a distributed source by a point source, the varying geometric twist of the blade and thus varied source orientation, and the deviation from a flat plate airfoil, which can be expected to have the most pronounced effect at high frequencies.

In Section 5.4.3, based on observed third octave spectra, the transition from TI noise-dominated low frequencies to TE noise-dominated high frequencies appears to occur at around 400 Hz. This is consistent with the shift in directivity pattern seen here. Specifically, leading edge TI noise is predicted to be directed preferentially towards the downwind microphones, and TE noise towards the upwind microphones. The measured directivity patterns show the shift between upwind and downwind preference occurring between 320 Hz and 450 Hz.

A notable and unexpected feature of the 450 Hz measured directivity, however, is the asym-

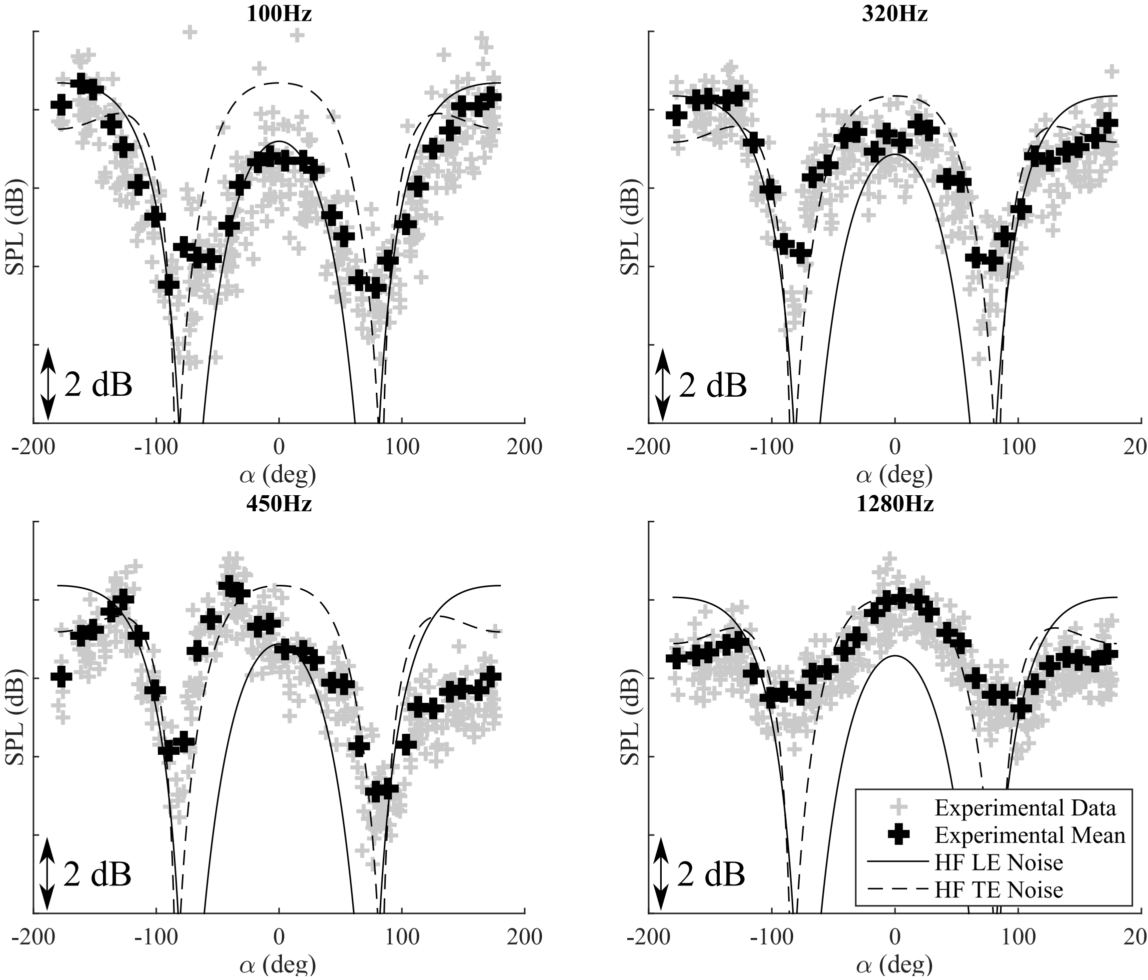

Figure 5.10: Comparison of experimental third-octave directivity measurements to theoretical high frequency leading edge and trailing edge noise radiation patterns. Experimental wind speeds are between 9.0 and 11.5 m/s.

metry about 0° viewing angle, i.e. about the plane defined by the wind direction and the vertical axis. The measured levels are significantly higher upwind and downwind of the downward passing blade than the upward passing blade, amounting to a 2.5 dB difference between viewing angles of -45° and 45°. This feature was observed across all wind speed bins analyzed—from 6.5 m/s up to 13.5 m/s—for third octave bins between about 430 Hz and 860 Hz. It is also apparent in the A-weighted directivity pattern measured by Oerlemans et al. (Figure 19 of Reference [64]), signifying that it is not a feature exclusive to the particular characteristics of this turbine or the atmospheric conditions at the National Wind Technology Center. Possible asymmetries not included in predictions include the presence of the tower and the ground. The aerodynamic effects of the tower were estimated using an approximation by potential flow around a cylinder, indicating that tower effects on blade angle of attack should be minimal and not sufficient to produce this level of asymmetry. Filtering by measured wind shear did not affect this feature, indicating that at least this ground effect is not the cause. A remaining possible cause is the *acoustic* effect of the tower. The array measurements of Buck et al. [18] as well as Oerlemans et al. [64] show some apparent tower effects on noise, particularly in the region of the bottom of the rotor. This apparent source is possibly due to suction side aerodynamic noise scattering off the tower towards the respective microphone arrays, a phenomenon that could have an asymmetric effect on a ground ring type measurement; further research is required to verify this.

5.6 Flow Stationarity Effects

This section assesses and discounts the possibility that low frequency noise, shown to be correlated to turbulence conditions in Sections 5.4.1 through 5.4.3, is due to turbulence-induced blade-flow separation and thus stall noise—i.e. not true TI noise. Stall noise can have drastic effects on the acoustics of an airfoil or wind turbine and can contribute to low frequency noise [15, 50], so care must be taken in determining the true noise mechanism being observed.

The response time of the turbine to changes in wind speed is finite and will necessarily result in deviations from design angles of attack. Specifically, a sudden increase in wind speed will result in an increased angle of attack until the turbine compensates by either an increase of rotor RPM or an increase in pitch angle. Such large scale velocity fluctuations are correlated via the turbulent energy cascade (see Figure 4.2) to the relatively small scale fluctuations measured by the blade accelerometers. It is possible that the accelerometer-measured turbulent fluctuations are correlated to large scale gusts and, in turn, stalled flow and stall noise, rather than the accelerometer-measured turbulence being directly correlated to noise.

To address this possibility, gusty conditions are detected using the available turbine instrumentation and local anemometry. Two gust filters are applied, and comparisons are made in observed trends. The first gust filter is based on measurements taken by the cup anemometer located on the downwind side of the turbine's nacelle. Figure 5.11 shows the distribution of wind speed standard deviations within each 15-second measurement for all data presented above. Wind speed standard deviation is used here to quantify gusts. While this is a metric for turbulence in general, the calculated standard deviation is only minimally affected by the small scale velocity fluctuations correlated to noise—smoothing the wind profile using a 3-second moving average typically reduces the calculated standard deviation by less than 10%. Thus, data with strong gusts can be eliminated while still keeping data with strong small-scale fluctuations. The first filter applied removes all data with wind speed standard deviations above 0.7 m/s.

The second filter is based on pitch activity. The logic here is that, while the most non-stationary wind data has now been eliminated, it is still feasible that a gust previous to a 15-second data segment results in stall during the segment. Such a gust would not affect the wind speed standard deviation of the data segment, and thus could slip through the filter described above. Now, by design, the turbine controller will react to gusts by pitching the blades to reduce excess lift (at least for operation above rated power, as in the data presented here). Such circumstances can be detected by pitch activity, which is quantified here by the standard deviation in pitch angle. Figure 5.11 shows the distribution of standard deviations in blade pitch angles. A second filter is applied to eliminate all data with pitch standard deviations above 0.6°.

With all but the most stationary 25% of data removed, the analysis of Section 5.4.2 is repeated. That is, a logarithmic fit is made to the data in order to assess the scaling of overall sound pressure level with equivalent turbulence intensity, shown in Figure 5.12. The resulting fit shows an increase of 3.68 dB for each doubling of equivalent turbulence intensity, which is almost identical to the value of 3.69 dB found with all of the data. This suggests that gusts, or non-stationary conditions, are not responsible for the correlation between turbulence and noise. Put another way, if the correlation were due to gusts and not small scale fluctuations, one would expect such data filtering to eliminate the loudest data points of Figure 5.3 and result in a flatter logarithmic fit. Conversely, while the filter has reduced the data scatter slightly, data has been

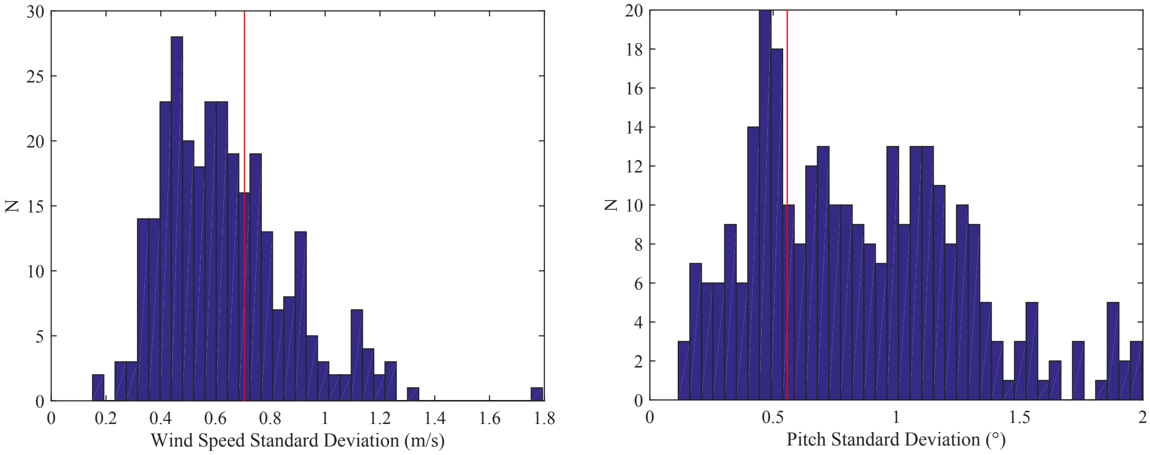

Figure 5.11: Distribution of wind gusts (left) and pitch activity (right), quantified by the standard deviations in wind speed and pitch, respectively. The red lines represent the limits of the respective stationarity filters, where data to the right of each red line is removed.

eliminated at all turbulence levels and the observed trend is statistically unchanged.

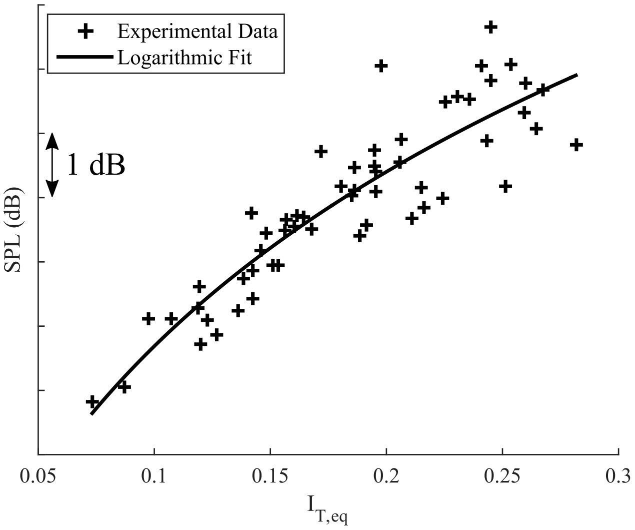

Figure 5.12: Unweighted overall sound pressure level in the downwind direction as a function of equivalent turbulence intensity $I_{T,eq}$. Each data point represents a 15-second data segment. Data is filtered by stationarity of operational conditions—wind speed and pitch—and includes the most stationary 25% of the data. Compare to the full data set of Figure 5.3.

Now considering the remaining data: The data has been filtered to include data with wind speed standard deviations no larger than 0.7 m/s. For the sake of simplicity, a Gaussian wind speed distribution is assumed. Thus, to two standard deviations—or 95% of the time—the wind speed will remain within 1.4 m/s of the mean, which is approximately 10 m/s. This means that 95% of the time the angle of attack variation about the design condition will be less than 1°, where the angle of attack is calculated as simply the angle of the local inflow vector at 85% span with respect to the rotor plane (the constant offset due to the pitch and geometric twist of the blade are of no consequence). This level of variation is not expected to result in separated flow. Further, since the angle of attack will vary spatially over the span of the blades and temporally throughout each 15-second measurement, the effect of angle of attack on TE noise is expected to largely average out to null effect, further supporting the hypothesis that the observed effect of turbulence is not due to either stall nor TE noise.

This rudimentary analysis does not eliminate the possibility of occasional turbulence induced stall. However, the consistency of the observed trends presented and discussed above are inconsistent with stall noise, which can be expected to be erratic and infrequent based on the arguments presented here.

5.7 Conclusions

Experimental findings have been presented in this chapter showing the effects of turbulence conditions in the inflow field of a wind turbine and the measured acoustic emission of the turbine. Variations in turbulence can affect overall, unweighted sound pressure levels by as much as 7 dB for the range of turbulence intensities observed at the National Wind Technology Center. The noise is shown to be predominantly in the low frequency portion of the spectrum, below about 400 Hz. For this reason, the A-weighted levels, which de-emphasize low frequencies and reflect the frequency dependence of human hearing, are only minimally affected. However, due to the efficient propagation of low frequency noise, the effect on A-weighted levels is expected to be more significant at larger distances from a wind turbine—estimated at 2 dBA at a distance of 500 m. The directivity of the noise is compared to several theoretical airfoil directivity patterns using a simple point-source turbine model. Directivity at low frequencies is found to be most consistent with leading edge noise radiated preferentially towards the trailing edge, and some indication is found that the lowest frequency noise measured—around 80 Hz—may be approaching a compact dipole radiation pattern. At high frequencies the measured directivity pattern is consistent with trailing edge noise radiated preferentially towards the leading edge. Intermediate frequency noise radiation is found to be asymmetric about the plane defined by the wind direction and vertical, which is inconsistent with theoretical predictions. The source of this asymmetry, which has also been observed in other measurements, is as of yet uncertain but may be due to acoustic scattering from the tower. Finally, it is shown that the noise observed to be affected by turbulence conditions and argued to be turbulent inflow noise is not consistent with the expected behavior of other aeroacoustic noise mechanisms—specifically trailing edge noise or stall noise. The agreement of observations with expected turbulent inflow noise behavior combined with the inconsistency with stall noise or trailing edge noise indicates that what has been measured and characterized in this chapter is in fact turbulent inflow noise.

Chapter 6

Comparison to a Standard Turbulent Inflow Noise Prediction Model

6.1 Introduction and Background

Prior research into wind turbine acoustics has been largely focused on the development of prediction models and the validation thereof. This is due to the fact that much of the fundamental theory had been derived prior to the rapid growth in wind energy production in recent decades. Net global wind energy production has increased by a factor of nearly 100 since just 1996, whereas much of the fundamental aeroacoustics [47, 26, 80, 25, 37] and airfoil noise [79, 4, 7, 40, 15] theory was developed between the early 1950's and the late 1980's. Now, aeroacoustics is not a solved problem, and significant research is being conducted to this day into improved analytical-, empirical-, and numerical-based prediction of aeroacoustic noise. That said, wind turbine acoustic noise prediction research has largely been formulated around application of the fundamental theories outlined in Section 2.1, rather than the development of novel aeroacoustic models. This dissertation uses a code that is based on the Amiet flat plate turbulent inflow noise model [4] and the Brooks, Pope, and Marcolini [15] semi-empirical trailing edge noise models, largely consistent with the wind turbine model formulation of Lowson [49]. The model developed by Lowson—and specifically the discretized-blade scheme and choice of fundamental airfoil noise models—forms the foundation for several more recent wind turbine noise codes [31, 56]. A notable exception is the model of Oerlemans et al. [64], which omitted turbulent inflow noise from predictions and was able to match measurements quite well for the mid to high frequency regime. This is nonetheless consistent with observations of Chapter 5 showing that turbulent inflow noise is influential at low frequencies.

This chapter will focus on comparison of a turbulent inflow noise prediction code to the experimental data discussed in Chapter 5. The code has been built by Siemens Wind Power based on the National Renewable Energy Laboratory's airfoil prediction code NAFNoise [59, 57]. As such, the study serves to validate wind turbine turbulent inflow noise models that are based on this or similar prediction codes. The chapter begins with a thorough derivation of Lowson's approximate form [49] of the Amiet turbulent inflow noise model [4] introduced in Sections 2.1 and 2.4, respectively. As has been expressed previously in this dissertation, the validation of wind turbine turbulent inflow noise predictions have been quite limited in the past, due at least in part to the complexities and chaotic nature of atmospheric surface layer turbulence. The large volume of data available, the thorough acoustic and atmospheric instrumentation, and the novel analysis techniques discussed in Chapter 4 and Section 6.2.2 make this the most comprehensive comparison of turbulent inflow noise predictions to experimental data to date. Comparisons are made on the basis of absolute levels, third-octave spectral shape, scaling of noise with turbulence levels, and scaling of noise with blade tip-speed. It is shown that the flat-plate airfoil analytical turbulence noise model developed by Amiet under-predicts the turbulent inflow noise levels by 3 to 5 dB, whereas the semi-empirical corrections put forth by Moriarty of the National Renewable Energy Laboratory reduces prediction errors to less than about 3 dB. Sound level trends with turbulence dissipation rate are predicted to within 1.5 dB, and at high turbulence levels within 0.2 dB. A simple airfoil directivity model is used in predictions and is shown to be accurate within 1-1.5 dB outside the rotor plane and above frequencies of about 100 Hz.

6.2 Noise Modeling

The turbulence noise prediction model to be validated is part of Siemens' full wind turbine noise prediction code xNoise [28]. Predictions are based on the commonly implemented, discretized blade scheme [49, 31, 59, 64], where each blade is approximated by several finite-span sections, and each section's noise is predicted based on 2-d models. For this study, the blade is broken into several equal sized sections between 50% span and the blade tip, which was shown to be sufficient based on a simple convergence study.

The code contains models for several noise mechanisms, but for the purposes of this study only TE noise and TI noise are included and discussed as noise measurements show these two mechanisms to be dominant. This section outlines the theory behind both of these models, though far more emphasis is placed on TI noise modeling since it is the focus of this study.

6.2.1 Lowson's Approximation of Amiet's Model

The Amiet model has been used in several wind turbine noise prediction codes described in existing literature [49, 31, 59, 9, 76] due to its convenient formulation for application to wind turbine noise. Lowson [49] presented a form of the model that interpolates between the low frequency and high frequency asymptotic behavior of the Amiet model, and this method was subsequently used by Moriarty et al. [59, 57] in the development of NREL's computer aided wind turbine engineering tool FAST. A thorough derivation of the simplified model is presented here such that the approximations made along the way can be fully understood in the validation analysis that follows.

The derivation is broken into two sections: An expression for the noise emitted in the direction perpendicular to the airfoil plane, and a directivity factor normalized to unity in the perpendicular direction. The combination of these two factors then gives the full three dimensional noise prediction for the airfoil section. The first section of the derivation begins with Equation 22 from [4] for the acoustic power spectral density of noise in the direction perpendicular to a flat plate, rigid airfoil at zero degrees angle of attack, reproduced in Equation 6.1 below.

$$S_{pp}(x=0, y=0, z, \omega) = \left(\frac{\omega \rho_0 b}{a_0 z}\right) \pi u_{in} d \left|G(\hat{\omega})\right|^2 \Phi_{zz}(k_x = K_x, k_y = 0) \tag{6.1}$$

This equation is taken from the more general airfoil noise response function given in Equation 2.15 with x, y, and M set to zero. The Mach number M is set to zero because an observer in a location directly perpendicular to the free stream from a sound source sees no convective amplification of the sound [5]. In Equation 6.1, S_{pp} is the far field acoustic power spectral density (PSD), x, y, and z are the coordinates shown in Figure 2.1, ω is the acoustic angular frequency, $\hat{\omega} = \omega b / u_{in}$, b is the airfoil semi-chord, u_{in} is the mean local inflow speed, c_0 is the free stream speed of sound, ρ_0 is the free stream density, d is the airfoil semi-span, $K_x = \omega/u_{in}$ and $\Phi_{zz}(k_x, k_y)$ is the wave vector spectrum of the upwash turbulence integrated across all k_z.

The function $G(\hat{\omega})$ is the airfoil lift response function, equal to the airfoil loading function L of Equation 2.16 with x and y, but *not* M, set to zero. The Mach number M is not set to zero here in order to include compressibility effects on source strength. Amiet offers two formulations of the airfoil lift response function for the low and high frequency limits, respectively. The low frequency airfoil lift response is given by Equation 6.2.

$$G_L(\hat{\omega}) = \left\{ \frac{1}{\beta} S(\hat{\omega}/\beta^2) \left[J_0(M^2\hat{\omega}/\beta^2) - iJ_1(M^2\hat{\omega}/\beta^2) \right] \right\} e^{-i\hat{\omega}} \tag{6.2}$$

Here $S(\hat{\omega})$ is the Sears function, $\beta^2 = 1 - M^2$, and J_0 and J_1 are Bessel functions of the first kind. This formulation is intended for use in the range where $M\hat{\omega}/\beta^2 < \pi/4$, which for low Mach numbers can be interpreted as airfoil chords smaller than a quarter acoustic wavelength. Blade tip speeds for modern industrial scale wind turbines reach Mach numbers of approximately 0.2 [20]. As such, $J_0 \to 1$ and $J_1 \to 0$ for the flow regimes of interest in this dissertation and for these low frequencies, giving the following simpler formula.

$$G_L(\hat{\omega}) = \frac{1}{\beta} S(\hat{\omega}/\beta^2) e^{-i\hat{\omega}} \tag{6.3}$$

The lift response function in the limit of high frequencies is given by Equation 6.4.

$$G_H(\hat{\omega}) = \frac{-i}{\pi\hat{\omega}M^{1/2}} \tag{6.4}$$

For simplicity and perhaps computational speed, Lowson [49] creates an interpolation scheme between these two lift response functions, ignoring the analytical function given by Amiet [4] for the lift response at frequencies just above $M\hat{\omega}/\beta^2 > \pi/4$ (for which Equation 6.4 is the high frequency asymptote). The same procedure will be taken here in order to determine the accuracy of several existing models based on this method.

Lowson's approximation begins with the high frequency lift response function $G_H(\hat{\omega})$ and follows a similar procedure to Amiet [4] in his simplification of his own model. A von Kármán turbulence spectrum is assumed, for which the turbulence spectral function $\Phi_{zz}(k_x, k_y)$ is given by Equation 6.5.

$$\Phi_{zz}(k_x = K_x, k_y = 0) = \frac{4}{9\pi}\frac{\sigma_z^2}{k_e^4}\frac{K_x^2}{1 + K_x^2/k_e^2} \tag{6.5a}$$

$$k_e = \frac{\sqrt{\pi}}{L}\frac{\Gamma(5/6)}{\Gamma(1/3)} \tag{6.5b}$$

Here, $K_x = \omega/u_{\text{in}}$, σ_z is the root-mean-squared fluctuation velocity in the direction perpendicular to the blade section (see Figure 2.6), k_e is the wavenumber scale of the energy-containing turbulent eddies, L is the integral length scale of te turbulence, and Γ is the gamma function.

All components of the acoustic PSD function Equation 6.1 are now defined. Substituting the high frequency lift response (Equation 6.4) and the von Kármán turbulence spectrum of Equation 6.5 gives the high frequency acoustic PSD function of Equation 6.6.

$$S_{pp}^H(z, \omega) = \frac{8}{9\pi^3}\left[\frac{\Gamma(1/3)}{\Gamma(5/6)}\right]^2 \left(\frac{\rho_0}{z}\right)^2 \frac{L^2 u_{in}^4 d}{a_0} \left(\frac{\sigma_z}{u_{in}}\right)^2 \frac{(K_x/k_e)^2}{(1 + (K_x/k_e)^2)^{7/3}} \tag{6.6}$$

Note that a factor of two has also been included in Equation 6.6 because the wave vector spectrum $\Phi_{zz}(k_x, k_y)$ extends to negative wave vector components, whereas the acoustic spectrum is given in terms of only positive frequencies ω. This narrowband spectral function is then converted to a third-octave sound pressure level (SPL) by multiplication by a third-octave bandwidth $\Delta\omega = 0.232\omega$. This is an approximation of the integration of the narrowband function across the same bandwidth, so the frequency in the function after integration should be taken as the center frequency of the relevant third-octave band. The resulting third-octave spectral function is given by Equation 6.7a, in a form similar to that of Moriarty et al. [57].

$$\text{SPL}^H = 10\log_{10}\left[\rho_0^2 a_0^4 \frac{Ld}{r^2} M^5 \left(\frac{\sigma_z}{u_{in}}\right)^2 \frac{(K_x/k_e)^3}{(1 + (K_x/k_e)^2)^{7/3}} D\right] + 78.4 \text{ (dB)} \tag{6.7a}$$

$$78.4 \text{ (dB)} = 10\log_{10}\left[\frac{8}{9\pi^{5/2}}\frac{\Gamma(1/3)}{\Gamma(5/6)}\right] + 10\log_{10}[0.232] - 20\log_{10}[20\text{e-}6 \text{ Pa}] \tag{6.7b}$$

This third-octave band level is normalized by a factor of $(20\ \mu\text{Pa})^2$, making the function unit-dependent and requiring use of SI units for proper application. An alternative approach is taken by Amiet [4] where the factor of $\rho_0^2 a_0^4$—which has units of pressure-squared—is taken out of the function, leaving only non-dimensional ratios and giving an additive term of 181.3 dB. The flexibility of the form taken here is preferred, however, given the altitude of the NWTC, where the present research is conducted. Note also that the factor of $1/z^2$ has been replaced with the more general factor of $1/r^2$, where r is the absolute source-observer distance, and the addition of a directivity term D, which is discussed further below.

A similar function can readily be derived for the low frequency third-octave levels. Lowson instead made note that the low frequency and high frequency functions only differ by the lift response $G(\hat{\omega})$ of the respective frequency regimes, i.e. by a low frequency correction factor LFC given by Equation 6.8.

$$\mathrm{LFC} \equiv \frac{|G_L(\hat{\omega})|^2}{|G_H(\hat{\omega})|^2} = \frac{\pi^2 S^2(\hat{\omega}/\beta^2)\hat{\omega}^2 M}{\beta^2} \tag{6.8}$$

Lowson then interpolates between the low frequency and high frequency prediction models according to Equation 6.9, a method subsequently used by Fuglsang et al. [31] and Moriarty et al. [59, 56] in their respective wind turbine noise codes—the latter of which is included in NREL's publicly available wind turbine computer aiding engineering code FAST.

$$\mathrm{SPL}_{\mathrm{inflow}} = \mathrm{SPL}^H + 10\log_{10}\left(\frac{\mathrm{LFC}}{1+\mathrm{LFC}}\right) \tag{6.9a}$$

$$S^2(\hat{\omega}/\beta^2) = \left[\frac{\hat{\omega}}{\beta^2} + \left(1 + 2.4\frac{\hat{\omega}}{\beta^2}\right)^{-1}\right]^{-1} \tag{6.9b}$$

Here, $\mathrm{SPL}_{\mathrm{inflow}}$ is the final expression for the turbulent inflow noise third-octave levels, and Equation 6.9b is an approximation of the compressible Sears function [70].

6.2.2 Simplification of Turbulence Spectral Model

A modification to the formulation of this TI noise model is first made, so as to facilitate the xNoise turbulent inflow noise model validation process. The common formulation of Equation 6.9 characterizes the turbulence based on two quantities: the turbulence intensity $\mathrm{I_T} = (\sigma_z/u_{in})$ and the turbulence integral length scale L, owing to the fact that the Amiet model assumes a von Kármán turbulence spectrum. The form of the von Kármán energy spectrum is given by

Equation 6.10 [39, 4].

$$E(k) = \frac{Ik^4}{\left[1 + (k/k_e)^2\right]^{17/6}} \tag{6.10a}$$

$$I = \frac{55}{9\sqrt{\pi}} \frac{\Gamma(5/6)}{\Gamma(1/3)} \frac{\sigma_z^2}{k_e^5} \tag{6.10b}$$

Here, $k = (k_x^2 + k_y^2 + k_z^2)^{1/2}$ is the turbulence wavenumber and I is the Loitsianskii integral [39]. It is now argued that noise prediction for wind turbines can be made based on a Kolmogorov spectrum, whose energy spectrum is given by Equation 6.11 [39], instead of the von Kármán spectrum.

$$E(k) = A\epsilon^{2/3}k^{-5/3} \tag{6.11}$$

Here, A is a universal constant set to 1.65 in the current study [81] (see Section 4.4), and ϵ is the turbulence dissipation rate. This modification will serve to reduce the required number of measured quantities from two to one and, more importantly, is given in terms of a quantity that can be reliably calculated within a 15-second acoustic measurement. Contrarily, both the turbulence intensity and integral length scale require on the order of several minutes to tens of minutes to properly calculate for atmospheric turbulence [66]. Further, as both quantities are highly dependent on very large scale fluctuations—shown below to have negligible impact at acoustic frequencies—the turbulence dissipation rate is seen as a far more relevant parameter to acoustic predictions. Notably, the following validation process *could* be carried out using the equivalent turbulence intensity $\mathrm{I}_{\mathrm{T,eq}}$ used in Chapter 5 and a derived constant value for the integral length scale L, but the present method is seen as more logical due to its simplicity.

The left plot of Figure 6.1 shows several von Kármán turbulence spectra along with a Kolmogorov spectrum, where all high frequency asymptotes have been intentionally matched. The right plot of Figure 6.1 shows an energy spectrum measured by the ultrasonic anemometer at hub height. What is observed, and what is consistent throughout measurements at the NWTC, is that the inertial sub-range of the turbulence spectrum, characterized by a $k^{-5/3}$ roll-off, extends to very large length scales (low frequencies). This means that the low frequency behavior of the turbulence can effectively be ignored in acoustics, where only frequencies above 20 Hz are typically of

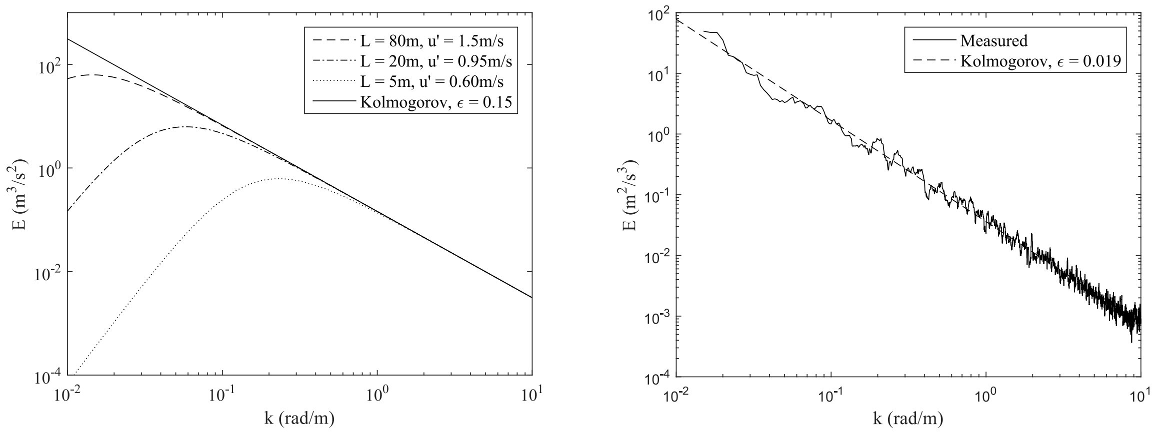

Figure 6.1: Three von Kármán spectra with various integral length scales along with a Kolomogorov spectrum (left) and a measured, 10-minute energy spectrum with a fitted Kolmogorov spectrum overlayed (right). A moving average of 20-sample width is applied to the measured spectrum for smoothing, and the measured frequency is translated to a wavenumber via Taylor's hypothesis [66].

interest. In fact, it is shown using xNoise that the acoustic difference between the $L = 80$ m and the $L = 5$ m spectra shown is less than 0.1 dB at 20 Hz. While the NWTC has unusually large turbulence scales—$L \sim 200$ m [22]—the integral length scale is typically taken to scale roughly with height above the ground [9, 49, 59], so for industrial scale turbines this is likely a widely applicable simplification.

Thus, the TI noise model is modified as follows. Noting that acoustic frequencies are within the inertial subrange—i.e. the high frequency asymptote of both the von Kármán spectrum of Equation 4.8 and, in turn, the third-octave acoustic spectrum function of Equation 6.7a—the third-octave prediction is reduced to Equation 6.12.

$$\mathrm{SPL}^H = 10\log_{10}\left[\rho_0^2 c_0^2 \frac{d}{r^2} M^3 L^{-2/3} \sigma_z^2 K_x^{-5/3} D\right] + 76.3 \tag{6.12}$$

Note that Equation 6.12 still implicitly contains the expected M^5 scaling. Normalizing the turbulent energy by the mean inflow speed squared gives this scaling explicitly, as is common practice, though the present approach leads to the simplest expression for the current purpose. Matching the high frequency asymptote of the von Kármán spectrum to the Kolmogorov spectrum gives

$$L^{-2/3}\sigma_z^2 = A\epsilon^{2/3}\frac{9\pi^{1/6}}{55}\left(\frac{\Gamma(1/3)}{\Gamma(5/6)}\right)^{5/3} \tag{6.13}$$

Substitution into Equation 6.12 then gives desired expression for the third-octave levels. Note that this modification only amounts to considering a specific frequency regime of the same physical model. Thus, all other aspects of the model are unaffected, and the high frequency asymptote of the TI noise model based on a Kolmogorov turbulence spectrum is given by Equation 6.14, including the minor correction factor for finite angle of attack [57]. This is the model included in Siemens' wind turbine noise code xNoise to be validated in this study.

$$\mathrm{SPL}^H = 10\log_{10}\left[\frac{\rho_0^2 c_0^2 d}{r^2}M^3\epsilon^{2/3}K_x^{-5/3}D\right] + 77.6 \tag{6.14a}$$

$$\mathrm{SPL}_{\mathrm{inflow}} = \mathrm{SPL}^H + 10\log\left(\frac{\mathrm{LFC}}{1+\mathrm{LFC}}\right) \tag{6.14b}$$

$$\mathrm{LFC} = \pi^2 S^2(\hat{\omega}/\beta^2)(1+9\alpha^2)M\hat{\omega}^2\beta^{-2} \tag{6.14c}$$

Here, LFC is the low frequency correction factor modified to reflect angle of attack effects, α is the angle of attack in radians, and S is the approximate compressible Sears function given by Equation 6.9b.

6.2.3 Correction for Finite Thickness Airfoils

A second model to be assessed is taken from Moriarty et al. [58]. The model is based on interpolation of the Guidati model for TI noise from airfoils of finite thickness [36], which is thoroughly discussed in Section 2.4. An interpolation is beneficial in that the full model requires significant computation time, making it ineffective as a tool in the turbine design process. The Guidati model, and its interpolated model, predict trends with airfoil thickness well, but not absolute levels. As such, the model is used to predict the spectral difference from a flat plate airfoil, and the flat plate absolute levels are taken from Amiet. Further, the original experimental validation of the Guidati model against airfoils in a wind tunnel [57] showed that this method of using Amiet as a foundation performed quite well in predicting absolute levels if a correction factor of 10 dB was applied—the

10 dB term in Equation 6.15. This turns out to agree with observations of the current dataset as well. Thus the model, deemed the Guidati-Moriarty (G-M) model in this dissertation, is given by Equation 6.15.

$$\mathrm{SPL}_{\text{G-M}} = \mathrm{SPL}_{\text{inflow}} + \Delta\mathrm{SPL} + 10\mathrm{dB} \tag{6.15a}$$

$$\Delta\mathrm{SPL} = -\left[1.123(T_{rel,1\%} + T_{rel,10\%}) + 5.317(T_{rel,1\%} + T_{rel,10\%})^2\right](2k_a b + 5) \tag{6.15b}$$

Here, $T_{rel,1\%}$ and $T_{rel,10\%}$ are the the airfoil thicknesses, normalized by the chord, at 1% and 10% chord locations, respectively. The term b is the semi-chord, and k_a is the acoustic wavenumber.

6.2.4 Directivity Model

Section 5.5 discusses several theoretical directivity models for airfoil noise and subsequently compares these models to observations at the Boulder turbine. It was shown that of the three models—low frequency (LF) dipole, high frequency leading edge (HF LE), and high frequency trailing edge (HF TE)—the low frequency turbine noise is most consistent with the HF LE noise model, and the high frequency noise best matches that of the HF TE noise model. These directivity models are commonly implemented in prior research [74, 15, 13, 49, 57] due to their simplicity and relative accuracy, with some selection criterion for whether to use the low frequency dipole pattern or the high frequency edge noise (can be either trailing edge or leading edge) pattern. Brooks et al. [15] use the dipole pattern for separation and stall noise, but the HF TE for all other self noise mechanisms. Moriarty et al. [59] takes a similar approach, choosing the radiation pattern based on the aeroacoustic source in question; the LF dipole pattern is used for TI noise and stall noise, whereas the HF TE pattern is used for TE noise, laminar boundary layer vortex shedding noise, etc. Lowson [49] notably does not include directivity in his prediction code because measurements were typically made at relatively large distances in the downwind direction.

In reality the radiation pattern of airfoil noise is frequency dependent, converging to a dipole source at low frequencies and to the HF edge noise pattern at high frequencies. Specifically, it is a function of the acoustic wavelength relative to the airfoil chord length [4, 74, 70]. Consideration will be given to this frequency dependence here due to the perhaps surprising result of Section 5.5 that TI noise more closely resembled a HF LE pattern than a LF dipole pattern [17], as proposed by Moriarty et al. [59], even at frequencies as low as 100 Hz. The frequency dependence of the airfoil noise directivity results from the far-field phase interaction of dipole sources distributed over its surface [26, 4, 40]. At sufficiently low frequencies for a finite chord airfoil the distance between these point-dipoles is small compared to an acoustic wavelength. This causes constructive interference and ultimately an airfoil behaving as a single point-dipole source. At higher frequencies the phase interaction is non-negligible, and the interference pattern becomes a complex function of the observer location containing multiple radiation lobes.

The full, frequency dependent directivity model can be conveniently derived from the work of Paterson and Amiet [70]. The work is based largely on the work of Amiet [4] with an unsteady lift function taken from Adamczyk [1]. The derivation begins with Amiet's equation for the far-field acoustic PSD given by Equation 2.15. The directivity—parameters that are functions of observer position—can be extracted simply, giving Equation 6.16.

$$D(\vec{x},\omega) = \left(\frac{z}{\sigma^2}\right)^2 |L(\vec{x},k_x = K_x, k_y = 0)|^2 \tag{6.16}$$

Here, $\sigma = \sqrt{x^2 + \beta(y^2 + z^2)}$, $\beta = \sqrt{1 - M^2}$, and $K_x = \omega/u_{\text{in}}$. The function $L(\vec{x}, k_x, k_y)$ is an unsteady loading function defined by Equation 2.16. The k_y component of the turbulent wavenumber is set to zero because the loading function L is generally independent of k_y for the condition of $MK_x \gg k_y$ [4]. As discussed in Section 2.1, far field noise is generated predominantly by turbulence wavevectors with $k_y = \omega y/a_0\sigma$, thus L becomes independent of k_y for $y/\sigma \ll 1$. This assumption breaks down for large y, i.e. for observers aligned with the span. Since the noise approaches zero here, errors are likely to be inconsequential.

The loading function is derived by Adamczyk [1] in a similar manner to the Schwartzschild method used by Amiet [6], except a far-field radiation boundary condition is imposed instead of an upstream, zero-potential condition. The governing equations are first solved for a semi-infinite flat plate downstream of a leading edge, and a correction is made to impose the Kutta-

Joukowski condition of zero pressure jump at the trailing edge. This yields the loading functions of Equation 6.17.

$$L_1(\vec{x}, k_x, k_y = 0) = \frac{1}{\pi}\sqrt{\frac{1}{(1+M)\bar{k}_x\Theta_1}}E^*(2\Theta_1)e^{i\Theta_2} \tag{6.17a}$$

$$L_2(\vec{x}, k_x, k_y = 0) = \frac{1}{\pi\Theta_1\sqrt{2\pi(1+M)\bar{k}_x}}e^{i\Theta_2}\left\{i(1-e^{-i2\Theta_1}) + (1-i)\left[E^*(4\mu) - \sqrt{\frac{2}{1+x/\sigma}}\right]\right\} \tag{6.17b}$$

$$L = L_1 + L_2 \tag{6.17c}$$

Here, $\Theta_1 = \mu(1 - x/\sigma)$, $\Theta_2 = \bar{k}_x(1 - Mx/\sigma) - \pi/4$, $\bar{k}_x$ is the x wavenumber normalized by the semi-chord b, and $\mu = MK_xb/\beta^2$ relates to the acoustic compactness of the airfoil—for small Mach number $\mu \approx \omega b/a_0$. The function E^* is a combination of cosine and sine Fresnel integrals defined by Equation 6.18.

$$E^*(x) = \frac{1}{\sqrt{2\pi}}\int_0^x e^{-i\epsilon}\epsilon^{-1/2}\mathrm{d}\epsilon \tag{6.18}$$

Convective amplification effects can then be predicted by the inclusion of a retarded-time coordinate system [70, 74]. That is, the above expressions are derived for an observer fixed in the frame of the airfoil, whereas a transformation is required in order to account for source-observer relative motion.

Equation 6.16 may then be compared to the high- and low-frequency directivity asymptotes used in Section 5.5. Figure 6.2 shows the 2d directivity pattern for several values of the non-dimensional parameter μ for operational Mach numbers corresponding roughly to those of wind turbine blades. The dimensional frequencies shown begin with 100 Hz, as in Section 5.5, and increase by a factor of three for each plot. Of particular note here is that, while the *turbine* directivity resembles the point-source HF LE pattern even at frequencies as low as 100 Hz, the theoretical airfoil directivity pattern has not nearly converged to this pattern and more closely resembles a dipole radiating preferentially downstream. In Section 6.3.5 a similar directivity analysis is conducted using the present distributed source model. Two airfoil directivity functions are applied in the prediction code. The first uses the exact, frequency-dependent directivity function for both TI noise and TE noise, where the latter is identical to the former but inverted about the plane perpendicular to the chord line [53]. The second airfoil directivity model uses the high-frequency asymptote of the exact function for both TI and TE noise—similarly inverted—as in the point-source analysis of Section 5.5. The low-frequency dipole model was also applied during the investigation, but the predictions matched the exact model within 0.2 dB for most observer locations at frequencies below 250 Hz so they are not shown. The high-frequency asymptote is used as the primary directivity function for all other results presented in this chapter.

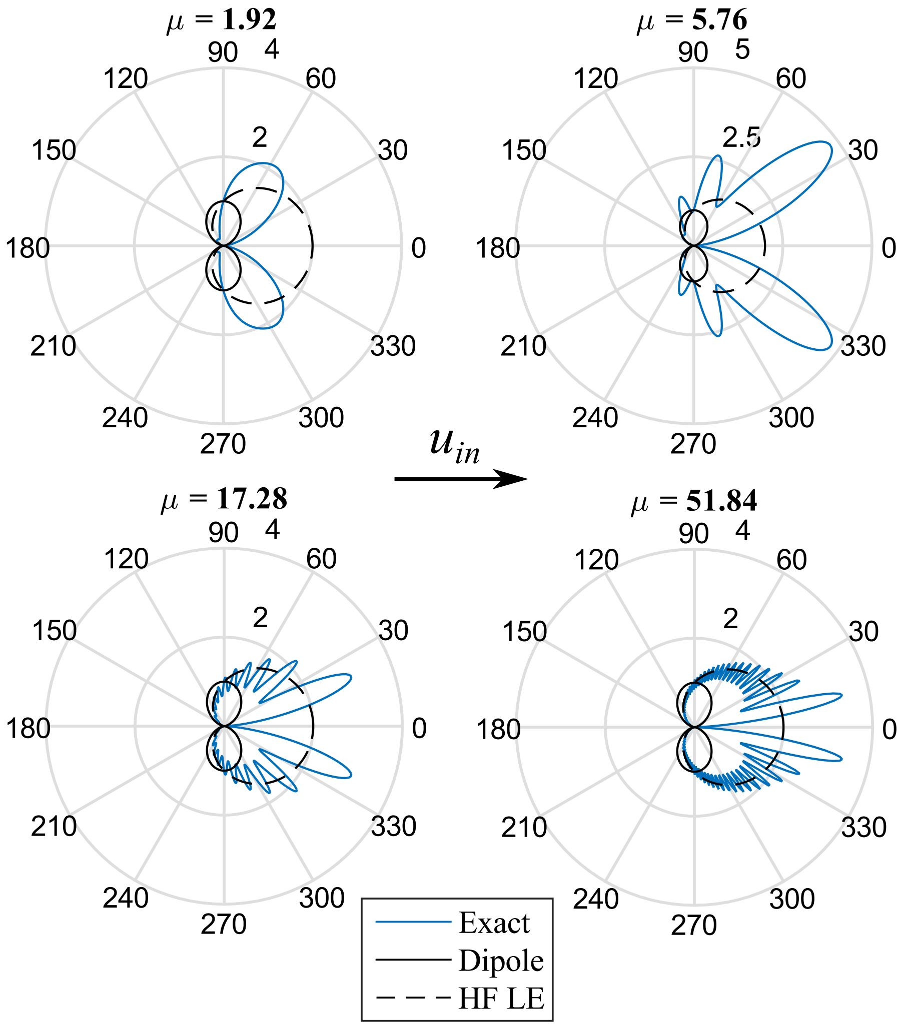

Figure 6.2: Theoretical 2d ($y = 0$) flat plate airfoil noise directivity patterns for various values of the non-dimensional frequency parameter μ. All directivity patterns are normalized to the direction perpendicular to the chord line and are given in linear units.

6.2.5 Trailing Edge Noise Model

The TE noise model in xNoise is fundamentally based on the semi-empirical relations of Brooks, Pope, and Marcolini [14] for airfoil noise detailed in Section 2.1.5. Trailing edge boundary layer displacement thicknesses are calculated using the 2-d, rotating frame airfoil code RFoil [34]. The implementation of the model originally produced by Moriarty et el. [59, 56] from NREL was modified to reflect internal acoustic measurements on Siemens wind turbines. Being that the original model is semi-empirical in itself, these modifications do not constitute a significant deviation from original theoretical formulation. The directivity pattern used is the same as for TI noise but inverted about the airfoil. See Section 6.2.4.

6.3 Results

This section presents comparisons of the models described in Section 6.2 to the experimental measurements described in Section 5.2. Comparisons are made based on several facets of the predictions, including the third-octave spectral levels, the scaling of low frequency noise with turbulence dissipation rate, and the noise directivity about the turbine.

6.3.1 Third-octave Levels

The wind speed bin selected for validation of third-octave predictions is between 9 and 11 m/s due to the large number of experimental measurements within this wind speed bin. Data is broken into four turbulence bins, and an average third-octave spectrum is calculated for each bin on an acoustic pressure squared basis. Predictions are made for a mean turbulence dissipation rate ϵ within each bin, where the mean is calculated via Equation 6.19 to reflect the scaling of acoustic pressure-squared with ϵ given by Equation 6.14.

$$\epsilon_{\text{mean}} = \left[\frac{1}{N} \sum_{i=1}^{N} \epsilon_i^{2/3} \right]^{3/2} \tag{6.19}$$

The upwind and downwind directions are shown, where experimental data is selected within 15° of the nominal direction. This is shown in Section 6.3.5 to amount to only some tenths of a dB in directivity effects. Predictions are made based on the both the Amiet flat plate model and the G-M finite thickness model (Section 6.2). Figures 6.3 and 6.4 show the resulting comparisons.

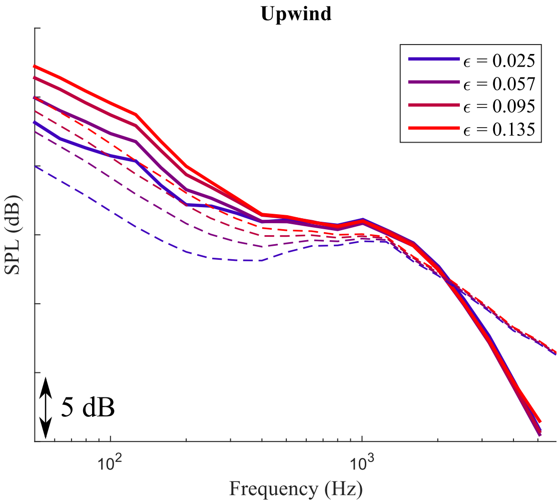

Figure 6.3: Measured (solid lines) and predicted (dashed lines) third octave sound pressure levels (SPL) in the upwind and downwind directions using the Amiet flat plate model for predictions. Wind speeds are between 9 and 11 m/s. Y-axis limits are matched between the plots.

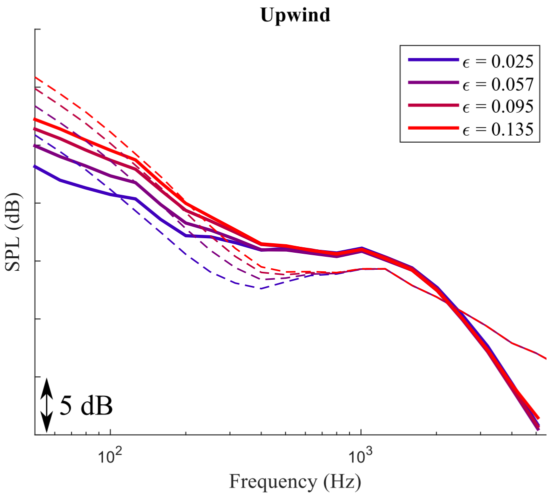

Figure 6.4: Measured (solid lines) and predicted (dashed lines) third octave sound pressure levels (SPL) in the upwind and downwind directions using the Guidati-Moriarty modifications for finite thickness airfoils. Wind speeds are between 9 and 11 m/s. Y-axis limits are matched between the plots.

Results from both models show the qualitative agreement with measurements that turbulence noise dominates the low frequency portion of the spectrum, whereas levels converge above about 450 Hz for TE noise dominated frequencies. It should be noted that these figures again show un-weighted SPL, not A-weighted. The effect of turbulence noise on overall integrated levels is significantly reduced when A-weighting is used. The Amiet flat plate model is shown to underpredict low frequency noise by between 3 and 5 dB. This is counterintuitive given that increasing thickness has been shown to reduce the acoustic radiation efficiency of an airfoil in a turbulent stream [36, 32, 58, 55]. However, it supports the empirical tuning constant of 10 dB found by Moriarty et al. [58] in the wind tunnel validation of the G-M model. The use of the G-M model, including this constant, is shown to significantly improve results insofar as predicting absolute levels. The measured spectral roll-off is not as steep as predicted by the G-M model in either the upwind or downwind directions, whereas measurements are slightly steeper than predicted by the Amiet model. The difference in spectral slope between the two models stems from the frequency dependence of the G-M thickness corrections, given by Equation 6.15. Predictions of the G-M model also deviate from measurements for low frequencies, below about 100 Hz and particularly in the upwind direction. Several factors are at play here and potentially contribute to this deviation: the frequency dependent G-M corrections, the simple interpolation between high and low frequency TI noise behavior given by Equation 6.9a, and the breakdown of the high frequency directivity approximation, as is discussed in Section 6.3.5. The response of the ground board acoustic-pressure-doubling effect at low frequencies may also contribute to the deviation. It is difficult to isolate the contributions of each factor at this point.

6.3.2 Scaling with Turbulence Dissipation Rate

The scaling of the TI noise with ϵ given by Equation 6.14 is compared to observations. Specifically, acoustic pressure squared is expected to scale as $p^2 \sim \epsilon^{2/3}$. Figure 6.5 shows comparisons of experimentally measured third-octave levels centered at 100 Hz in the downwind direction against corresponding predictions using the G-M model (which scales the same with ϵ as the Amiet model). The figure illustrates that the scaling agreement between measurement and prediction is best at moderate to high turbulence dissipation rates. The difference in SPL between $\epsilon = 0.042$ and $\epsilon = 0.146$ is overpredicted by 0.13 dB, where the measured difference is 3.47 dB. For lower turbulence dissipation rates the model falls off faster than is observed in measurements. The difference in SPL between $\epsilon = 0.011$ and $\epsilon = 0.042$ is overpredicted by 1.21 dB, where the measured difference is 2.59 dB. Repeating the logarithmic fit analysis of Section 5.4.2 (SPL as a function of $\mathrm{I_T}$) shows that the overall measured scaling law is lower than predicted, as expected from the previous analysis. The logarithmic fit suggests a scaling of $p^2 \sim \epsilon^{0.53}$, where corrections have again been made for background noise. Possible reasons for the reduced scaling have been discussed in Section 5.4.2.

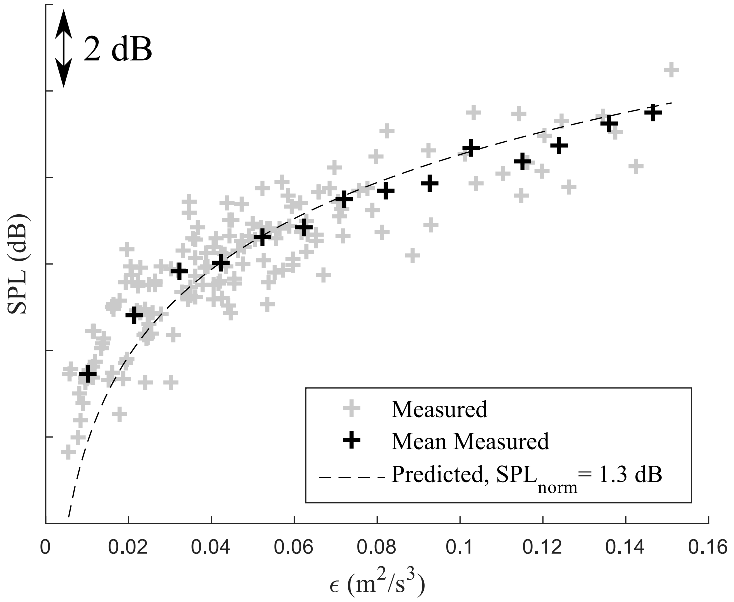

Figure 6.5: Measured and predicted third-octave SPL centered about 100 Hz versus turbulence dissipation rate ϵ. Wind speeds are between 9 and 11 m/s. Predicted levels are normalized to measured levels at $\epsilon = 0.042$ in order to illustrate trends.

6.3.3 Scaling with Blade Tip Speed

The Lowson model [49] that forms the foundation of these turbulence noise predictions and is discussed in Section 6.2 interpolates between the low and high frequency theoretical behavior of TI noise. A significant distinguishing factor between the two frequency regimes is the scaling of noise with inflow speed: For a constant turbulence intensity, or equivalently for a constant value of the normalized quantity $\epsilon^{1/3}/u_{\text{in}}$, low frequency dipole noise radiates as $p^2 \propto M^6$, and high frequency edge noise radiates as $p^2 \propto M^5$ [40, 49, 65] (see Equations 6.7a and 6.8). The interpolation made by Lowson, and subsequently implemented by Fuglsang et al. [31] and Moriarty et al. [59, 56], between low and high frequency behavior can therefore be assessed by examination of the scaling of noise with inflow speed at different frequencies. Figure 6.6 shows the measured and predicted scaling of the turbulent inflow noise-dominated frequencies with blade tip speed. Data is chosen for an approximately constant value of the quantity $\epsilon^{1/3}/u_{\text{tip}}$. The turbulence dissipation rate chosen is relatively high value of $\epsilon = 0.065$ m^2/s^3 in order to achieve a strong signal to noise ratio. Scaling laws are assessed via a logarithmic fit to both the data and the predictions. Average background noise levels are calculated for each respective wind speed and frequency bin, and measured third-octave levels are corrected. Scaling laws are assessed via a logarithmic fit to both the data and the predictions.

Several things should be noted about the figure. The first is that the scaling laws—both measured and predicted—are typically higher than even the M^6 of low frequency TI noise. This is due to the spatial sampling effect of the atmospheric turbulence. For increased local inflow speeds a given frequency noise is generated by larger scale, higher amplitude turbulent fluctuations. This causes the observed scaling for a constant-frequency bin to be higher than that of a sinusoidal gust. Spatial sampling also has a secondary effect on the scale of the relevant turbulence fluctuations with respect to the airfoil thickness and the radiation efficiency for any particular frequency. Both of these effects are accounted for in the prediction model. It is also notable that at 100 Hz and 157.5 Hz the experimentally observed trend deviates from predictions, particularly at 100 Hz. Some consideration must me made to the amount of data scatter and the uncertainty with regards to background noise effects. However, the reduced scaling exponent at 100 Hz was consistent regardless of the turbulence levels selected for data filtering—several mutually exclusive sets of data were examined—indicating that it is not likely a random occurrence due to, e.g., extraneous background noise during a few measurements. The observed deviation of measurements from the model appears to be due to non-compactness effects not captured by Lowson's interpolation, discussed further below. Nonetheless, it seems that the model generally matches measurements quite well despite its simplicity.

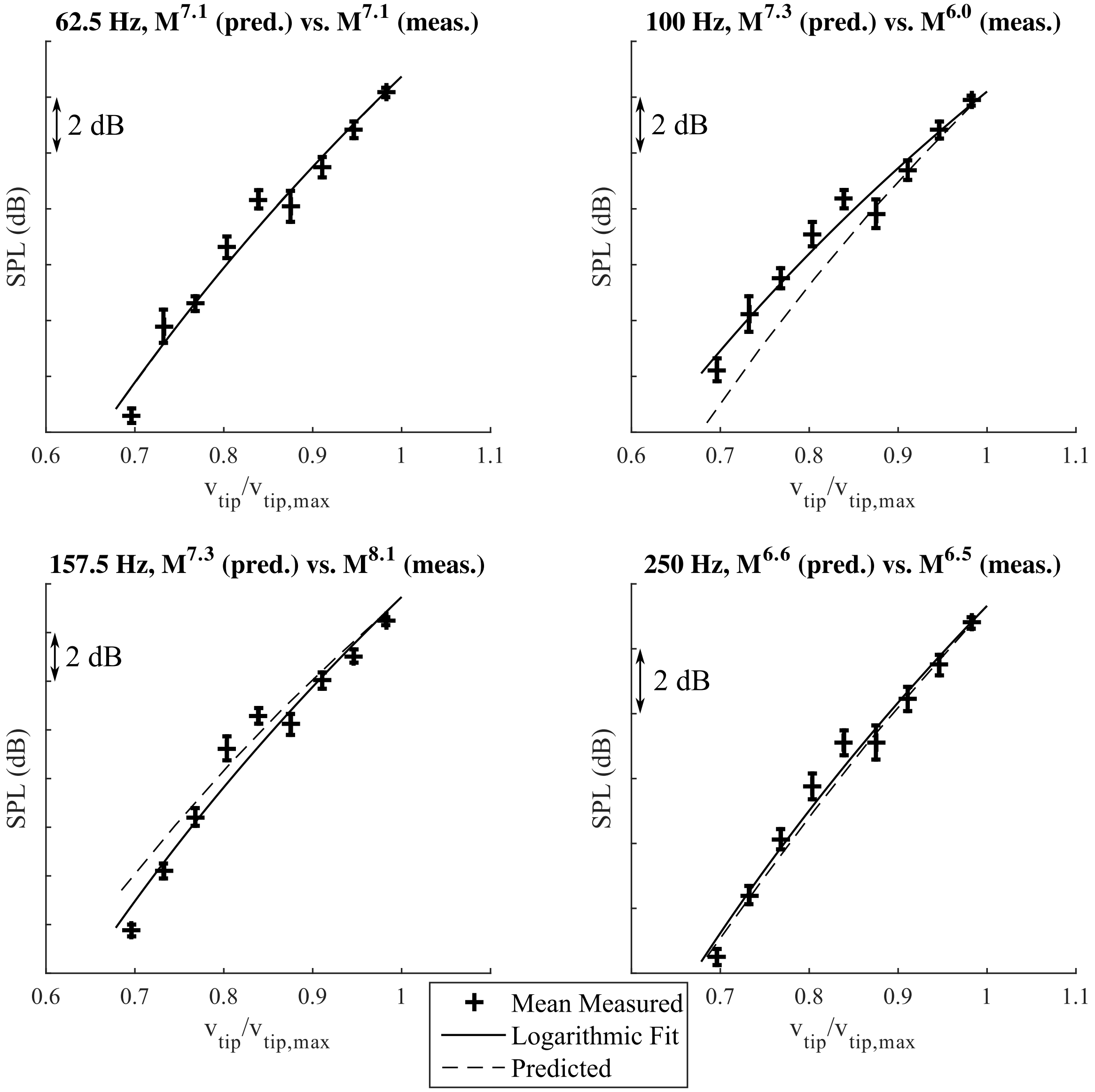

Figure 6.6: Measured and predicted scaling of turbulent inflow noise third-octave levels at various frequencies. The title of each plot gives the predicted and measured scaling laws M^n. Levels are normalized to match at the maximum noise level for each plot. Each data point represents an average of at least nine 15-second measurements, and error bars represent ± one standard error.

6.3.4 Data Collapse of Third-octave Levels

The deviation of observed behavior from predictions shown in Figure 6.6 can be further clarified by analysis of the full third-octave spectra for varying rotor speed. Figure 6.7 shows the raw third-octave spectra for the TI noise dominated frequency range, along with normalized third-octave spectra. Normalization of the x axis using Strouhal number $St = fc/v_{\text{tip}}$—where c is a typical chord length scale taken as 1 m—removes the spatial sampling effects, reducing the expected scaling for a particular St bin back to a range between M^5 and M^6. Normalization of the y axis is shown for both M^5 and M^6. Several features should be noted in the figure. Examining the spectral shape in the raw third-octave levels, it is apparent that the spectral feature observed just above 100 Hz (also apparent in Figures 6.3 and 6.4) is present at all tip-speeds shown, and is in fact more intense at lower tip-speeds. The feature appears at constant acoustic frequencies regardless of tip-speed, indicating that the acoustic wavelength is the relevant length scale, rather than the turbulence wavelength. This dependence on the acoustic wavelength is consistent with expectations for acoustic compactness effects [70], indicating a shift from compact airfoil behavior at low frequencies to non-compact airfoil behavior at higher frequencies; similar behavior can be seen in the wind tunnel tests of Roger et al. [73]. The contention that this feature is due to compactness effects is further supported by the non-dimensionalized spectra in the right plot of Figure 6.7. It is shown that at the lowest frequencies, data collapse is best for a M^6 scaling, whereas higher frequencies collapse better for a M^5 scaling, consistent with compact airfoil and non-compact airfoil behavior, respectively [40]. Note that the highest frequencies shown include effects of trailing edge noise as well, making the behavior here more complex and not within the scope of this analysis. It is apparent from the analysis of Figure 6.7 that the deviation from Lowson's model [49] shown in Figure 6.6 is due to the model's inability to track the turbine's acoustic behavior in the transition from compact to non-compact behavior, though the agreement within either acoustic regime is again noted to be quite good.

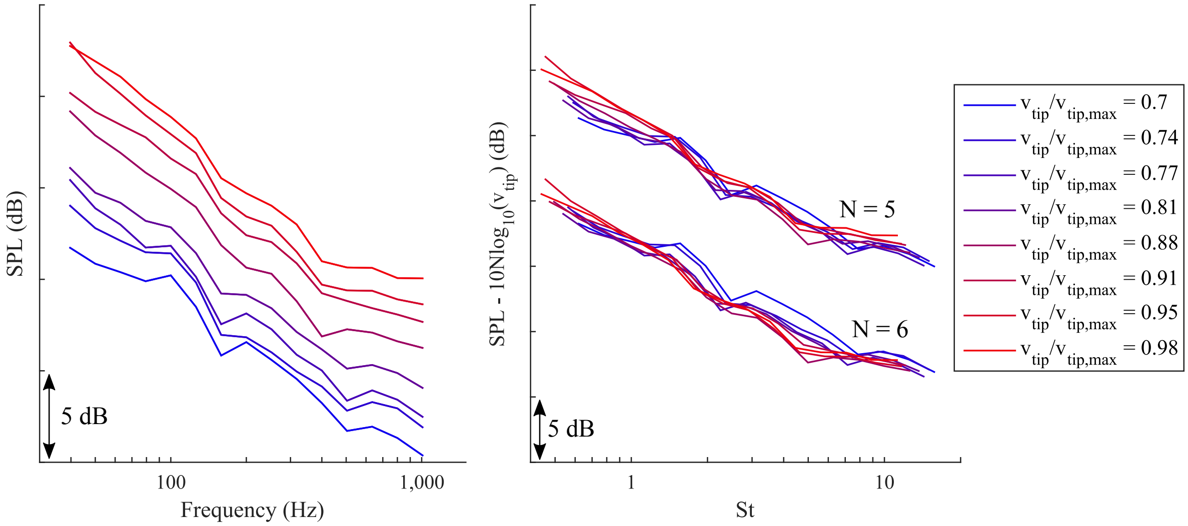

Figure 6.7: Third-octave spectra measured in the downwind direction for various blade tip speeds (left) and normalized third-octave spectra for two different theoretical scaling exponents N (right). Each spectra represents an average of at least nine 15-second measurements.

6.3.5 Turbine Noise Directivity

Figure 6.8 compares the wind turbine's measured noise directivity to the prediction model's. To clarify, the wind turbine's emitted directivity as measured by the ground ring system is referred to as the "turbine directivity", whereas the directivity of airfoil noise in the frame a blade section will be referred to as the "airfoil directivity". The former is strongly affected by the latter [65, 64], so the measured turbine directivity is a means of validating the theoretical airfoil directivity model used. As described in Section 6.2, two theoretical airfoil directivity patterns are included in the analysis. The first model uses the exact, frequency-dependent radiation pattern with multiple lobes derived in Section 5.4.1[70] for both TI noise and TE noise, but with inverted radiation orientations (see Section 5.4.1). The second uses the high-frequency asymptote of the theoretical radiation pattern for both TI noise and TE noise, as suggested by the point-source directivity study of Section 5.4.1.

Figure 6.8 shows the general qualitative agreement between both models and the experimental data that noise is significantly reduced near the plane of the rotor, particularly at low

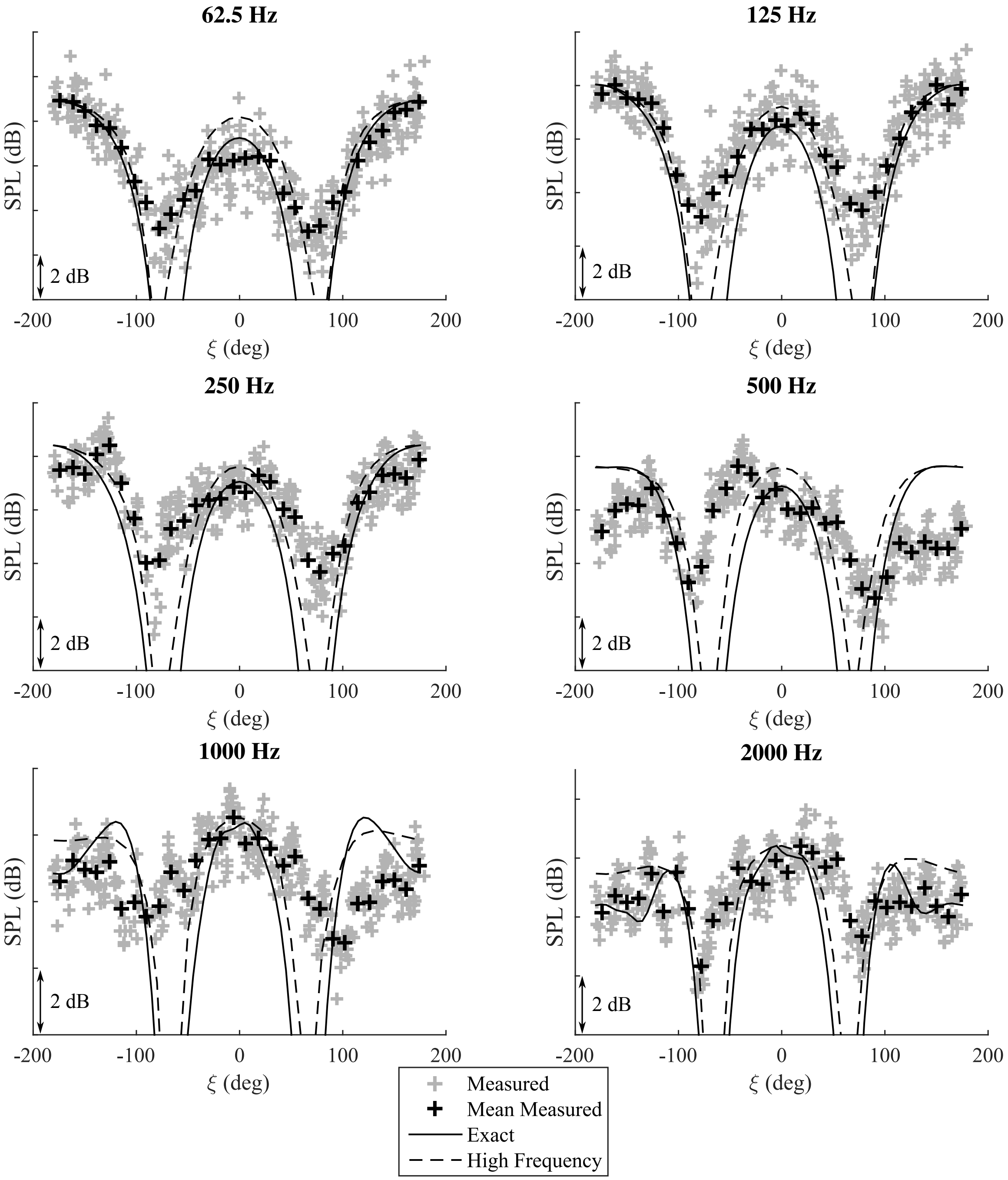

Figure 6.8: Measured and predicted turbine directivity patterns for winds speeds between 9 and 11 m/s and $\epsilon = 0.032 m^2/s^3$. Two theoretical noise directivity patterns are shown: Model 1 uses the compact dipole pattern for TI noise, and Model 2 uses the high-frequency leading edge pattern for TI noise, while TE noise emission in *both cases* is predicted using the high-frequency trailing edge noise pattern. Predicted levels are normalized such that the maximum levels match between measurements and predictions.

frequencies. For all frequencies the measured noise reduction in the plane of the rotor is not as significant as predicted. This likely owes to several approximations inherent in the directivity model, including the flat-plate approximation in its derivation, and the variation in angle of attack in the physical turbine due to unsteady loading. Oerlemans et al. [64] used a smoothed version of the theoretical directivity pattern, averaging the theoretical model over a specified solid angle, to mitigate this issue. The predicted shift from downwind preferential turbine directivity at low frequencies to upwind preferential turbine directivity at high frequencies is also observed in experimental data. Comparison of the two models shows that the simpler high-frequency directivity function approximates both the exact model and experimental observations quite well insofar as the turbine directivity prediction. At very low frequencies the exact model is more accurate, but the high-frequency approximation actually matches better to the width of the upwind directivity lobe between 125 and 250 Hz, before unpredicted features arise at moderate frequencies.

At moderate frequencies—from 450 Hz to roughly 850 Hz—a consistent asymmetry about $\xi = 0°$ is observed that is not replicated by predictions. The feature is observed across all wind speed bins from 6.5 m/s up to 13.5 m/s. This asymmetry is also apparent in the measurements of Oerlemans et al. [64], indicating that is is not a product of the conditions at the NWTC or this particular turbine. Physical asymmetries that are not accounted for in predictions include the presence of the tower and the ground. A basic calculation of the tower aerodynamic effects was conducted using an approximation by potential flow around a cylinder, indicating that tower effects on blade angle of attack should be minimal and not sufficient to produce this level of asymmetry. Wind shear is also not likely to be a significant contributor based on a shear-based data filtering study. Acoustic reflection of suction-side (downwind) blade noise radiation off of the tower is a potential cause. The array measurements of Buck et al. [18] and of Oerlemans et al.[65] show discernible effects of such acoustic scattering measured in the upwind direction. This effect is not modeled in the present study, so could be a cause for the measured asymmetry.

Finally, at 1000 Hz and above, the high-frequency approximate directivity function matches within about 1.5 dB to predictions the exact airfoil directivity, aside from measurements near the rotor plane. The exact directivity model is approximately as accurate as the HF model but predicts the presence of small local peaks in the turbine directivity (see 2000 Hz). While the small peaks do not match exactly with observations, similar features do arise in experimental data, suggesting that these measured features are likely due to the lobes of the airfoil directivity being projected to the ground ring.

6.4 Conclusions

Two turbulent inflow noise models commonly used in wind turbine applications have been compared to measurements made on a full-scale 2.3 MW wind turbine. Measurements consist of over 50 hours of acoustic data gathered simultaneously by twelve calibrated microphones in a one-rotor-radius ring about the turbine base. The first turbulent inflow noise model is based on the flat plate analytical model developed by Amiet[4] and implemented in a similar manner to several previously developed wind turbine noise codes[49, 31, 59, 9], and the second uses the corrections for finite airfoil thickness developed by Guidati and Moriarty[36, 58]. A modification is made such that the turbulence is described simply by a Kolmogorov spectrum, owing to the fact that acoustic frequencies are generated by turbulence wavelengths within the inertial subrange of atmospheric turbulence. The modification allows predictions to be made based on the turbulence dissipation rate—which can be properly calculated for each 15-second acoustic measurement—rather than the combination of turbulence intensity and integral length scale. The latter two quantities each take on the order of minutes to tens of minutes to calculate and are far less relevant in wind turbine acoustics due to the length scales of atmospheric turbulence. The turbulence dissipation rate is measured using blade-mounted accelerometers as discussed in Chapter 4 in order for the turbulence to be characterized directly in the rotor plane.

Using these methods, comparisons are made between predictions and measurements based on third-octave spectra, scaling of noise with turbulence dissipation rate, scaling of noise with blade tip speed, and the noise directivity. Third octave spectra for both predictions and experiment show that turbulence noise dominates the low frequency portion of the spectrum. The flat plate model under-predicts measured levels by between 3 and 5 dB, contrary to the expectation that flat plate airfoils radiate more efficiently than finite-thickness airfoils. Corrections for finite thickness developed by Guidati and Moriarty—including the added empirical constant of 10 dB—significantly improve absolute levels, reducing errors to typically less than 3 dB for the TI noise dominated portion of the spectrum. This result then supports the observations of Moriarty et al. [58] that a 10 dB correction factor is required for predicting absolute levels. Scaling with turbulence dissipation rate is shown to be predicted within 0.2 dB for moderate to high turbulence levels, but deviations are as high as 1.5 dB for low turbulence levels. Directivity patterns are predicted within 1-1.5 dB by the simple airfoil directivity model, which is based on the high frequency asymptote of the Amiet directivity model. Deviations from this approximation are apparent below about 100 Hz and in the vicinity of the rotor plane.

Chapter 7

Aerodynamic Stall Noise

7.1 Introduction and Prior Research

An investigation has been conducted into the acoustic effects of aerodynamic flow separation on the blades of a wind turbine. Aerodynamic separation occurs at high angles of attack due to strong adverse pressure gradients and, in turn, the development of a recirculation region—a so-called separation bubble. Beyond what is referred to as the critical angle of attack, the phenomenon causes decreases in lift and rapid increases in drag—which is the definition of aerodynamic stall—and is known to have dramatic effects on the acoustic characteristics of an airfoil [75, 15, 54, 50]. As such, wind turbines are typically designed to avoid aerodynamic separation and stall on their blades by inclusion of a stall margin, which is the difference between the design angle of attack and the stall angle of attack such that blades are robust to perturbations in operational conditions. Despite this consideration, and due to factors such as extreme gusts, wind shear, yaw error, manufacturing variability, and blade surface roughness, flow separation and aerodynamic stalling can occur in the field. It is therefore necessary to determine the acoustic effects of flow separation such that the consequences of these conditions can be fully understood and appropriate provisions can be made with respect to wind turbine design.

The amount of literature pertaining to *wind turbine* aerodynamic stall noise is relatively limited because of the requirement for these specific conditions. One can only directly measure the acoustic effects of stall either by the fortunate circumstance where measurements are gathered when these conditions arise, or by designed turbine operation for intentionally inducing stall—the latter being the case for the present investigation. The former is the case of the data acquisition campaign of the DANAERO project [50, 9]. Madsen et al. [50] analyzed unsteady surface pressure measurements for a portion of the data collected when unusually high shear conditions lead to strong angle of attack variation and, in turn, dynamic stalling. Dynamic stalling is the condition of periodic shifting between stalled and attached flow during a rotor passage. The study is discussed further in Section 2.4, and is notably one of the few cases available in literature where stalled conditions are clearly observed on a full scale wind turbine. Surface pressure fluctuations show an increase in low frequency spectral amplitude of up to 15 dB for the highest angles of attack that occurred, presumably for separated flow conditions. The far field noise was not measured during this study.

In a study previous to the Madsen et al. [50] measurements, Oerlemans [61] postulated that dynamic stalling is a plausible cause of what is referred to as “thump noise” and has been described in several other studies, e.g. [12, 77, 27]. Thump noise is an extreme variation in noise level at the blade passing frequency that has long been qualitatively distinguished from normal wind turbine amplitude modulation, though its causes, characteristics, and even its existence had been the subject of some debate. Oerlemans notes that in these prior wind turbine noise studies, the level of amplitude modulation is inconsistent with expectations for normal turbine operation. Normal amplitude modulation of wind turbine noise is due to the directivity and convective amplification of airfoil noise combined with the periodic motion of the blades [65] and is most significant in the geometric near field of the turbine. At large distances upwind and downwind this normal swish approaches zero due to minimal source angle variation and relative motion. Contrarily, Di Napoli [27] measures modulation depths—the difference between peak and trough noise level—of up the 5 dB at a location 530 m downwind of a 1 MW turbine. Detailed inflow measurements and operational conditions are not available for this study. The dynamic stall noise model developed by Oerlemans [61] and described in Section 2.4 was shown to qualitatively agree with the modulation noise characteristics of these studies, though for the same reasons it was not possible to perform a thorough quantitative validation.

Several wind tunnel investigations into separated flow dynamics and acoustics have also been conducted, which provide far greater control over aerodynamic conditions and typically more detailed measurements. Two wind tunnel studies in the late 1960's and early 1970's [29, 30] analyzed separated flow behind obstacles by placing a solid fence on the wind tunnel wall. Measurements were used to create a set of non-dimensional empirical models for pressure fluctuations downstream of the obstacles as a function of characteristic flow parameters, including a characteristic obstacle dimension. These studies, while showing reasonable prediction capability, are not likely applicable to airfoil separation, which is typically caused by extended adverse pressure gradients rather than by discrete obstacles. Further, the dimensions of the recirculation region are not in general known. However, these measurements do agree with observations of airfoil separation in their measured order-of-magnitude increase in surface pressure fluctuation amplitude versus that of attached boundary layer turbulence [75, 54, 50].

Flat plate and finite thickness airfoil wind tunnel tests have been conducted as well [75, 52, 15, 54] and are more relevant to the present study. Sharland [75] made what appears to be one of the earliest measurements of separated flow noise in a wind tunnel. The study investigated aerodynamic noise from axial flow fans using a model ducted fan rig inside a wind tunnel. Single-microphone measurements are made at several locations in the flow, and investigations are conducted with and without a turbulence generating annulus upstream of the model. Of particular interest here is the study of angle of attack effects, where the angle of attack is controlled via the tunnel wind speed: Reduced tunnel speed leads to increased angle of attack on the fan blades for a constant rotational rate. Figure 7.1 shows the noise versus mass flow rate and the stalled and attached flow noise spectra from this study. Two notable features are apparent. The first is the rapid increase in noise as the flow on the fan blades presumably begins to separate; this occurs at the lowest mass flow rates shown. Overall noise levels increase by 10 dB for a change in mass flow rate of ~20%. The other is the spectral effect on the noise. Stalled flow pushes the peak spectral content of the noise to significantly lower frequencies, likely owing to the larger scale turbulence in the separated flow region.

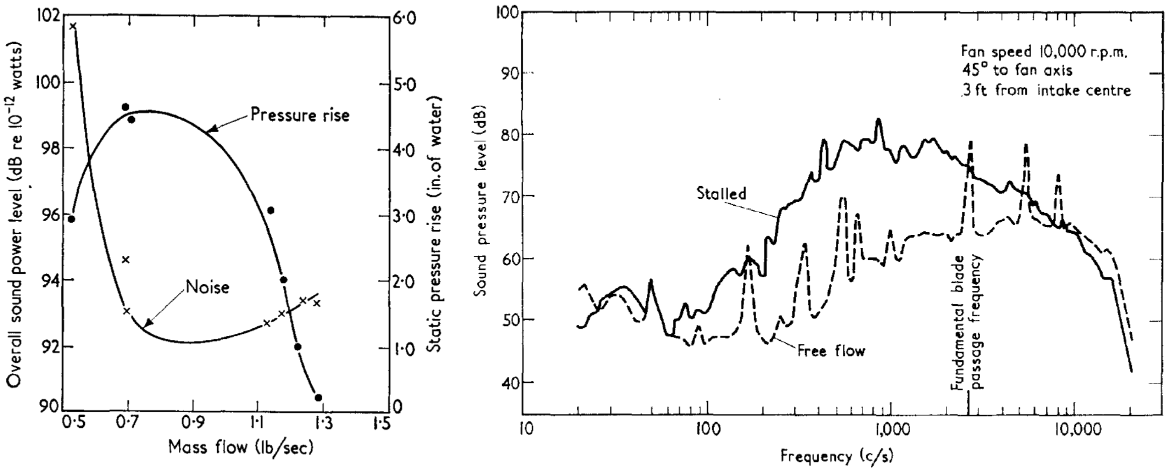

Figure 7.1: Noise levels versus mass flow rate for a ducted axial fan with a constant rotational speed (left) and the spectral difference between attached flow and stalled flow noise (right). Figure credit to Sharland et al. [75].

Research conducted since the work of Sharland [75] have typically corroborated the qualitative result of noise increasing rapidly after the onset of flow separation [15, 54, 50], though the level of increase varies from ∼3 dB [15] to ∼30 dB [54] dependent on the specific model, depth of stall, and testing methods. Maruta et al. [52], contrarily, show a *decrease* in noise with angle of attack for a flat plate airfoil in a wind tunnel. Angles of attack tested are in particularly coarse increments—values of 0°, 30°, 60°, and 90°, where 30° can already be expected to beyond the stall angle of a flat plate. This result may be due to the competing effect of directivity, as the spectra shown are for a microphone located in a direction perpendicular to the mean flow. Maruta et al. [52] also perform a cross-correlation study of hydrodynamic pressure fluctuations in the wake of the airfoil with acoustic pressure fluctuations in the far field. Results show that the cross correlation is largest for near field fluctuations very close to the airfoil, indicating that the noise is due to surface dipole radiation, rather than free-field quadrupole sources. This is the expected result for low Mach number flows, as discussed in Section 2.1 [26].

A more recent study by Moreau et al. [54] investigated several airfoil shapes in aeroacoustic wind tunnel tests for high angles of attack. The thickest airfoil tested is a NACA0012. Measurements are made with single microphones in a direction perpendicular to the flow, but a strong signal to noise ratio was generally achieved, and data is rejected when the SNR is below 2 dB. Separated flow is detected using total static pressure measurements in the wake of the airfoil near its trailing edge, clearly showing the onset of a recirculation region. Results show what Moreau delineates as two flow regimes beyond the onset of flow separation, referred to as “light stall” and “deep stall”. The former occurs above geometric angles of attack above about 15° and is characterized acoustically by a 10 to 20 dB broadband increase in noise over about a decade of frequencies. The latter occurs at geometric angles of attack of about 25° and is characterized by strong tonal noise of about 30 dB above attached flow levels. The broadband noise for deep stall is lower than that of light stall. Moreau attributes the tonal noise to large scale vortex shedding, though unsteady wake measurements are not made. Static pressure measurements on the surface of the NACA0012 show a recirculation region near the leading edge for stalled flow, which is expected for thin airfoils [52, 54]. This is contrary to the thick airfoils used in wind turbines for structural reasons, which typically show recirculation regions near the trailing edge, as will be shown in Section 7.2.2.

The purpose of the study described in this chapter is to determine the acoustic effects of flow separation and aerodynamic stalling on a full scale turbine by intentionally inducing separated flow on the prototype SWP-2.3-108 in Boulder, Colorado. The study will answer the questions as to how stall noise behaves both for thick airfoils and for a full scale turbine, neither of which have been addressed in the literature. Separated flow is induced by adjusting the turbine’s control parameters in order to slow the rotor and increase the operating angle of attack beyond the stall angle. Stalled conditions are detected using the static pressure taps at the 33 m, 44 m, and 51 m radial stations (54 m rotor radius) on the instrumented blade. A method is developed for detecting separated flow using the measured pressure coefficients from only two of the pressure taps at each station—one near the trailing edge and one at about 50% chord. The acoustic signature is then measured using all twelve ground ring microphones as described in Chapter 3, showing that stalled flow increases noise across all frequencies by at least 7 dB and up to 13 dB above normal operation. Overall levels increase by at least 10 dBA. Results also show that the stall noise directivity does not follow the expected compact dipole pattern—even as low as 100 Hz. The driving physical mechanisms for this unexpected noise directivity are not yet fully clear.

7.2 Experimental Approach

This section will outline the experimental methods used to determine the acoustic effects of stall, including the instrumentation, the method of deliberately inducing blade stall, and a method of using the static pressure measurements on one of the blades in order to detect stalled conditions. Finally, the signal processing codes are outlined and discussed. The research is conducted on the Boulder turbine and acoustic signal processing is the same as for the turbulent inflow noise study. The facility, instrumentation, and signal processing methods are detailed in Chapter 3.

7.2.1 Inducing Stall

In order to determine the acoustic effects of flow separation and aerodynamic stalling, the controller parameters of the turbine are modified such that the operating angle of attack increases and stall flow is achieved. This experimental process allows for controlled investigation of the acoustic effects in that the turbine may be readily switched between stalled and attached operation. Three settings are cycled through during experimentation, with 10 minutes at a time spent at each setting:

(1) **Normal Operation** Max RPM: Ω_0; Max Electrical Power: P_0

This is the baseline measurement. It gives a reference noise level as well as a means to compare with prior measurements.

(2) **Low-speed, Stalled Flow** Max RPM: $0.63\times\Omega_0$; Max Power: $0.63\times P_0$

This setting pushes the turbine into high operating angles of attack and stall. Pressure tap data shows that stall typically occurs across the entire noise generating portion of the blade (see Section 7.2.2).

(3) **Low-speed, Attached Flow** Max RPM: $0.63\times\Omega_0$; Max Power: $0.26\times P_0$

By reducing the maximum power demanded from the turbine, the controller pitches the blades out, reducing operating angles of attack and inducing attached flow. This gives a comparison of noise for attached flow and stalled flow at the same wind speed.

All other controller parameters were left unchanged during this test. Setting 2 induces stalled flow for sufficiently high wind speeds by virtue of the vector addition of the wind vector and the blade sectional velocity, often referred to as the "inflow triangle". Figure 7.2 depicts the inflow triangle for each of the settings listed above and illustrates how the reduced rotor rate increases the operating angle of attack. Each setting was designed using the NREL blade-element-momentum (BEM) code WTPerf [19] in order to determine how much power the turbine could actually make at a given wind speed and rotor rate. For Setting 2 the max power was set well above this limit to avoid pitching out, and for Setting 3 it was set below this limit in order to promote pitching out. Note, that while sufficiently high wind speeds are required to achieve stall, wind speeds can be too high causing the blades to pitch out for Setting 2 and re-attaching the flow. The nominal wind speed regime for the test was between approximately 9 and 12 m/s. Setting 1 was used for

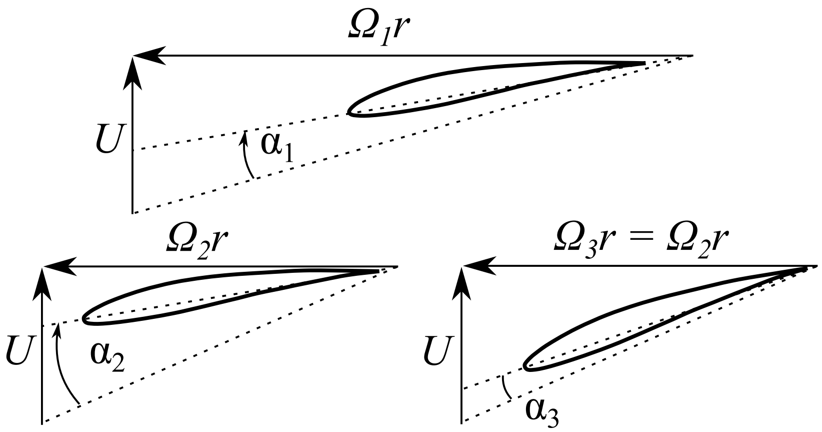

Figure 7.2: Inflow triangle depiction of each of the three controller settings implemented during stall testing. The parameter α shown is the sectional angle of attack. The angle of the blade section with respect to the rotor plane—the Ωr direction—is the sum of the blade pitch angle and the geometric twist of the blade at that station. The subscript numbers correspond to the setting numbers in the list above.

comparison of measurements with the large volume of normal operation data taken three months prior to this test. Analysis of similar data between the two data sets—matched wind speed, rotor RPM, and turbulence intensity—shows that the data sets agree to within 1.4 dB and with a mean error of 0.5 dB. This level of agreement allows for direct comparison between the two datasets, albeit with a certain degree of uncertainty due to systematic error. As such, when comparisons are made to this volume of data an error margin of ±0.5 dB plus the standard error of the measurement are included.

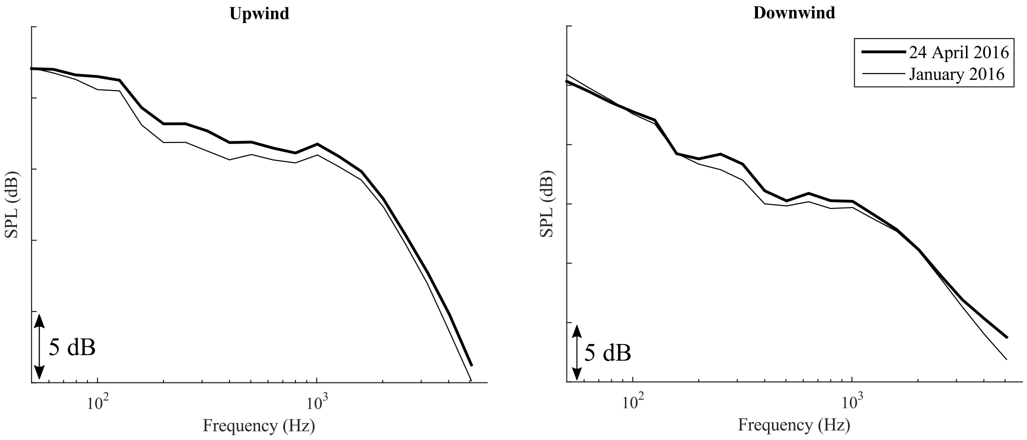

Figure 7.3: Comparison of data gathered during the extended data acquisition campaign, primarily in January 2015, to data gathered during the stall test in April 2015. Data is for maximum rotor RPM, wind speeds of 10.2 m/s, and equivalent turbulence intensities between 0.12 and 0.17. Both spectra consist of at least 20 constituent spectra.

7.2.2 Detecting and Quantifying Stall

Blade C of the Boulder turbine is outfitted with static pressure ports at the 33 m, 44 m, and 51 m spanwise stations. A method has been developed for using the measured pressure distribution for detecting aerodynamic flow separation and stall, which is implemented in this acoustic analysis and is detailed here. Separation occurs at high angles of attack due to a strong adverse pressure gradient causing flow deceleration and reversal. For the thick airfoils used in modern wind turbines, flow reversal occurs towards the trailing edge on the suction side of the blade. A recirculation region then arises, which is readily observable in the measured pressure distribution, as is shown in Figure 7.4. The recirculation region is the region of nearly constant pressure coefficient in the suction side stalled data.

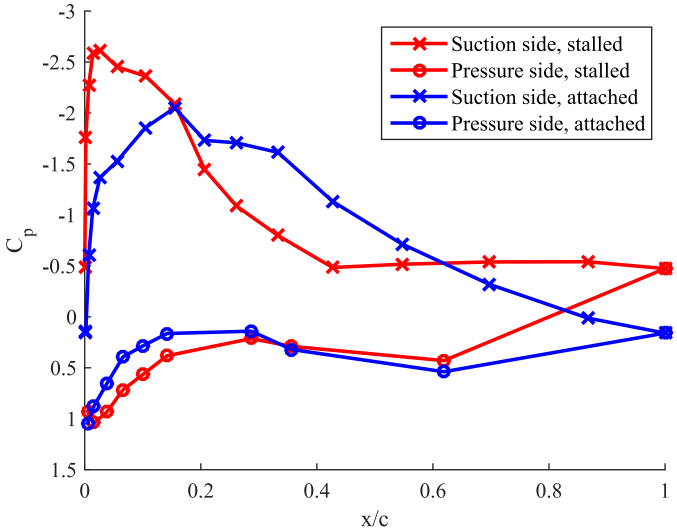

Figure 7.4: Pressure coefficient distributions for stalled and attached flow conditions taken at the 44 m radial station. Data is from the stall test conducted on the Boulder turbine on 28 January 2014. The two measurements are averaged over 20-second segments.

Now, the reason that Figure 7.4 shows the pressure distributions taken during the 28 January 2014 stall test—when acoustic data was not gathered—instead of the more recent stall test on 24 April 2015 is that the pressure taps are subject to clogging, and numerous pressure taps had gone out of commission by the time of the later, stall noise testing (and, in fact, several before the earlier test). That said, the method of detecting separation and stall to be used in this study requires only two pressure taps, one on the suction side near the trailing edge and one closer to mid-chord. Inspection of the two pressure distributions in Figure 7.4 shows that the change in C_p between about mid-chord and the trailing edge is quite indicative of whether a recirculation region exists. Specifically, the quantity ΔC_p defined by Equation 7.1 is used as the indicator for flow separation.

$$\Delta C_p = C_{p,56} - C_{p,99} \tag{7.1}$$

Here, $C_{p,56}$ and $C_{p,99}$ are the suction side pressure coefficients at 56% and 99% chord, respectively.

Figure 7.5 shows a C_L-α curve for the 44 m spanwise station, where C_L is the lift coefficient calculated by integrating the pressure distribution with respect to the chordwise and cross-chord directions, with the lift being the sum of the components in the cross-stream direction. The angle of attack is calculated geometrically using the wind speed measured at hub height at the MET tower and an induction factor of 0.33. The figure shows that two pressure taps are sufficient to quantitatively characterize the aerodynamic state of the flow around the blade: ΔC_p rapidly drops from above 0.7 to below 0.3 for angles of attack beyond the angle where separation occurs, as indicated by the highly non-linear lift curve. This makes it possible to analyze the stall noise test data using a direct assessment of the flow conditions for each acoustic measurement, rather than by estimating the angle of attack and assuming the aerodynamic state. This becomes important due to the relatively limited amount of data that was captured, as will be shown later.

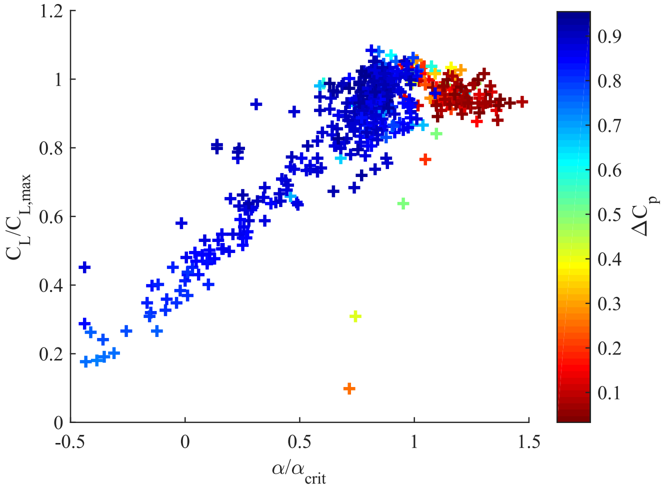

Figure 7.5: Lift coefficient C_L versus angle of attack α, colored by ΔC_p. ΔC_p is calculated as the difference between the trailing edge pressure tap and the tap at 56% chord on the suction side. Data is from the stall test conducted on the Boulder turbine on 28 January 2014. Each point represents fifteen seconds of experimental data.

Figure 7.6 shows ΔC_p against estimated angle of attack for the three stations spanwise stations for both the January 2014 test and the April 2015 test. The aerodynamic data matches quite well at both the 33 m and 44 m stations, though the measurements at the 51 m station suggest that the blade was stalling at lower angles of attack during the earlier test than during the latter. The pressure data also indicates that the flow in the latter test did not reach the level of separation at the 51 m station that was achieved during the earlier test, namely where ΔC_p bottoms out below about 0.2. Nonetheless, the level of agreement between the two data sets indicates that the measurements of these two pressure taps should be sufficient to detect flow separation.

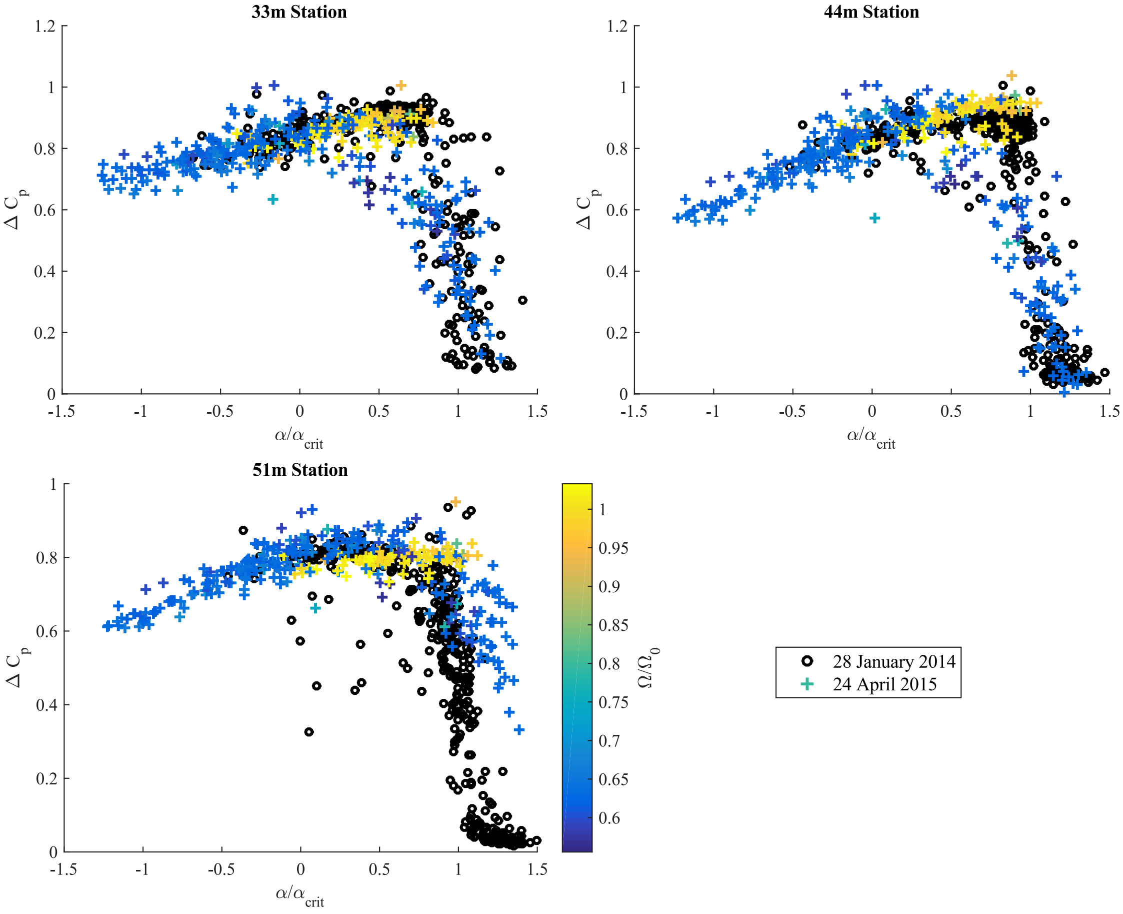

Figure 7.6: Stall number ΔC_p versus angle of attack α at each spanwise station. Each data point represents fifteen seconds of experimental data. Black data points are from the January 2014 test, and colored data points are from the April 2015 test.

7.2.3 Binning by Aerodynamic State

The measured ΔC_p, along with the estimated angle of attack, provide a fairly robust method of filtering for stalled conditions. As a first study in the next section, the data is grouped into three bins: small-α attached, large-α attached, and large-α fully stalled. The filtering criterion for each bin is based on the rotor rate, the angle of attack estimation for each station, and the ΔC_p at each station. All three are at the reduced rotor RPM of $0.63 \times \Omega_0$, and the max-RPM (Ω_0) data is used simply in comparison to previously acquired data under normal turbine operation. Note that these bins do not correspond directly to the controller settings described above: Setting 3 has been broken into two groups because of the large amount of angle-of-attack variation within it. The specific filtering criteria are given in the list below along with the number of 15-second measurements matching each. Note that separated flow is readily filtered for 33 m radial location and outboard, but inboard stalling can still occur, as is discussed further below. Wind speeds are limited to between 8 and 12.5 m/s based on nacelle anemometer data.

(1) **Small-α, Attached:** $-0.3 < \alpha/\alpha_{\text{crit}} < 0.1$; $\Delta C_p > 0.6$; 31 measurements

(2) **Large-α, Attached:** $\alpha/\alpha_{\text{crit}} > 0.6$; $\Delta C_p > 0.6$; 12 measurements

(3) **Fully Stalled:** $\alpha/\alpha_{\text{crit}} > 0.6$; $\Delta C_p < 0.4$; 56 measurements

7.3 Results

This section outlines the acoustic measurement results for the stall noise testing. Third-octave levels are first given for each of the three aerodynamic bins described in Section 7.2.3. The directivity of stall noise is then analyzed.

7.3.1 Third-octave Spectra and Overall Levels

Figure 7.7 shows the third octave levels measured in the upwind and downwind direction for the three aerodynamic states described in Section 7.2.3. All three sets of data shown are at the reduced rotor RPM, so the effects are almost entirely due to difference in angle of attack and aerodynamic state. Data is corrected for background levels, and data is omitted for frequencies at which the mean SNR drops below 3 dB; it is evident that background noise becomes an issue for small α at the low rotor rate due to the significantly reduced turbine acoustic signal with the same background noise levels. Normal operation data is also included for the same rotor rate, i.e. at a wind speed of about 6 m/s, such that the local inflow speed along the blade is approximately matched. The turbulence dissipation rate is matched such that the TI noise should be approximately equal. Error bars are included in order to reflect that there was about three months between these sets of measurements (see Section 7.2.1). Comparison between stall and normal operation measured levels provides insight into the expected increase in noise if a uniform, 4 m/s gust pushes the turbine into stall—the noise increase before the turbine controller has time to react. The other two bins then show give the expected noise levels as the turbine pitches to lower angles of attack; this hypothetical sequence provides some intuitive context for these four spectra. It is noted that the low-α stall-test levels are slightly higher than the normal operation data at mid- and very high frequencies, despite the low outboard angle of attack. Several factors likely contribute to this behavior, including the slightly increased inflow speeds, increased pressure side boundary layer turbulence, and perhaps even separation noise inboard, as is discussed further below.

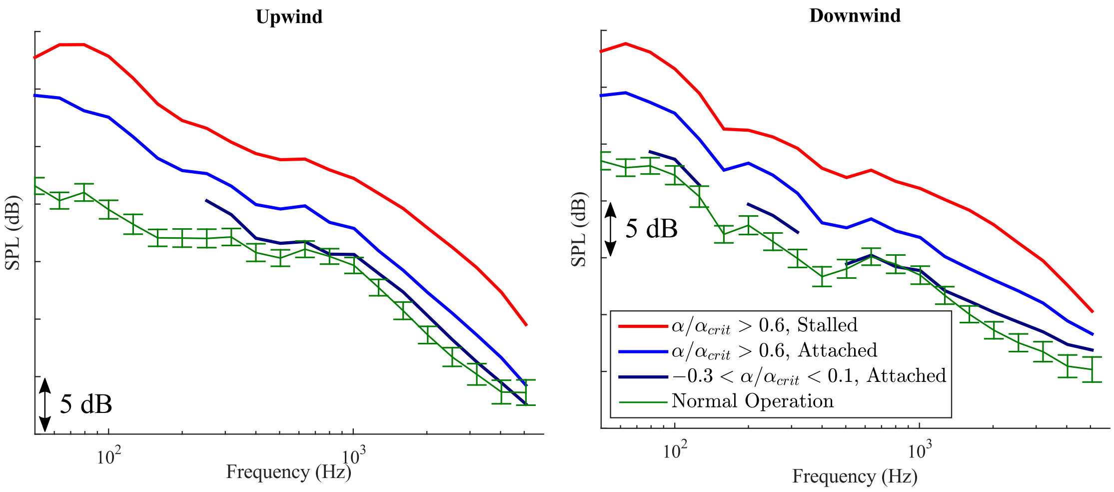

Figure 7.7: Mean unweighted third-octave levels for the three aerodynamic bins described in Section 7.2.3. All rotor RPMs are approximately equal and all spectra are background corrected. Normal operation data is gathered at $U = 5.9$ m/s to achieve the same rotor RPM; the mean approximate angle of attack for this data is $\alpha_{44m}/\alpha_{\text{crit}} = 0.61$.

Results show that the increase in spectral levels from normal operation to deep stall is broadband, between 8 and 13 dB, with the strongest increase in the low frequencies. The increase in the integrated A-weighted levels between attached and stalled flow is 12.0 dBA in the upwind direction and 10.6 dBA in the downwind direction. The noise increase at low frequencies is particularly notable, because under normal operation conditions the low frequency noise is dominated by turbulent inflow noise. This is shown for the maximum rotor RPM data in Chapter 5, and a similar analysis suggests that TI noise dominates below about 150 Hz for the reduced RPM data (Figure 7.9). Since TI noise is relatively independent of angle of attack [36, 58], the TI noise levels contributing to the four spectra of Figure 7.7 can be expected to remain approximately at the normal operation level—the level observed below 150 Hz. This suggests that the TI noise becomes dominated for the high-α cases by between 5 and 13 dB. Several effects are at play here, so careful consideration must be made. Namely, trailing edge noise increases with angle of attack even before separation occurs [15], which makes definitively separating the noise increase due simply to angle of attack effects on TE noise from the noise increase due to flow separation somewhat difficult. However,

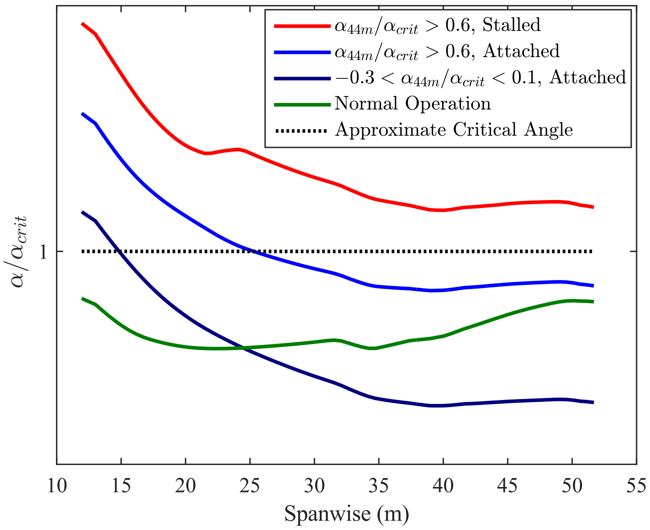

Figure 7.8: Approximate angle of attack versus radial location for the four aerodynamic bins used in Figure 7.7. Operational conditions used in calculation—pitch, RPM, wind speed—are the mean values for each respective set of data. The critical angle is taken from pressure tap data (see Figure 7.5)

the amount by which the noise is increased is far greater than can be expected for normal trailing edge noise. TE noise increases by approximately 0.3 dB/degree based on the semi-empirical model of Brooks et al. [15], so this noise mechanism alone can be expected to increase by less than 3 dB between normal operation and stalled operation, indicating that separation and stall noise causes the majority of the observed 8-13 dB increase.

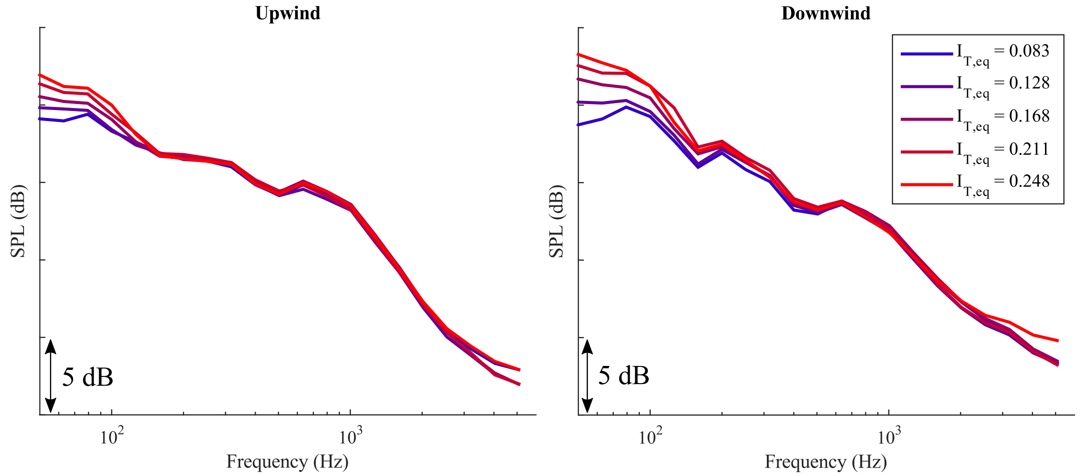

Figure 7.9: Third-octave spectra for varying turbulence intensities at reduced rotor RPM. Each spectra is an energy average of at least six constituent spectra.

The integrated difference between the attached and stalled high-α data—i.e. just before stall and just after stall—is approximately 4 dBA both upwind and downwind. However, the relatively high noise level for the high-α attached flow is suspected to be due in part to inboard flow separation. As discussed in Section 7.2.2, the data is filtered to ensure that the flow is either stalled or attached at the radial locations where pressure data is available. The angle of attack is higher inboard of the pressure taps for these operational conditions. An approximation of the angle of attack as a function of radial location for the four sets of mean operating conditions corresponding to the four spectra is shown in Figure 7.8. The angle of attack α in this case is calculated from a Siemens internal blade element model code quite similar to WTPerf [19] with estimated blade-strain deformation included. The code calculates the induction for each radial position as a function of the aerodynamic forces at that blade section, offering a more accurate estimate of the spanwise distribution of α than by assuming a constant induction. The distribution for the high-α, attached flow shows that while the 33 m station is ensured via pressure data to be attached, the increased angles of attack inboard are likely to be causing flow separation and increased noise levels. This could perhaps best be investigated by distributed-source acoustic modeling, which would be a practical next step in this investigation.

7.3.2 Stall Noise Directivity

An analysis of the turbine noise directivity is conducted in order to gain further insight into the stall noise mechanism and to potentially improve modeling capabilities. Turbulent inflow noise is shown in Chapters 5 and 6 to be dominant for frequencies below about 400 Hz for normal operating conditions. However, based on the third-octave analysis in the previous section, it appears that the stall noise becomes dominant at low frequencies when it arises. The directivity of the 100 Hz spectral hump is analyzed here. The 100 Hz attached-flow directivity is based on normal operation data at the same rotor RPM, rather than the low-α data taken during the the presently discussed test. This is because the signal to noise ratio of the low-α, attached data of this test is too low; the background noise is high because of the wind speed but the turbine noise is low because of the reduced RPM. Results show that for attached flow the noise is higher in the downwind direction by 1.5 dB, while fully stalled directivity is higher in the *upwind* direction by 1.2 dB. The former is consistent with the directivity of turbulent inflow noise radiated from the leading edge and can be predicted either by a point source model (Section 5.5) or a distributed source model (Section 6.3.5); a point source model with a constant radial location of 79% span is included here. The high frequency leading edge directivity model agrees fairly well with the measured directivity in its difference between upwind and downwind noise levels and the shape of its upwind and downwind lobes. Similar agreement is found at any rotor rate, including the normal operation data at max-RPM gathered during this test—this is the expected result for turbulent inflow noise.

The stall noise directivity is more elusive, however. Stall noise is often modeled as a compact dipole [15, 57] due to its low frequency noise contribution. However, it is clear from Figure 7.10

that the noise is decidedly inconsistent with a dipole model. Agreement with the dipole model is not improved significantly regardless of source location, which indicates that the integrated noise from a distributed dipole source model is also highly unlikely to predict this pattern. The observed upwind preference is more consistent with a high frequency trailing edge noise directivity model, but agreement is not good insofar as the shape of the downwind lobe. The exact mechanisms driving this directivity are currently unclear, but the disagreement with dipole radiation in itself is considered scientifically interesting. Oerlemans [60] showed that a similar turbine had a noise emission directivity pattern consistent with the HF trailing edge noise pattern down to 325 Hz, so the result is not entirely unexpected but is inconsistent with theory—the turbine noise code discussed in Chapter 6 predicts that the exact directivity model is approximately dipole-like up to at least 250 Hz. Considering the agreement of the measured TI noise turbine directivity with the theoretical HF *leading edge* noise model—even as low as 125 Hz (Section 6.3.5)—this result seems to indicate that the directivity of airfoil aeroacoustic noise may generally have preference opposing the edge from which it is emitted, even at very low frequencies—i.e. the true radiation pattern is approximately cardioid-like in the plane perpendicular to the spanwise direction. Neither low frequency stall noise nor TI noise radiate in the expected compact dipole pattern; the disagreement with theory is much more evident in the case of separation noise, as can be seen in Figure 7.10. This finding in itself may warrant further investigation but at this time is not fully understood.

7.4 Conclusions

A stall noise test was conducted on the Boulder turbine in order to assess the effect of flow separation on wind turbine noise. The turbine blades were pushed to high angles of attack by slowing down the rotor to increase the operating angle of attack. Static surface pressure data was acquired at the 33 m, 44 m, and 51 m spanwise positions along one blade, which was used to detect the presence of a separation region. Results show that noise increases by between 8 and 13 dB across all frequencies when comparing normal operation noise levels to stalled noise levels at the same rotor RPM. A difference in integrated noise levels of about 4 dBA is observed between angles

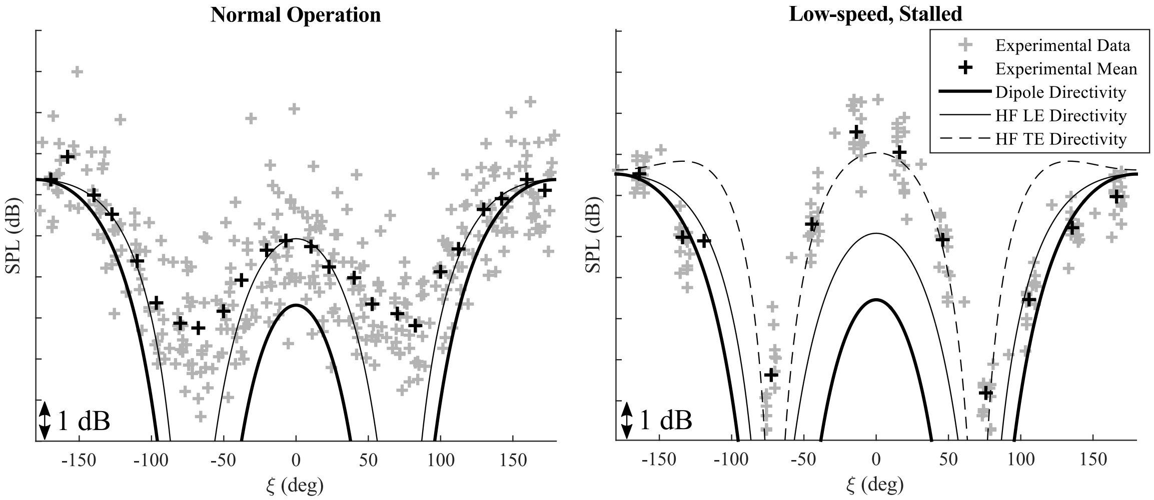

Figure 7.10: Directivity of the third-octave band centered at 100 Hz for normal operation at U = 6.2 m/s (left) and for the deep stall data (right); rotor RPMs are approximately equal. The predicted directivity is based on a point source model directivity model where all point sources are located at the approximate source location of 79% span [16]. Predictions are normalized to the measured level in the downwind direction, i.e. at a viewing angle of $\xi = -180°$.

just before the onset of separation and a few degrees beyond separation, though it is expected that separation inboard of the pressure sensors is contributing to this reduced acoustic effect. The increase in integrated noise levels between *normal operation* and stall is shown to be about 12 dBA in the upwind direction and 10.6 dBA in the downwind direction. The stall noise appears to be generally broadband with a spectral hump around 100 Hz, and is shown to be stronger than turbulent inflow noise at low frequencies. This assertion is based on the drastic increase in noise at low frequencies, whereas turbulent inflow noise is not significantly affected by angle of attack. The turbine noise directivity pattern changes character significantly for separated flow and is shown to be quite inconsistent with the expected dipole radiation pattern. The measured directivity appears to be closer to the high-frequency asymptote of the exact theoretical directivity pattern, but the mechanisms for this observed directivity are currently unknown.

Chapter 8

Conclusions

An investigation has been conducted into two wind turbine acoustic noise generation mechanisms that contribute to variability of noise emission in field-deployed turbines. The objective of this dissertation is to mitigate issues pertaining to unexpected or not fully understood acoustic effects that arise due to the vastly broad operational conditions wind turbines encounter. These effects are referred to as "variability parameters", as they are caused by differences in operational conditions such as atmospheric turbulence, wind shear, and wind veer. Noise variability may also arise due to turbine-to-turbine variation, e.g. blade manufacturing variability, though this dissertation focuses on the former—the variability in noise that can arise even for identical turbines. The two parameters investigated are turbulent inflow noise and noise due to flow separation. By thorough experimental characterization of these two mechanisms and comparison to expectations based on literature review and simulation, the understanding of this variability behavior is enhanced such that its detrimental effects—curtailed-power operation and negatively impacted public perception—can be mitigated by more informed wind turbine design and noise modeling. The conclusions drawn from this dissertation may be summarized as follows.

Wind turbine turbulent inflow noise results from small scale turbulent fluctuations interacting with the leading edge of wind turbine blades. As this noise mechanism is highly dependent on turbulence conditions—which are driven by surface roughness and atmospheric stability—turbulent inflow noise will naturally vary from location to location and throughout a given turbine's operational lifetime. This parameter is investigated by analysis of an extensive experimental dataset comprising thorough acoustic and atmospheric measurements taken at a full-scale wind turbine facility. Acoustic measurements consist of twelve calibrated, precision microphones in a one rotor radius ring about the turbine. A method is developed for estimating both the turbulence intensity and turbulence dissipation rate based on measured vibrations in each of the blades. This provides an in-situ measurement of the turbulence and is shown to significantly improve the fidelity of the results. Analysis generally shows that turbulent inflow noise affects the low frequency noise emission, below a few hundred Hz, confirming what has been predicted by several noise models in the literature. The increase in low frequency noise is approximately 6 dB between the minimum and maximum turbulence observed at this test site. Measured noise is reduced drastically in the plane of the rotor, similar to trailing edge noise. Finally, significant scrutiny is placed upon the results in order to show that the increase in noise with turbulence intensity is due to turbulent inflow noise. Wind noise increase on the microphones is ruled out by a simple signal to noise ratio argument, where the mean wind noise is shown to be insufficient to potentially cause significant effects. Increases in trailing edge noise and separation noise due to variations in angle of attack are also ruled out by a rudimentary statistical analysis of the range of angles of attack that can be expected for a given turbulence level. This analysis leads to the secondary conclusion that the primary acoustic impact of turbulence arises from the interaction of small scale turbulence structures with the leading edge causing surface pressure fluctuations, and *not* due to angle of attack variations. Large, coherent turbulent structures may be an item for future investigation, however, as they are more likely to result in systematic aerodynamic stalling.

The results are compared to the predictions of a commonly used wind turbine noise prediction model. The model is modified in two particular ways. The first is that the noise is predicted based on the turbulence dissipation rate instead of the combination of turbulence intensity and integral length scale, i.e. an assumed Kolmogorov turbulence spectrum instead of a von Kármán spectrum—the latter being the assumption of prior research. This modification is due simply to the scale of typical atmospheric turbulence, for which the integral length scale is large enough to have negligible effect on acoustic frequencies above 20Hz. In other words, the two spectra are identical within the frequency range of interest, so the integral length scale is both irrelevant and inconvenient due to the long period over which it must be calculated. It is important to note that this modification is not a change to the *acoustic* model whatsoever, only the turbulence model; the modification is simply for convenience in making predictions for short periods of time. The second modification is the use of the high frequency, cardiodal directivity pattern, instead of the dipole-like pattern used in previous models. This is shown to significantly improve agreement with experimental observations. Comparisons are made based on the third-octave spectral levels, turbine noise directivity, scaling of noise with turbulence dissipation rate, and scaling of noise with blade tip speed. Perhaps the preeminent result of this study is that the model developed by Guidati and Moriarty to account for finite thickness airfoils provides appreciably improved absolute level prediction over the flat plate model of Amiet. Agreement is particularly good between about 100-300 Hz, though significant deviation occurs particularly in the upwind direction for frequencies below 100 Hz.

Finally, noise due to aerodynamic flow separation on a wind turbine blade is investigated by controlled experimentation. The test turbine's blades are deliberately pushed into higher operating angles of attack by reduced rotor RPM. The angle of attack is then further modified using blade pitch actuation such that the turbine is periodically shifted from stalled flow to attached flow operation. Flow separation is detected using surface static pressure ports at three radial stations along one of the blades. Acoustic data is gathered using the same ground-ring system as in the turbulent inflow noise study such that the effects of flow separation on noise directivity can be assessed. Measured results are also compared to measurements made for normal operation at the same rotor RPM, i.e. at a lower wind speed but with closely match local inflow speeds along the blade. This comparison gives insight into the hypothetical case where a uniform gust—from 6 m/s to 10m/s—drives the entire rotor into stall. Results show that the increase in overall noise from normal operation to fully stalled flow is over 10 dBA, with the strongest increase at low frequencies. Noise is appreciably reduced at higher pitch angles (lower angles of attack) for the same wind speed. This is postulated to be due to two additive effects: reduced boundary layer turbulence as the angle of attack decreases, and the reduced fraction of the blade that is operating in stall. It is quite certain, however, that flow over the entire blade is attached for normal operation and fully stalled for the highest angle of attack setting, which is why the comparison of these two operational bins is particularly clear and insightful. A significant effect is also observed on the noise directivity when the flow separates. Specifically, as separated flow noise begins to dominate turbulent inflow noise low frequencies, the directivity shifts from a downwind preference to an upwind preference. Though this shift in directivity is not fully understood, it is of particular note that the directivity is clearly inconsistent with the dipole radiation pattern typically assumed for separation and stall noise.

With regard to the overarching theme of this dissertation, some closing remarks should be made on the variability impact of these two parameters. Turbulent inflow noise can intuitively be expected to be problematic at high turbulence sites and to vary significantly for sites where turbulence is inconsistent, such as at the NWTC. The effect on near-field, A-weighted levels is perhaps negligible aside from extreme turbulence variation—only about 0.5 dBA variability was observed at the ground ring microphones for variation in turbulence intensities between 0.09 and 0.24. The effect is undoubtedly higher at larger distances, however, being that the low frequency noise propagates more efficiently. One notable implication is that, while measurements made in accordance with IEC Standard 61400-11 accurately reflect the small effect of turbulence near the turbine, neighbors at larger distances may observe a more significant impact of turbulence. As stated in Chapter 1, this dissertation is not intended to make any argument about the sufficiency of IEC Standard 61400-11; the standard simply gives useful context for the implications of noise variability.

In practice, separation noise is unlikely to occur in the manner that it has been induced in this research. That is, stall over the entire rotor is unlikely, or at least unlikely to persist for long before the turbine controller reacts. As such, the results of this study should be used to assess expectations for dynamic-stall and thump noise. Instead of all three blades operating with separated flow simultaneously, a single blade will enter and exit regions of the rotor plane where stall occurs due to wind shear, veer, yaw error, or perhaps coherent turbulence structures. If the entire noise-generating portion of the blade enters stall, the spectra for that blade can be expected to increase by the same spectral difference that was observed for the entire rotor in this dissertation. This means that the 10 dBA increase for the rotor translates to a roughly 6 dBA thump—a sudden increase in noise when a single blade completely stalls. Some approximate fraction of this thump amplitude can also of course be assumed if a certain fraction of the blade stalls, rather than its entire length. This can be considered the most likely variability impact of flow separation noise.

Bibliography

[1] John J Adamczyk. Passage of a swept airfoil through an oblique gust. Journal of Aircraft, 11(5):281–287, 1974.

[2] Matthew L Aitken, Robert M Banta, Yelena L Pichugina, and Julie K Lundquist. Quantifying wind turbine wake characteristics from scanning remote sensor data. Journal of Atmospheric and Oceanic Technology, 31(4):765–787, 2014.

[3] Roy K Amiet. Compressibility effects in unsteady thin-airfoil theory. AIAA Journal, 12(2):252–255, 1974.

[4] Roy K Amiet. Acoustic radiation from an airfoil in a turbulent stream. Journal of Sound and vibration, 41(4):407–420, 1975.

[5] Roy K Amiet. Correction of open jet wind tunnel measurements for shear layer refraction. In AIAA Conference on the Exploration of the Outer Planets, volume 1, 1975.

[6] Roy K Amiet. High frequency thin-airfoil theory for subsonic flow. AIAA journal, 14(8):1076–1082, 1976.

[7] Roy K Amiet. Noise due to turbulent flow past a trailing edge. Journal of Sound and Vibration, 47(3):387–393, 1976.

[8] Franck Bertagnolio, Andreas Fischer, and Wei Jun Zhu. Tuning of turbulent boundary layer anisotropy for improved surface pressure and trailing-edge noise modeling. Journal of Sound and Vibration, 333(3):991–1010, 2014.

[9] Franck Bertagnolio, Helge Aa Madsen, Christian Bak, Niels Troldborg, and Andreas Fischer. Aerodynamic noise characterization of a full-scale wind turbine through high-frequency surface pressure measurements. International Journal of Aeroacoustics, 14(5-6):729–766, 2015.

[10] David T Blackstock. Fundamentals of physical acoustics. John Wiley & Sons, 2000.

[11] William K Blake. Mechanics of flow-induced sound and vibration: complex flow-structure interactions, volume 2. Academic Press, 1986.

[12] Dick Bowdler. Amplitude modulation of wind turbine noise: a review of the evidence. Institute of Acoustics Bulletin, 33(4):31–41, 2008.

[13] Thomas F Brooks and Casey L Burley. Rotor broadband noise prediction with comparison to model data. AIAA paper, 2210:2001, 2001.

[14] Thomas F Brooks and TH Hodgson. Trailing edge noise prediction from measured surface pressures. Journal of Sound and Vibration, 78(1):69–117, 1981.

[15] Thomas F Brooks, D Stuart Pope, and Michael A Marcolini. Airfoil self-noise and prediction, volume 1218. National Aeronautics and Space Administration, Office of Management, Scientific and Technical Information Division, 1989.

[16] Steven Buck, Stefan Oerlemans, and Scott Palo. Experimental characterization of turbulent inflow noise on a full-scale wind turbine. Journal of Sound and Vibration, 385:219–238, 2016.

[17] Steven Buck, Stefan Oerlemans, and Scott Palo. Experimental validation of a wind turbine turbulent inflow noise prediction code. In 22nd AIAA/CEAS Aeroacoustics Conference, page 2953, 2016.

[18] Steven Buck, Scott Palo, Pat Moriarty, and Jason Roadman. Acoustic array development for wind turbine noise characterization. NREL Technical Report, TP 5000-60457, 2013.

[19] Marshall L Buhl. Wt_perf users guide. National Wind Technology Center, National Renewable Energy Laboratory, Golden, CO, 2004.

[20] Tony Burton, David Sharpe, Nick Jenkins, and Ervin Bossanyi. Wind energy handbook. John Wiley & Sons, 2001.

[21] FH Champagne. The fine-scale structure of the turbulent velocity field. Journal of Fluid Mechanics, 86(01):67–108, 1978.

[22] Andrew Clifton, Scott Schreck, George Scott, Neil Kelley, and Julie K Lundquist. Turbine inflow characterization at the national wind technology center. Journal of Solar Energy Engineering, 135(3):031017, 2013.

[23] International Electrotechnical Commission. Wind Turbine Generator Systems Part 11: Acoustic Noise Measurement Techniques. IEC Standard 61400-11, 2000.

[24] International Electrotechnical Commission. Wind Turbine Generator Systems Part 12: Power Performance Measurements of Electricity Producing Wind Turbines. IEC Standard 61400-12, 2000.

[25] DG Crighton. Scattering and diffraction of sound by moving bodies. Journal of Fluid Mechanics, 72(02):209–227, 1975.

[26] N Curle. The influence of solid boundaries upon aerodynamic sound. Proceedings of the Royal Society of London. Series A. Mathematical and Physical Sciences, 231(1187):505–514, 1955.

[27] Carlo Di Napoli. Long distance amplitude modulation of wind turbine noise. In Fourth International Meeting on Wind Turbine Noise, 2011.

[28] Oriol Ferret Gasch. Assessment, Development, and Validation of Wind Turbine Rotor Noise Prediction Codes. Master's thesis, Delft University of Technology, the Netherlands, 2014.

[29] Fergus R Fricke and DC Stevenson. Pressure fluctuations in a separated flow region. The Journal of the Acoustical Society of America, 44(5):1189–1200, 1968.

[30] FR Fricke. Pressure fluctuations in separated flows. Journal of Sound and Vibration, 17(1):113–123, 1971.

[31] Peter Fuglsang and Helge Aagaard Madsen. Implementation and verification of an aeroacoustic noise prediction model for wind turbines. Riso National Laboratory, 1996.

[32] J Gershfeld. Leading edge noise from thick airfoils in turbulent flows. Journal of the Acoustical Soc. Am, 116(3), 2004.

[33] SAL Glegg, SM Baxter, and AG Glendinning. The prediction of broadband noise from wind turbines. Journal of sound and vibration, 118(2):217–239, 1987.

[34] Francesco Grasso. Usage of numerical optimization in wind turbine airfoil design. Journal of Aircraft, 48(1):248–255, 2011.

[35] Ferdinand W Grosveld. Prediction of broadband noise from horizontal axis wind turbines. Journal of propulsion and power, 1(4):292–299, 1985.

[36] Gianfranco Guidati, Rainer Bareiss, Siegfried Wagner, Ton Dassen, and Rene Parchen. Simulation and measurement of inflow-turbulence noise on airfoils. American Institute of Aeronautics and Astronautics Paper, pages 97–1698, 1997.

[37] RE Hayden, HL Fox, and RC Chanaud. Some factors influencing radiation of sound from flow interaction with edges of finite surfaces. NASA CR-145073, 1976.

[38] Chad W Higgins, Martin Froidevaux, Valentin Simeonov, Nikki Vercauteren, Caitlin Barry, and Marc B Parlange. The effect of scale on the applicability of taylors frozen turbulence hypothesis in the atmospheric boundary layer. Boundary-layer meteorology, 143(2):379–391, 2012.

[39] JO Hinze. Turbulence. McGraw-Hill Book Company, Inc, New York, 1975.

[40] MS Howe. A review of the theory of trailing edge noise. Journal of Sound and Vibration, 61(3):437–465, 1978.

[41] Florence V Hutcheson, Thomas F Brooks, and Daniel J Stead. Measurement of the noise resulting from the interaction of turbulence with a lifting surface. International Journal of Aeroacoustics, 11(5-6):675–700, 2012.

[42] Applied Technologies Inc. Operational features and commands for the sati series ultrasonic anemometer. http://http://www.apptech.com/products/ultrasonic-anemometers/operational-features-and-commands/. Accessed: 2017-04-02.

[43] National Instruments. Pseudodifferential versus differential input configurations, 2012.

[44] JC Kaimal, JCj Wyngaard, Y Izumi, and OR Coté. Spectral characteristics of surface-layer turbulence. Quarterly Journal of the Royal Meteorological Society, 98(417):563–589, 1972.

[45] M Kamruzzaman, Th Lutz, W Würz, Wen Zhong Shen, Wei Jun Zhu, Martin Otto Laver Hansen, Franck Bertagnolio, and H Aa Madsen. Validations and improvements of airfoil trailing-edge noise prediction models using detailed experimental data. Wind Energy, 15(1):45–61, 2012.

[46] Seunghoon Lee, Kyutae Kim, Wooyoung Choi, and Soogab Lee. Annoyance caused by amplitude modulation of wind turbine noise. Noise Control Engineering Journal, 59(1):38–46, 2011.

[47] Michael J Lighthill. On sound generated aerodynamically. i. general theory. Proceedings of the Royal Society of London. Series A. Mathematical and Physical Sciences, 211(1107):564–587, 1952.

[48] Michael J Lighthill. On sound generated aerodynamically. ii. turbulence as a source of sound. In Proceedings of the Royal Society of London A: Mathematical, Physical and Engineering Sciences, volume 222, pages 1–32. The Royal Society, 1954.

[49] Martin V Lowson. Assessment and prediction of wind turbine noise. Technical report, Flow Solutions Ltd., Bristol, United Kingdom, 1993.

[50] Helge A Madsen, Franck Bertagnolio, Andreas Fischer, and Christian Bak. Correlation of amplitude modulation to inflow characteristics. In INTER-NOISE and NOISE-CON Congress and Conference Proceedings, volume 249, pages 12136–12136. Institute of Noise Control Engineering, 2014.

[51] Jakob Mann. The spatial structure of neutral atmospheric surface-layer turbulence. Journal of fluid mechanics, 273:141–168, 1994.

[52] Y Maruta and S Kotake. Separated flow noise of a flat plate at large attack angles. Journal of Sound and Vibration, 89(3):335–357, 1983.

[53] Stephane Moreau and Michel Roger. Competing broadband noise mechanisms in low-speed axial fans. AIAA journal, 45(1):48–57, 2007.

[54] Stéphane Moreau, Michel Roger, and Julien Christophe. Flow features and self-noise of airfoils near stall or in stall. AIAA paper, 3198:2009, 2009.

[55] Stephane Moreau, Michel Roger, and Vincent Jurdic. Effect of angle of attack and airfoil shape on turbulence-interaction noise. In 11 th AIAA/CEAS Aeroacoustics Conference(26 th Aeroacoustics Conference), pages 1–20, 2005.

[56] Patrick J Moriarty. Development and validation of a semi-empirical wind turbine aeroacoustic code. NREL Report, 2004.

[57] Patrick J Moriarty, Gianfranco Guidati, and Paul Migliore. Recent improvement of a semi-empirical aeroacoustic prediction code for wind turbines. In Proc., 10th AIAA/CEAS Aeroacoustics Conference, Manchester, UK, AIAA, volume 3041, page 2004, 2004.

[58] Patrick J Moriarty, Gianfranco Guidati, and Paul Migliore. Prediction of turbulent inflow and trailing-edge noise for wind turbines. In Proc. of the 11th AIAA/CEAS Aeroacoustics Conf.(Monterey, CA), AIAA Paper, volume 2881, page 2005, 2005.

[59] Patrick J Moriarty and Paul G Migliore. Semi-empirical aeroacoustic noise prediction code for wind turbines. National Renewable Energy Laboratory Golden, CO, USA, 2003.

[60] Stefan Oerlemans. Detection of aeroacoustic sound sources on aircraft and wind turbines. University of Twente Doctoral Thesis, 2009.

[61] Stefan Oerlemans. An explanation for enhanced amplitude modulation of wind turbine noise. Wind Turbine Amplitude Modulation: Research to Improve Understanding as to its Cause and Effect. RenewableUK, 2013.

[62] Stefan Oerlemans. Effect of wind shear on amplitude modulation of wind turbine noise. International Journal of Aeroacoustics, 14(5-6):715–728, 2015.

[63] Stefan Oerlemans, Murray Fisher, Thierry Maeder, and Klaus Kögler. Reduction of wind turbine noise using optimized airfoils and trailing-edge serrations. AIAA Journal, 47(6):1470–1481, 2009.

[64] Stefan Oerlemans and JG Schepers. Prediction of wind turbine noise and validation against experiment. International Journal of Aeroacoustics, 8(6):555–584, 2009.

[65] Stefan Oerlemans, Peter Sijtsma, and B Méndez López. Location and quantification of noise sources on a wind turbine. Journal of Sound and Vibration, 299(4):869–883, 2007.

[66] Steven P Oncley, Carl A Friehe, John C Larue, Joost A Businger, Eric C Itsweire, and Sam S Chang. Surface-layer fluxes, profiles, and turbulence measurements over uniform terrain under near-neutral conditions. Journal of the Atmospheric Sciences, 53(7):1029–1044, 1996.

[67] René R Parchen. Progress report DRAW: A prediction scheme for trailing edge noise based on detailed boundary layer characteristics. TNO Institute of Applied Physics, 1998.

[68] Robert W Paterson and Roy K Amiet. Noise of a model helicopter rotor due to ingestion of turbulence. 1979.

[69] Robert W Paterson, Roy K Amiet, and C Lee Munch. Isolated airfoil-tip vortex interaction noise. Journal of Aircraft, 12(1):34–40, 1975.

[70] Robert William Paterson. Acoustic radiation and surface pressure characteristics of an airfoil due to incident turbulence. NASA CR-2733, 1976.

[71] Eja Pedersen, Frits van den Berg, Roel Bakker, and Jelte Bouma. Response to noise from modern wind farms in the netherlands. The Journal of the Acoustical Society of America, 126(2):634–643, 2009.

[72] Eja Pedersen and Kerstin Persson Waye. Perception and annoyance due to wind turbine noisea dose–response relationship. The Journal of the Acoustical Society of America, 116(6):3460–3470, 2004.

[73] Michel Roger and Stéphane Moreau. Extensions and limitations of analytical airfoil broadband noise models. International Journal of Aeroacoustics, 9(3):273–306, 2010.

[74] Robert H Schlinker and Roy K Amiet, editors. Helicopter rotor trailing edge noise, October 1981.

[75] I J Sharland. Sources of noise in axial flow fans. Journal of Sound and Vibration, 1(3):302–322, 1964.

[76] Samuel Sinayoko and Jeremy Hurault. On predicting wind turbine noise and amplitude modulation using amiet's theory. In Proceedings of the 6th International Conference on Wind Turbine Noise, April 2015.

[77] GP Van den Berg. Effects of the wind profile at night on wind turbine sound. Journal of Sound and Vibration, 277(4):955–970, 2004.

[78] Siegfried Wagner, Rainer Bareiss, and Gianfranco Guidati. Wind turbine noise. Springer, 1996.

[79] JE Ffowcs Williams and LH Hall. Aerodynamic sound generation by turbulent flow in the vicinity of a scattering half plane. Journal of Fluid Mechanics, 40(04):657–670, 1970.

[80] JE Ffowcs Williams and David L Hawkings. Sound generation by turbulence and surfaces in arbitrary motion. Philosophical Transactions of the Royal Society of London. Series A, Mathematical and Physical Sciences, 264(1151):321–342, 1969.

[81] PK Yeung and Ye Zhou. Universality of the kolmogorov constant in numerical simulations of turbulence. Physical Review E, 56(2):1746, 1997.